2015

Automated segmentation and analysis of layers and structures of human posterior eye

Li Zhang
University of Iowa

AUTOMATED SEGMENTATION AND ANALYSIS OF LAYERS AND STRUCTURES OF HUMAN POSTERIOR EYE

by

Li Zhang

A thesis submitted in partial fulfillment of the
requirements for the Doctor of Philosophy
degree in Electrical and Computer Engineering
in the Graduate College of
The University of Iowa

December 2015

Thesis Supervisors: Professor Milan Sonka
Professor Michael D. Abràmoff

Graduate College
The University of Iowa
Iowa City, Iowa

CERTIFICATE OF APPROVAL

PH.D. THESIS

This is to certify that the Ph.D. thesis of

Li Zhang

has been approved by the Examining Committee for the thesis requirement for the Doctor of Philosophy degree in Electrical and Computer Engineering at the December 2015 graduation.

Thesis Committee: _____
Milan Sonka, Thesis Supervisor

_____
Michael D. Abràmoff, Thesis Supervisor

_____
Joseph M. Reinhardt

_____
Mona K. Garvin

_____
Andreas Wahle

ACKNOWLEDGEMENTS

I wish to express my sincere thanks to Dr. Milan Sonka and Dr. Michael D. Abràmoff, my advisors, for all the patient guidance and support they have given me. Throughout my PhD life, I have learned many great things from them, not only the knowledge but also critical thinking, research attitude and passions for the research. These have transformed me from an absolute newbie to a somehow qualified researcher.

A special thanks also goes to Dr. Abràmoff and Dr. Gabriëlle H.S. Buitendijk (from Rotterdam Eye Study Group) for their willingness to manually segment layers and structures in OCT images. I have also received considerable assistance from other ophthalmologists including Drs. Robert F. Mullins, Young H. Kwon, Elliott H. Sohn, James C. Folk, Stephen R. Russell.

Many thanks are due to my friends, lab-mates and colleagues Dr. Kit Lee, Dr. Hrvoje Bogunović, Dr. İpek Oğuz, Dr. Ling Zhang, Zhi Chen, Ray Wang, Junjie Bai, Dakai Jin, Chen Cui for their help over these years. I also appreciate Dr. Xinjian Chen and Dr. Meindert Niemeijer for sharing their great experience of research and paper-writing skills.

In addition, I would like to thank Dr. Joseph M. Reinhardt, Dr. Mona K. Garvin and Dr. Andreas Wahle for serving on my committee.

This work was supported, in part, by the NIH grants EY018853, EY017066, EB004640 and by Arnold and Mabel Beckman Initiative for Macular Research fund-

ing.

Finally, most of all thanks are for my loving wife. Thanks for being bright and fun, for showing unconditional support to and faith in me, and for throwing all the paint with me on the great big canvas of life.

ABSTRACT

Optical coherence tomography (OCT) is becoming an increasingly important modality for the diagnosis and management of a variety of eye diseases, such as age-related macular degeneration (AMD), glaucoma, and diabetic macular edema (DME). Spectral domain OCT (SD-OCT), an advanced type of OCT, produces three dimensional high-resolution cross-sectional images and demonstrates delicate structure of the functional portion of posterior eye, including retina, choroid, and optic nerve head. As the clinical importance of OCT for retinal disease management and the need for quantitative and objective disease biomarkers grows, fully automated three-dimensional analysis of the retina has become desireable. Previously, our group has developed the Iowa Reference Algorithms, a set of fully automated 3D segmentation algorithms for the analysis of retinal layer structures in subjects without retinal disease. This is the first method of segmenting and quantifying individual layers of the retina in three dimensions. However, in retinal disease, the normal architecture of the retina - specifically the outer retina - is disrupted. Fluid and deposits can accumulate, and normal tissue can be replaced by scar tissue. These abnormalities increase the irregularity of the retinal structure and make quantitative analysis in the image data extra challenging.

In this work, we focus on the segmentation of the retina of patients with age-related macular degeneration,the most important cause of blindness and visual loss in the developed world. Though early and intermediate AMD results in some vision loss,

the most devastating vision loss occurs in the two endstages of the disease, called geographic atropy (GA) respectively choroidal neovascularization (CNV). In GA, because of pathological changes that are not fully understood, the retinal pigment epithelium disappears and photoreceptors lose this supporting tissue and degenerate. Second, in CNV, the growth of abnormal blood vessels originating from the choroidal vasculature causes fluid to enter the surrounding retina, causing disruption of the tissues and eventual visual loss. The severity and progress of early AMD is characterized by the formation of drusen and subretinal drusenoid deposits, structures containing photoreceptor metabolites - primarily lipofuscin - the more drusen the more severe the disease and the higher the risk of progressing to GA or CNV. Thus, to improve the image guided management of AMD, we will study automated methods for segmenting and quantifying these intraretinal, subretinal and choroidal structures, including different types of abnormalities and layers, focusing on the outer retina.

The major contributions of this thesis include: 1) developing an automated method of segmenting the choroid and quantifying the choroidal thickness in 3D OCT images; 2) developing an automated method of quantifying the presence of drusen in early and intermediate AMD; 3) developing an method of identifying the different ocular structures simultaneously; 4) studying the relationship among intraretinal, subretinal and choroidal structures.

PUBLIC ABSTRACT

The posterior segments of human eyeball, especially the retina and the choroid, are playing important roles in visual processing. The retina is the light-sensitive layer of tissue, which acts like a film in the camera to receive images and convert them to electric signals. The choroid is the layer of blood vessels and connective tissue that supply oxygen and nutrients to the inner parts of the eye including the retina.

Many eye diseases affect these two layers. In this work, we focus on age-related macular degeneration (AMD), a disease that causes a majority of vision loss and blindness among adults over 50 years old. Typically, AMD patients suffer from damages of their central vision and are incapable of seeing objects in the front of them.

AMD-affected eyes are characterized with abnormal cysts and deposits in the retinal and the choroidal regions. Quantifying these abnormalities is crucial in the diagnosis of AMD. Traditionally, doctors used two-dimensional images of the posterior segment of AMD patients eyes to roughly evaluate the conditions of patients eye(s). This type of diagnosis is inefficient and often less accurate, given that it requires a doctor to manually analyze a substantial number of images for hours.

In this work, we use a novel three-dimensional modality of eye imaging – optical coherence tomography (OCT) imaging – to access the delicate structures of human eyes. Furthermore, we develop several advanced and automated image processing algorithms and methods to measure important indices of AMD disease such as the

size of cysts and deposits, the area of the affected regions, the volume of the related vessels, and the thickness of the related layers. Using our automated analyses, doctors could obtain the quantitative references with high accuracy by just "one-click". Thus, our methods have the potential to improve the diagnosis and the management of the AMD among other eye diseases.

TABLE OF CONTENTS

LIST OF FIGURES

Figure

CHAPTER 1
INTRODUCTION

Optical coherence tomography (OCT) is becoming an increasingly important modality for the diagnosis and management of a variety of eye diseases, such as age-related macular degeneration (AMD) [1], glaucoma [2], and diabetic macular edema (DME) [3]. Optical coherence tomography utilizes the low coherence interferometry to image the eye structures. Spectral domain OCT (SD-OCT), an advanced type of OCT, produces three dimensional high-resolution cross-sectional images and demonstrates delicate structure of the functional portion of posterior eye [4, 5], including retina, choroid, and optic nerve head [6]. As the clinical importance of OCT for retinal disease management and the need for quantitative and objective disease biomarkers grows, fully automated three-dimensional analysis of the retina is desireable. Previously, our group has developed the Iowa Reference Algorithms (https://www.iibi.uiowa.edu/content/iowa-reference-algorithms-human-and-murine-oct-retinal-layer-analysis-and-display), a set of fully automated 3D segmentation algorithms for the analysis of retinal layer structures in subjects without retinal disease. This is the first method of segmenting and quantifying individual layers of the retina in three dimensions [7]. However, in retinal disease, the normal architecture of the retina - specifically the outer retina - is disrupted. Fluid and deposits can accumulate, and normal tissue can be replaced by scar tissue. These abnormalities increase the irregularity of the retinal structure and make quantitative analysis in the image data extra challenging.

In this work, we focus on the segmentation of the retina of patients with age-related macular degeneration, the most important cause of blindness and visual loss in the developed world [8, 9]. Though early and intermediate AMD results in some vision loss, the most devastating vision loss occurs in the two endstages of the disease, called geographic atropy(GA) respectively choroidal neovascularization (CNV) [10]. In GA, because of pathological changes that are not fully understood, the retinal pigment epithelium disappears and photoreceptors lose its supporting tissue and degenerate eventually [11, 12]. In CNV, the growth of abnormal blood vessels originating from the choroidal vasculature causes fluid to enter the surrounding retina, causing disruption of the tissues and visual loss [13]. The severity and progression of AMD is characterized by the formation of drusen and subretinal drusenoid deposits, structures containing photoreceptor metabolites - primarily lipofuscin - the more drusen the more severe the disease and the higher the risk of progressing to atrophic AMD or CNV [11]. To improve the image guided management of AMD, we will study automated methods for segmenting and quantifying these intraretinal, subretinal and choroidal structures, including different types of abnormalities and layers, focusing on the outer retina.

We define the outer retinal-subretinal layer as those tissue layers between external limiting membrane (ELM) and Bruchs membrane (BM), consisting of the inner segments of the photoreceptors, the virtual space between inner and outer segments, the outer segments of the photoreceptors, the (virtual) subretinal space, the pigment epithelium, the virtual sub-RPE space, and Bruch's membrane. Though the afore-

mentioned virtual spaces do not materialize in normals, in retinal disease they may realize and be filled with fluid or deposits, and therefore segmentable on OCT images [11]. There are two types of photoreceptor cells, rods and cones, the primary origin of vision as they transform their activation by a photon into an electrical impulse. [14]. The RPE is composed of a single but dense layer of hexagonal cells, maintaining balance of water, pH and biochemical compounds [15]. Abnormalities occur in retinal diseases. Drusen [16] presents in the virtual sub-RPE space between RPE and BM in dry form of AMD. Subretinal drusenoid deposits (SDD) realize virtual sub-retinal space between outer segment of photoreceptor layer and RPE [17]. In CNV, pigment epithelial detachments [18] build up in the virtual sub-RPE space, subretinal fluid [19] presents in the virtual subretinal space, and intraretinal fluid within the retina. Drusen, subretinal fluid and pigment epithelial detachment may result in distortion and damage in the sub-retina [20].

Clinically, the size and location of these abnormalities are evaluated visually by the clinician, though semi-automated methods have been developed for research studies [21, 22, 23]. Such methods are not fully automated as required by the clinic workflow and suffer from large intra- and inter-observer variability and inefficiency from human interaction. In our study, we have developed several three dimensional fully-automated segmentation methods for segmenting and quantifying subretinal structures, including RPE, drusen, subretinal fluid and pigment epithelial detachment. Such segmentation and analysis methods are crucial for improved evaluating and managing of AMD becasue of the nature and risk of AMD treatments, if

available.

The choroid is a vascular plexus between retina and sclera, forms a vascular system with the highest flow of any tissue in the human body, and is crucial for oxygenation and metabolic activity of the RPE and outer retina [24]. Choroidal thickness changes in many retinal disease, including thickening in central serous retinopathy [25], and in choroiditis [26]. In other retinal diseases, the choroid thickness decreases in choroidal atrophy [27], in AMD, even in normal aging [28, 29, 30]. Specifically, choroidal thinning has been implicated in AMD and may be a potential initiating factor. Therefore to quantitatively and in 3D measure choroidal thickness is of great importance.

Due to the relatively low contrast of the choroid in the standard clinically available SD-OCT, choroidal imaging and segmentation is challenging. Previously, our group has reported a 3D automated segmentation of the choroid from clinical SD-OCT [28]. This is the first method for segmenting the choroidal vasculature and estimating the global average thickness of choroidal vasculature and choriocapillaris using surface fitting. Currently, compared to the estimation results of surface fitting, more accurate segmentation method of the choroid layer will be our next goal. Such methods would be even more useful for understanding the association between the changes of choroidal thickness and the eye diseases with regional abnormalities.

The events that the different virtual spaces sketched above undergo are of great interest. For example, drusen and choroidal thinning occur in age-related macular degeneration. However, quantification of such features has so far been difficult. Starting

with our automated segmentation methods as discussed above, we will start quantitative studies of relationship between drusen and choroidal thinning. In addition, decreased choroidal thickness has been described in age-related macular degeneration, both nonexudative and exudative AMD, although it has not been universally observed. Thus, after developing the individual segmentation of structures of subretina and choroid, we plan on combining the results of these methods to help show additional clinical information from segmenting and analyzing different tissues of subretina and choroid simultaneously. This comprehensive analysis has the potential to increase our understanding of the 'vertical' interaction in the outer retina between photoreceptors, RPE and choroid.

1.1 Specific Aims

- **Aim 1:** Develop and validate methods for segmenting choroid, including choroidal vasculature and the boundaries of choroid layers.
- **Aim 2:** Develop and validate methods for segmenting subretinal tissues, including RPE, photoreceptors in the face of disruptions of the outer retinal architecure caused by retinal diseases. Develop and validate methods for segmenting the realized virtual spaces sketched above including drusen.
- **Aim 3:** Integrate and analyze segmentation results to obtain more clinically useful information.

1.2 Thesis Overview

This thesis contains 6 chapters. The following is an overview of the remaining chapters:

- Chapter 2 provides background information and literatures review of the entire thesis, including the introduction of age-related macular degeneration, choroid, structures in outer-retinal sub-retinal layer and graph theory.
- Chapter 3 provides a summary of the methods for segmenting choroidal vasculature and choroidal boundaries in 3D OCT volumetric images.
- Chapter 4 provides the methods for segmenting outer-retinal sub-retinal layer and abnormal regions as drusen in neovascular or non-neovascular age-related macular degeneration disease.
- Chapter 5 provides the theoretical algorithms for the proposed segmentation methods in Chapters 3 and 4.
- Chapter 6 provides a few preliminary results for showing the segmentations combined from multiple methods and possible extensions of the proposed developments to new imaging modalities, and also revealed the significance of interpreting clinical biomarkers from the segmentation results.
- Chapter 7 provides the conclusions of this thesis.

CHAPTER 2
BACKGROUND AND LITERATURE REVIEW

2.1 Age-related Macular Degeneration

Age-related macular degeneration is the primary cause of vision loss among the adults (>50 years). Central vision is damaged so that patients may not be able to recognize the objects in the front (Figure 2.1).

Early AMD is the most common type of macular degeneration and affects 90% of the people with macular degeneration. In this early stage, presence of drusen (dots of yellow appearing crystalline deposits that develop within the macular region) is the pathognomic sign . AMD affects the photoreceptor cells, which gathers photons and convert them into action impulses for futher processing in the virtual cortex [14]. In geographic atrophy [31] the RPE degenerates, causing death of photoreceptors. Geographic atrophy reduces the central vision and can effect color perception, and eventually results in vision loss and blindness.

Approximately 10% of patients with age related macular degeneration have the exudative form of this disease. Exudative AMD (wet-AMD or choroidal neovascularization) typically includes overt evidence of choroidal neovascularization (CNV) [13], manifesting as retinal pigment epithelial detachment, subretinal and intraretinal cysts and fluid, retinal pigment epithelial tears, fibrovascular disciform scarring and vitreous hemorrhage. An important factor in CNV is excess vascular endothelial growth factor (VEGF). Recently, anti-vascular endothelial growth factor (anti-VEGF) agents

Figure 2.1: Vision of Age-related macular degeneration patient.

Image from http://galleryhip.com/wet-amd-vs-dry-amd.html

have become the mainstay of treatment for CNV [13]. Defects in Bruch's membrane occur. In addition to visual acuity as a functional measurement, retinal thickening, location, and amount of intra- and subretinal fluid as imaged by optical coherence tomography have become the principal milestones in the management of CNV with anti-VEGF agents. Therefore, accurately and automatically segmenting the retinal structures in CNV is important. However, CNV-associated retinal layer distortion

resulted from intra- and sub-retinal fluid accumulation makes accurate segmentation more challenging than in normal subjects or patients with, atrophic diseases such as glaucoma.

2.2 Choroid

The choroid is a vascular plexus between the retina and the sclera, it forms a vascular system with the highest flow of any tissue in the human body [24]. Anatomically, the choroid can be divided into two principal components: the choriocapillaris, a lobular, vascular plexus comprised of large fenestrated capillaries adjacent to Bruchs membrane, and the choroidal stroma, a combination of Sattler and Haller's layers. The thickness of choriocapillaris measures between 20 to 50μm. For choroidal vasculature, most of the choroidal vasculature thickness is attributable to the choroidal stroma, which is comprised of larger vessels that supply and drain the choriocapillaris, as well as melanocytes, fibroblasts, immune cells, neurons, and ground substance that contribute to its thickness. In this study, we will study the two layers of choroidal vasculature: Haller's layer, the outermost layer of larger diameter choroidal vessels; Sattler's layer, the layer of medium diameter choroidal vessels. The choroidal circulation is crucial for oxygenation and metabolic activity of the RPE and outer retina. The choroid receives the arterial blood from ophthalmic feeding arteries, and supplies oxygen and nutrients to RPE and approximately outer third of the retina. In the central macular region, crucial for vision, the choroid provides almost all the blood supply to the entire retina.

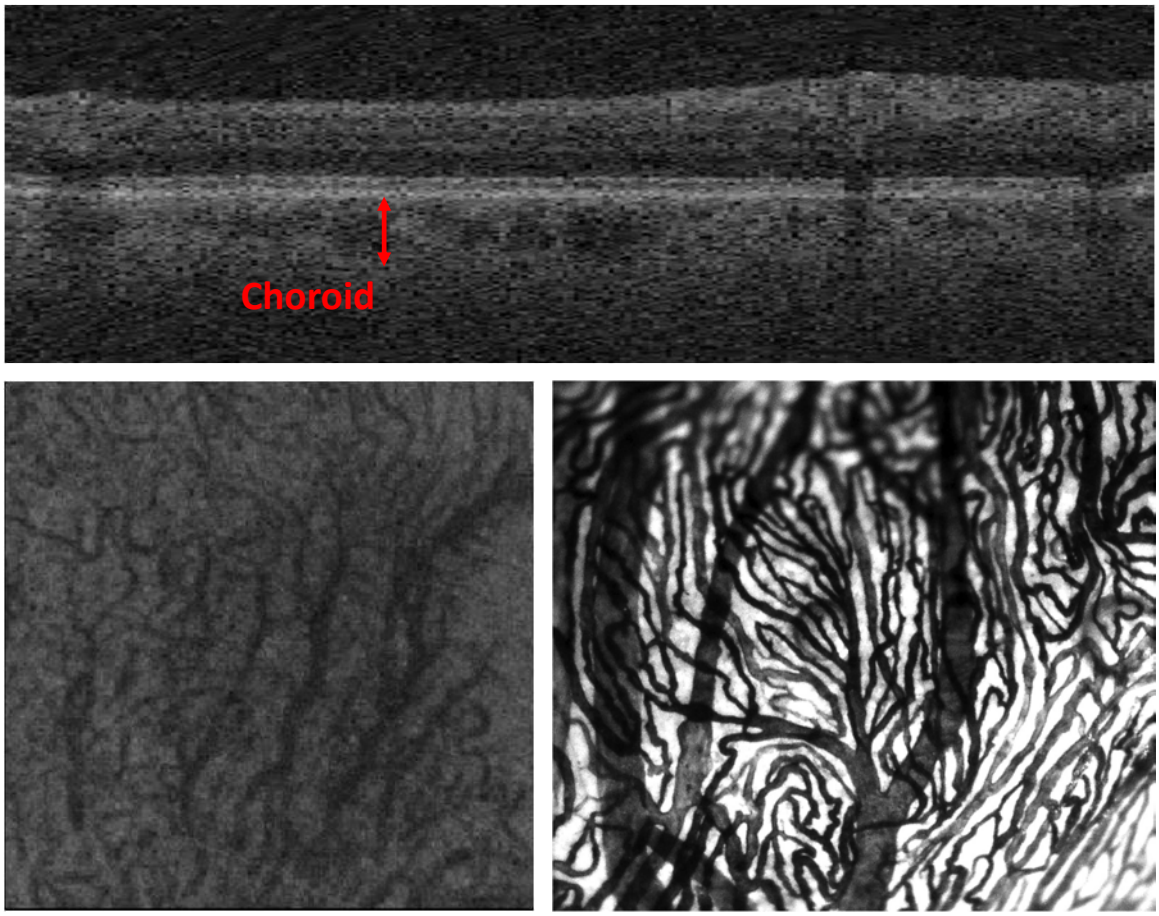

Figure 2.2: Top: an example B-scan shows the relative position between the choroid and the retina; Lower-left: en-face view of choroidal vasculature; Lower-right: an example of choroidal imaging by endogenous alkaline phosphatase activity.

As set forward above, quantitative analysis of the choroid in vivo is of great interest to ophthalmic research. Recently, many groups have developed objective methods to quantify the choroidal thickness and choroidal vessels from OCT:

- Chhablani *et al.* reported a manual measurement of choroidal thicknes and volume in Enhanced Depth Imaging-OCT (EDI-OCT) images. Repeatability and

reproducibility analysis were performed on the results. Manual identification of choroidal boundaries may be time-consuming and tedious [32].

- Shin *et al.* reported a 2D quantitative analysis of choroid on six high-resolution radial line scans. Thickness maps were provided, however, due to the large interval between adjacent line scans, the thickness may not be accurate [33].
- Hu *et al.* proposed a semi-automated method for segmenting the choroid in EDI-OCT images. Extra constraints and pre-processing steps may be needed for applying this method on the data from diseased eye. Due to the data-specified problem, the extension of this method was limited [34].
- Tian *et al.* has developed a 2D intensity transition-based segmentation method to quantify choroidal thickness using Spectralis EDI-OCT images. The method required high-quality OCT B-scans. However, due to the limited time of data acquisition, 3D volumetric information was not available when high-resolution in 2D B-mode was enforced. Thus, 3D choroidal thickness may not be achieved using this method [35].
- Duan *et al.* proposed an automated segmentation of choroidal boundaries using phase-retardation information from polarization sensitive OCT. Although this device is not clinically in use, and requires a special device, this may be a new useful feature for detecting choroid/sclera junction [36].
- we have previously developed a fully automated segmentation method to segment and visualize choroidal vasculature and to quantify choroidal thickness using Hessian vesselness analysis and Thin-plate spline surface fitting approach.

Although this method segmented choroidal vasculature, the actual choroidal boundaries were only approximately estimated as the fitted surfaces [28].

2.3 Outer Retinal-subretinal Layer

We define the outer retinal-subretinal layer (ORSR) as extending from the external limiting membrane (ELM) to Bruch's membrane (BM), including the photoreceptor layers (inner segment and outer segment) and retinal pigment epithelium layer, as well as the virtual spaces between these tissues. Early on, age-related macular degeneration causes deposits in the outer retinal-subretinal layer between the outer segments and RPE called subretinal drusenoid deposits and RPE and BM, called drusen, while geographic atrophy causes degeneration of the RPE, and choroidal neovascularization causes fluid between RPE and BM, between RPE and outer segments and elsewhere in the retina. In this study, we will develop segmentation method for identifying and evaluating the following abnormalities.

2.3.1 CNV: Pigment Epithelial Detachment and Subretinal Fluid

In CNV, fluid-filled abnormalities may occur in any part of retina. Typically, these abnormalities are categorized into three types: intra-retinal fluid, subretinal fluid and pigment epithelial detachment. Two types of fluid – pigment epithelial detachment and subretinal fluid will be studied and analyzed in this work.

- Pigment epithelial detachment (PED): choroidal disordering disrupts the normal junction between RPE and Bruchs membrane.
- Subretinal fluid (SRF): In sub-retinal fluid, small disruptions may compromise

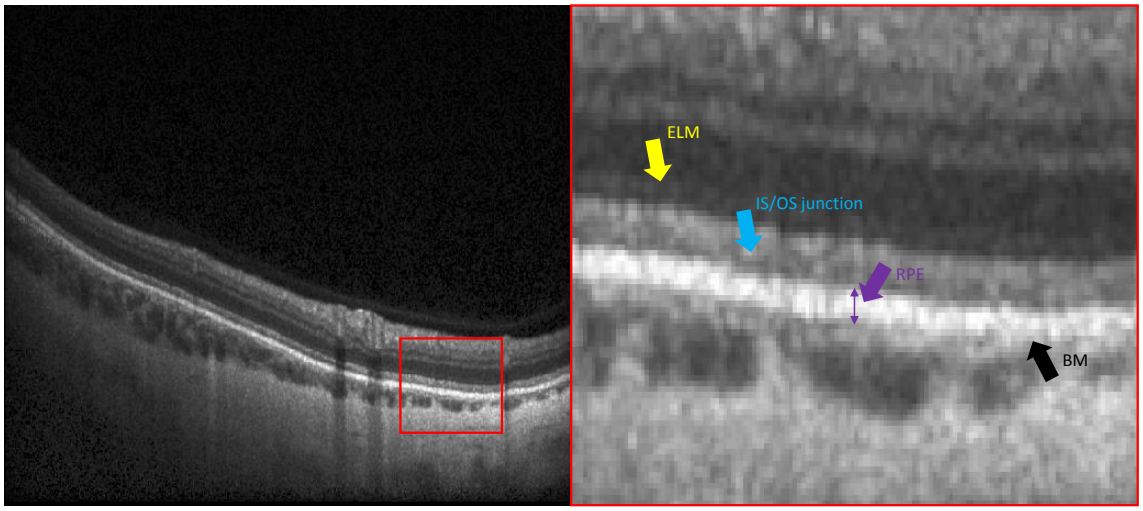

Figure 2.3: The surfaces related to the proposed studies: external limiting membrane (ELM), inner segment and outer segment junction (IS/OS junction), retinal pigment epithelium layer (RPE), and Bruch's membrane (BM).

the barriers of retinal pigment epithelium, resulting in detachment of the outer segment layer from the RPE

Many studies regarding imaging analysis of CNV have been published recently:

- Fernandez reported a semi-automated delineation method relying on manual initialization on 2D B-scans. This is the first quantitative measurement on OCT images. However, it suffers from large intra- and inter-observer variabilities and is not time-efficient [37].
- Ding *et al.* reported an automatic B-scan-based detection of SRF and PED on OCT images in 2D. This method only showed an estimation of the two types of fluid, but the accuracy was not high and real segmentation has not been

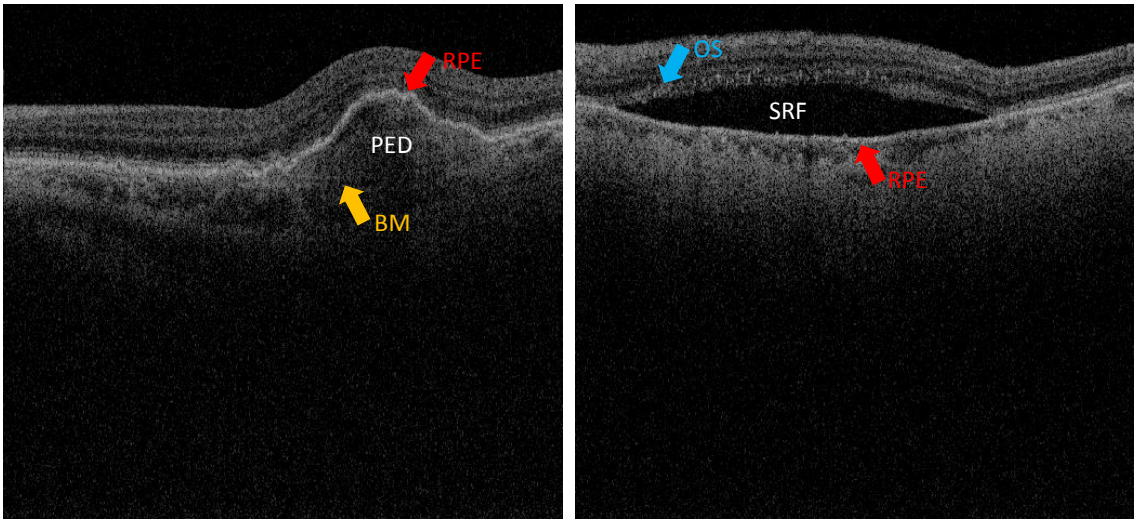

(a) (b)

Figure 2.4: Choroidal neovascularization (CNV) related fluid-filled abnormalities: left figure, pigment epithelial detachment (PED) between the outer boundary of RPE and BM; right figure, subretinal fluid (SRF) is between the outer boundary of the outer segments (OS) and RPE.

achieved [38].

- Quellec *et al.* reported a voxel classification method for detecting the "footprint" of SRF and PED in en-face projections. The results showed effected regions of fluid-filled abnormalities but a true volume measurement cannot be performed with only "footprint" maps [39].
- An automatic segmentation tool was reported by Ahlers *et al.* but it failed to segment up to 30% of the analyzed scans [40].

- Dolejší *et al.* developed a two-step 3D SEAD segmentation with human interaction. Thus, the method may suffer from time-consuming issues [41].
- Chen *et al.* proposed a 3D fully automated segmentation of fluid-filled abnormalities on Spectral domain OCT images (the Iowa Reference Algorithm). However, the method suffered from fluid-in constraints between neighboring surfaces and fluid-filled region, resulting high accuracy with flat SRF/PED, but low accuracy with tall and big SRF/PED [42].

2.3.2 Drusen

Quantitative analysis of drusen, classicially only 2D measurements on fundus photographs were available. Three-dimensional segmentation methods were reported recently.

- Kirkpatrick *et al.* reported a texture based method to quantify drusen in 2D fundus photographs. But they only achieved a sensitivity of 60%, when the specificity was enforced as 90% [43].
- Ben Sbeh *et al.* proposed a 2D approach using geodesic reconstruction on fundus photographs. The authors did not show the evaluation results of the method. False positive and false negative response occurred in the results that they showed in the figures [44].
- Niemeijer *et al.* has developed a supervised pixel classification method to detect and differentiate drusen from similar lesions on fundus photographs. However, manual annotation of the lesions were needed. [21].

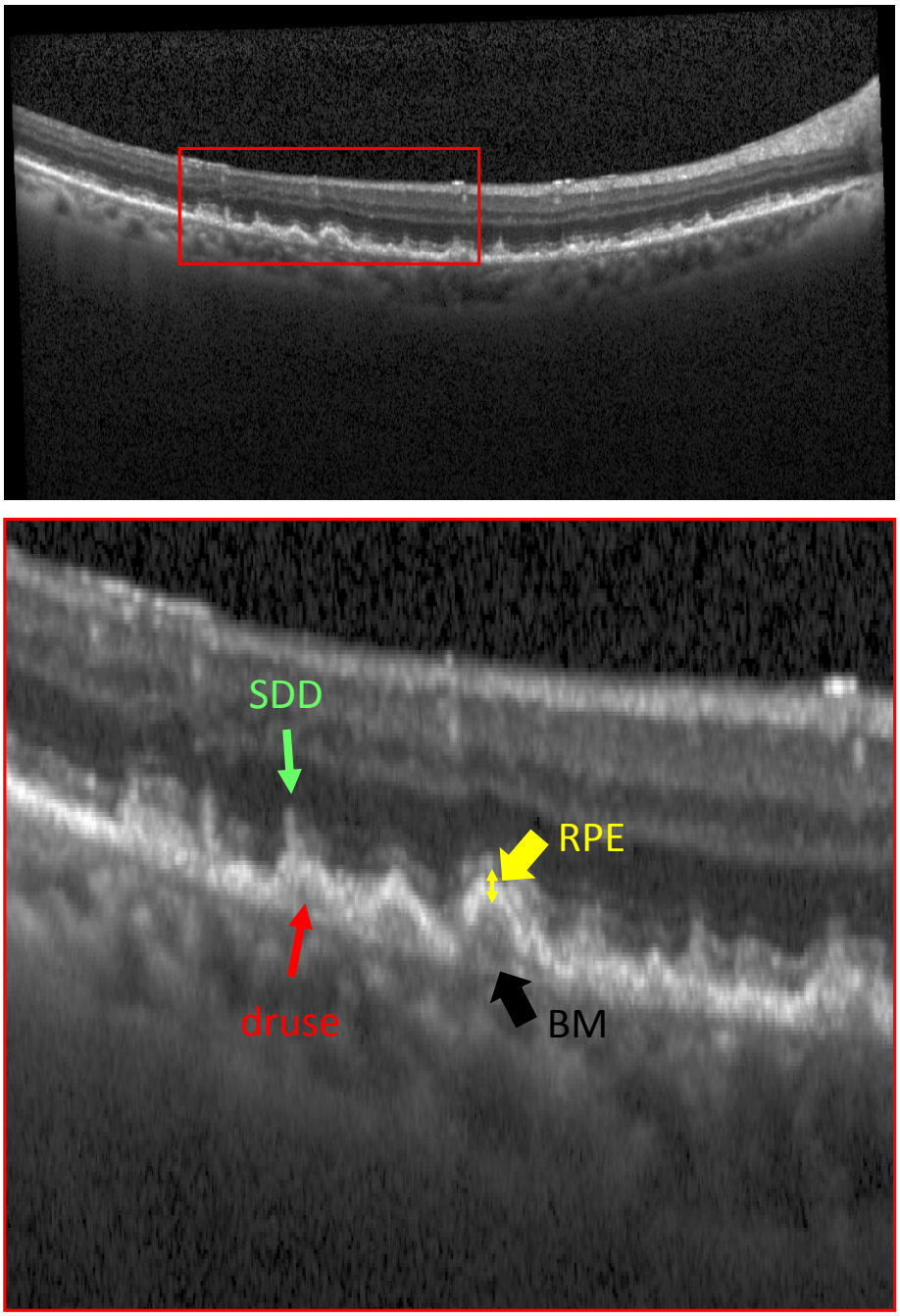

Figure 2.5: Abnormal regions in early AMD: 1. subretinal drusenoid deposits (SDD's), "spiky" shaped debris above RPE; 2. drusen, abnormal accumulations in sub-RPE space.

- Quellec *et al.* has reported a model based method to detect, quantify and statistically analyze the drusen phenotypes in early AMD on 2D fundus photographs. Three-dimensional volume analyses were not available using this method [45, 46].
- Chiu *et al.* has developed an automatic segmentation method capable of segmenting macular drusen and geographic atrophy in SD-OCT images. The method was limited of using 2D B-scans, thus, clinically important information, such as drusen load, may be available using this method [47].
- Dufour *et al.* has reported a 3D multi-surface segmentation using trained hard and soft constraints capable of segmenting the upper and lower boundaries of drusen. However, the training-based approach is dataset-specified and very sensitive to image quality [48].

2.3.3 Subretinal Drusenoid Deposits

Several groups have attempted to perform statistical analyses on the prevalence and significance of SDD: in the study reported by Zweifel *et al.* [49], SDD's were manually graded based on intensity of different channels from color fundus photographs and confirmed by SD-OCT images. Curcio *et al.* analyzed multiple properties of SDD's such as morphology, prevalence, topography on histological images of donor eyes using computer aided software [50]

Although quantitative detection and analysis of subretinal drusenoid deposits are challenging, we hope new imaging analysis techniques may help reveal more clin-

ically important facts of SDD in vivo retinal images such as spectral domain OCT volumetric scans.

2.4 OCT Modality

Optical coherence tomography (OCT) is an increasingly important modality for the noninvasive management of ocular diseases, such as age-related macular degeneration, diabetic macular edema, and glaucoma [51]. An OCT image represents a cross-sectional, micrometer-resolution, three-dimensional depiction of biological tissue of human posterior eye. Spectral domain OCT (SD-OCT) is an advanced type of OCT imaging using Fourier domain detection techniques, which provides a significantly high scanning speed for measuring single column (also called A-scan) simultaneously. Depending on the number of frames (also called B-scans), SD-OCT image volume data are divided into two groups: "isotropic image" and "non-isotropic image". Three dimensional image analysis methods may have significant difference in processing these these types of image volume data. Swept-source OCT (SS-OCT) has the potential for increasing the scanning speed in retinal imaging [52]. Compared to conventional SD-OCT imaging, a longer central wave-length used in SS-OCT (1060nm versus 840nm in SD-OCT) provides higher penetration through RPE enabling deep choroidal imaging. The choroid/sclera junction that is difficult to be identified in conventional scanners is now visible in SS-OCT.

- "Isotropic" image: At the cube setting Zeiss Cirrus images a typical isotropic SD-OCT image volume with respect to the base geometry of the sampling. The

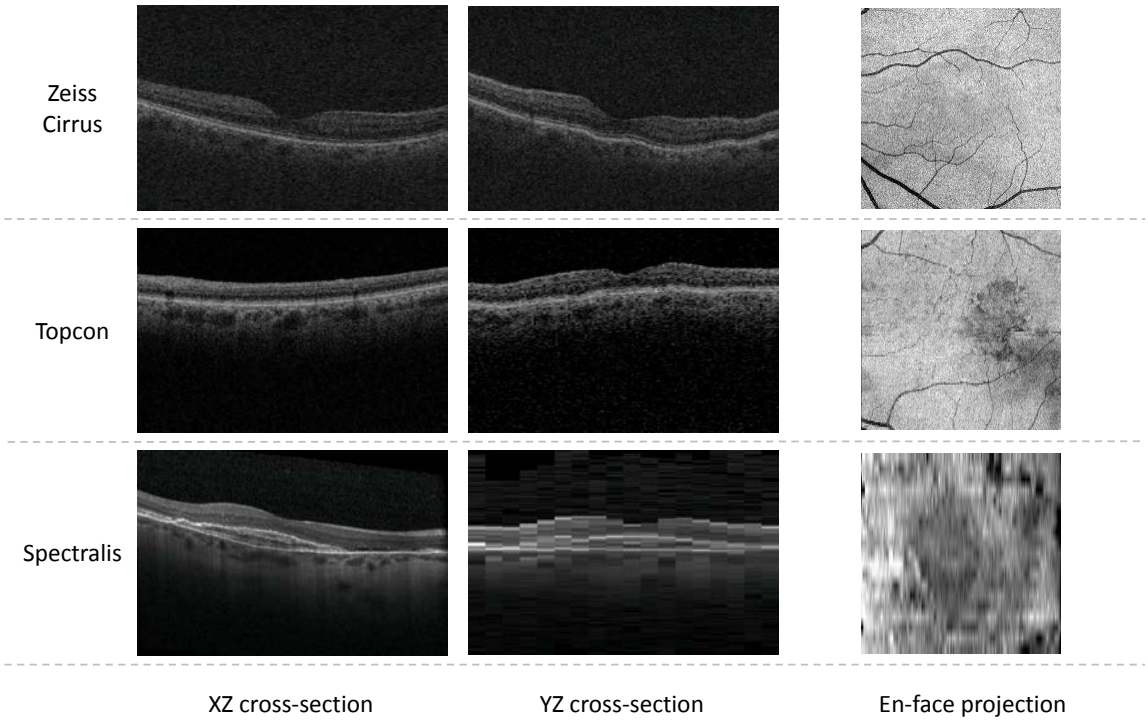

Figure 2.6: Comparison of the dimensions from three OCT scanners related to the proposed study (Zeiss Cirrus, Topcon and Heidelberg Spectralis).

physical dimension is this setting is $6\times6\times2mm^3$ with $200\times200\times1024$ voxels, and voxel size of $30\times30\times2\mu m^3$. This type of SD-OCT image provides consecutive B-scan information, which is important for the analysis methods using three-dimensional textural or structural image features, such as vessel segmentation approaches and 3D object detection methods.

- "Non-isotropic" image: This type of SD-OCT contains only a few B-scans that are spaced an order of magnitude or more apart than the distance between the A-scans (typically 20-40 μm), for example, Heidelberg Spectralis produces SD-

OCT with 19 or 31 B-scans in a $6\times6mm^2$ region. The distance interval between neighboring B-scans (in the y-axis) is relatively large, so it is difficult to obtain 3D contextual information from y direction. Despite of this, the "non-isotropic" type of SD-OCT usually has high resolution in each of the B-scans, which is suitable for analyzing detailed retinal/choroidal structure in 2D.

2.5 Conventional Graph-based Methods

Conventional graph-cut algorithm: Boykov *et al.* reported a fast image segmentation approach – Graph Cut methods [53, 54], which is commonly used in medical image analysis in recent years. By introducing regional terms and boundary terms into the graph-cut energy function, the method computes a minimum cost s/t cut on an appropriately constructed graph. The conventional graph-cut framework can be applied to objects with different topological shapes, but it cannot avoid segmentation leaks in lower-resolution images.

Optimal surface approach graph-search approach: The optimal surface approach was first demonstrated by Li *et al.* in [55]. This approach modeled the boundaries in-between layers as terrain-like surfaces and suggested representing the terrain-like surface as a related closed set. By finding an optimal closed set, the approach was able to segment the terrain-like surface. For the multiple-surface case, the approach constructed a corresponding sub-graph for each surface. Weighted inter-graph arcs were added, which enforced geometry constraints between sub-graphs. The multiple optimal surfaces could be solved simultaneously as a single s/t cut problem

by using a maximum-flow algorithm. One important application of optimal surface approach is multiple intra-retinal layer segmentation in 3D OCT images [7].

2.6 Advanced Graph-based Algorithm

Layered optimal graph image segmentation of multiple objects and surfaces (LOGISMOS): LOGISMOS is a general graph-based approach reported by Yin *et al.* [56] for segmenting multiple surfaces that mutually interact within multiple objects (including single object and single surface). The problem is modeled by one graph consisted of multiple sub-graphs in which internal relationships, such as smoothness or shape information, of single object or surface are represented solution-related costs among individual graph nodes. Intra-surface, inter-surface, and inter-object relationships are represented as context specified graph arc weights. A single graph holding all relationships and surface cost elements is constructed in LOGISMOS, and in which the segmentation of all desired surfaces and objects is performed simultaneously in a single st-cut optimization process. To solve multi-object-multi-surface segmentation tasks are common in medical imaging analysis. In OCT images from diseased eyes, particularly in AMD scans, various abnormalities and retinal layers construct the multi-object-multi-layer environment for LOGISMOS method.

Graph-based method with shape and context priors: Graph-based method with shape and context priors is an nontrivial extension of the previously reported graph search framework – optimal surface approach, in which the energy

function was formulated using weighted nodes in the graph. However, this original framework may only consider the internal properties from image; useful prior information may not be considered. The prior information of context and shape was first introduced by Song *et al.* in a study of bladder and prostate detection [57]. Additional terms are added to the energy function, which encode the prior information using weighted arcs in the graph, encouraging the segmentation to realize the prior models. A globally optimal solution (st-cut) is computed by solving a single maximum flow problem in the graph, defining the optimal solution in the source N-dimensional image.

CHAPTER 3
AUTOMATED SEGMENTATION OF CHOROID

In this Chapter, we will introduce two distinctive methods for segmenting the choroidal vasculature and the boundaries of choroid layers (Aim 1). In Section 3.1, a Hessian-analysis based method is developed to generate the segmentation of the choroidal vasculature, providing a robust way of assessing the choroidal vessel volume and density in normal or diseased eyes. This work was published in *Investigative Ophthalmology and Visual Science, 2012* [28]. In Section 3.2, a graph-based method proposes a 3D fully automated segmentation of the choroidal boundaries, catering for the growing needs for the quantitative analysis of choroidal thickness over all frames in the OCT images. This work was published in *Investigative Ophthalmology and Visual Science, 2015* [58].

3.1 Automated Segmentation of the Choroidal Vasculature from Clinical SD-OCT

Abstract

Purpose: To develop and evaluate a fully automated three-dimensional method for segmentation of the choroidal vessels, quantification of choroidal vasculature thickness and choriocapillaris-equivalent thickness of the macula, and evaluate repeat variability in normal subjects using standard clinically available SD-OCT.

Methods: normal subjects (24) were imaged twice, using clinically available, 3D spectral-domain optical coherence tomography (Cirrus, Carl-Zeiss, Dublin, CA).

A novel, fully-automated three-dimensional method was used to segment and visualize the choroidal vasculature in macular scans. Local choroidal vasculature and choriocapillaris-equivalent thicknesses were determined. Reproducibility on repeat imaging was analyzed using overlapping rates, Dice coefficient, and Root Mean Square Coefficient of Variation (CV) of choroidal vasculature and choriocapillaris-equivalent thicknesses.

Results: For the $6\times6\ mm^2$ macula-centered region as depicted by the SD-OCT , average choroidal vasculature thickness in normal subjects was $172.1\mu m$ (95% CI, 163.7-180.5μm) and average choriocapillaris-equivalent thickness was $23.1\mu m$ (95% CI, 20.0-26.2μm). Overlapping rates were 0.79 ± 0.07 and 0.75 ± 0.06, Dice coefficient was 0.78 ± 0.08, CV of choroidal vasculature thickness was 8.0% (95% CI, 6.3%-9.4%), and of choriocapillaris-equivalent thickness, 27.9% (95% CI, 21.0%-33.3%).

Conclusion: Fully automated three-dimensional segmentation and quantitative analysis of the choroidal vasculature and choriocapillaris-equivalent thickness demonstrated excellent reproducibility in repeat scans (CV 8.0%) and good reproducibility of choriocapillaris-equivalent thickness (CV 27.9%). Our method has a potential to improve the diagnosis and management of patients with eye diseases in which the choroid is affected.

Introduction

The choroid is a vascular plexus between the retina and the sclera, forms a vascular system with the highest flow of any tissue in the human body, and is crucial

for oxygenation and metabolic activity of the RPE and outer retina [24]. Anatomically, the choroid can be divided into two principal components: the choriocapillaris, a lobular, vascular plexus comprised of large fenestrated capillaries adjacent to Bruch's membrane, and the choroidal stroma [59]. Most of the choroidal vasculature thickness is attributable to the choroidal stroma, which is comprised of larger vessels that supply and drain the choriocapillaris, as well as melanocytes, fibroblasts, immune cells, neurons, and ground substance that contribute to its thickness [24].

The choroid is affected in many diseases of the retina [60]. Changes in the health of the choroid have been documented in both early macular degeneration and in advanced disease [61, 62, 63]. Decreased choroidal vasculature thickness has been described in age-related macular degeneration [64] although it has not been universally observed. Some choroidal thinning occurs during normal aging, and is seen acutely in some patients in a condition referred to as age-related choroidal atrophy [27]. Other conditions such as central serous retinopathy [25], polypoidal choroidal vasculopathy, and inflammatory conditions such as in choroiditis and autoimmune diseases are associated with thickening of the choroid.

Historically, imaging the choroid in patients was possible with Indocyanine Green Angiography, where injection of this fluorescent dye and subsequent imaging of fluorescence allowed two-dimensional imaging of the choroid pattern and the existence of leakage and vessel wall abnormalities [65]. ICG may be clinically useful in a range of choroidal diseases, though recent studies have failed to demonstrate this [66]. However it does not depict the three-dimensional structure of the choroid.

Several studies have therefore used spectral domain OCT, which allows 3-dimensional imaging of the posterior eye, including the choroid [67], and used manual or semi-manual methods to quantify choroidal vasculature thickness [33, 68]. However, such methods suffer from large intra- and inter-observer variability, and do not have access to the choriocapillaris separately. We have previously developed and validated fully automated, highly robust and three-dimensional segmentation of retinal structures [51].

The purpose of the present study was to develop and evaluate a fully automated three-dimensional method for segmentation of the choroidal vessels, quantification of choroidal vasculature thickness and choriocapillaris-equivalent thicknesses of the macula in normal subjects, using standard clinically available SD-OCT.

Methods

Subject and Data Collection

Normal subjects were recruited by advertising, and included in this prospective study after written informed consent. All subjects were imaged twice on the same day, and macula-centered SD-OCT volumes (Zeiss Cirrus, Carl Zeiss Meditec, Inc., Dublin, CA) were obtained from each subject in both eyes; a single eye was selected randomly for further analysis. Each volume was 200(width of B-scan)×200(number of B-scans)×1024(depth, or height of B-scan) voxels, corresponding to physical dimensions of 6×6×2 mm^3, and voxel size was 30×30×2 μm^3. Volume scan data were de-identified before further image analysis. Institutional Review Board of the Univer-

sity of Iowa gave approval to the study which adhered to the tenets of the Declaration of Helsinki.

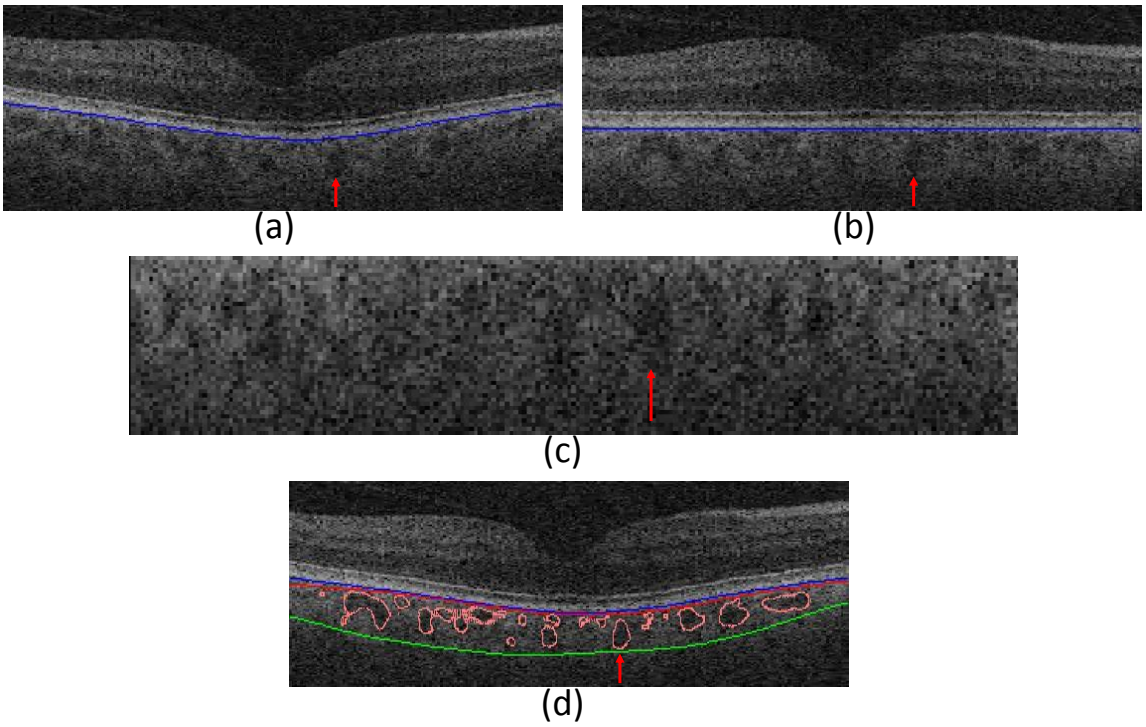

Figure 3.1: Choroidal vasculature in standard clinical OCT scan, central B-scan shown. (a) Original OCT volume with segmented Bruch's membrane (blue line). (b) Flattened OCT volume with segmented Bruch's membrane. (c) Sub-volume under Bruch's membrane containing the entire choroid. (d) Original OCT volume with superimposed segmented vessels (pink outlines), segmented Bruch's membrane (blue line) and the top (red line) and bottom surfaces (green line) fitting around the choroidal vasculature, used to determine choroidal vasculature thickness and choriocapillaris-equivalent thickness. Red arrow points to one of the choroidal vessels.

OCT Volume Flattening and Choroidal Layer Extracting

Due to the relative position of the OCT scanner and patient's pupil, and the possible eye movement, the raw OCT image data are deformed randomly. To reduce the geometric distortion of the choroidal layer, a volume flattening process was needed. Thus, the OCT volume was first automatically segmented using our reported graph-based multi-layer segmentation approach [69], which produced the segmentation result of eleven intra-retinal surfaces including Bruch's membrane (BM), see Figure 3.1(a). The entire raw OCT volume was then flattened based on the segmented BM surface (see Figure 3.1(b)). The choroidal layer was assigned the position beneath the Bruch's membrane. A sufficiently large sub-volume containing choroidal layer (see Figure 3.1(c)) was selected as the target region to employ our choroidal vasculature segmentation method.

Pre-processing of SD-OCT Volumes

Due to the OCT imaging physics, silhouettes occur in the regions under the retinal vessels, see Figure 3.2(a). We introduced a three-stage approach to change the contrast of the silhouette regions in the choroidal layer and to reduce the likelihood of incorrect segmentation due to retinal vessel silhouettes. In the first stage, two of the eleven segmented surfaces, as labeled in Figure 3.2(b), were used to define the retinal pigment epithelium complex (RPE). From top to bottom, the yellow-marked surface is between the inner segment layer and connecting cilia, and the green-marked surface is Bruch's membrane. In the second stage, a projection image was created by computing

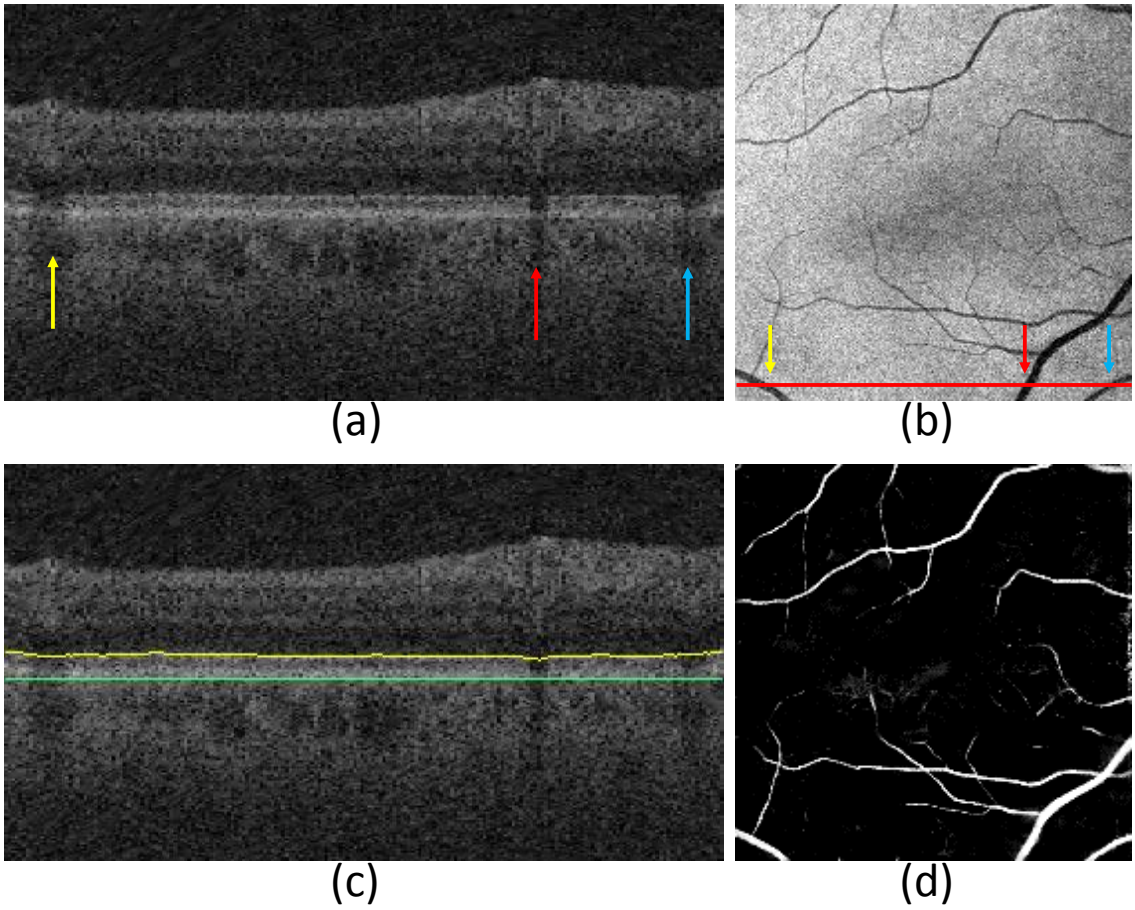

Figure 3.2: Detection of retinal vessel silhouettes. (a) Example x-z slice with retinal vessel silhouettes (colored arrows). (b) Projection image defined by the mean intensity value inside the RPE along the z direction showing vessel silhouettes (same as in a). (c) Reference surfaces (yellow and green lines). (d) 2D retinal vesselness map.

the mean intensity values of voxels within the RPE (see Figure 3.2(c)). Retinal vessel silhouettes were then segmented using our previous retinal vessel segmentation approach [70], Figure 3.2(d). The retinal vessel silhouettes are visible in both the RPE and choroidal layers. As such, the retinal vessel silhouettes must be identified

and distinguished from the similar-looking signatures of choroidal vessels. Therefore, in the third stage, the identified retinal vessel silhouettes were used as a mask, based on which the contrast of the OCT data was smoothed so that the retinal vessels would not show among the identified choroidal vessels.

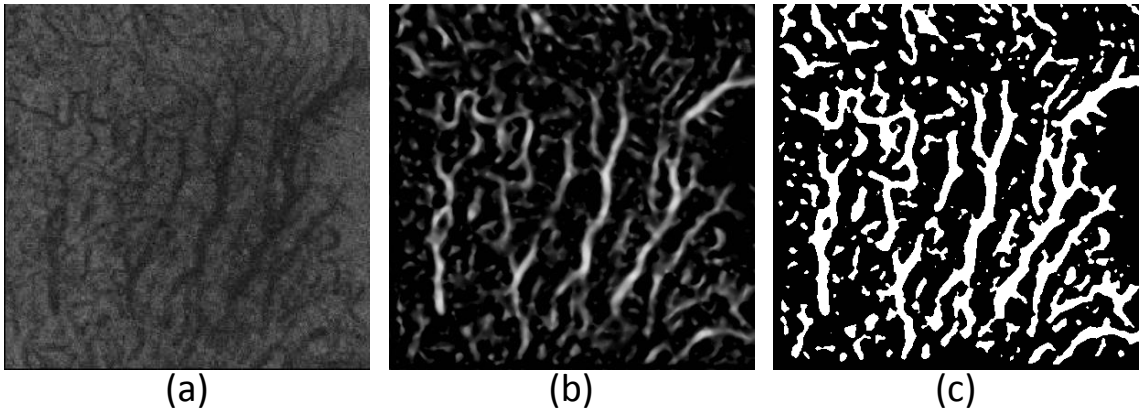

Figure 3.3: Choroidal vasculature segmentation compared to projection of the flattened choroidal layer. (a) An x-y projection view of flattened data. (b) Corresponding x-y projection at the same z-level of the vesselness map. (c) Corresponding x-y projection at the same z-level of the choroidal vasculature segmentation.

Choroidal Vasculature Segmentation

The choroidal vasculature segmentation consists of two main steps: vessel detection and vessel segmentation. In the vessel detection step, choroidal vessels were modeled as 3D tube-like objects in a resampled sub-volume that yielded isometric

(cubic) voxels. To detect choroidal vessel voxels, we applied a multi-scale Hessian matrix analysis [71, 72, 73] on the selected sub-volume: a 3 by 3 tensor matrix was generated for each voxel, containing local directionality and shape information. The vesselness map of the choroidal vasculature was then calculated using the eigenvectors of the tensor matrix at each voxel position. For the second main step of vessel segmentation, voxel groups with relatively high vesselness values were selected by thresholding of the vesselness map using an experimentally-determined threshold that was fixed for all analyzed images. Varying this threshold gave close-to equivalent results over a large range of values. The resulting binary regions were used as seeds for a classic region growing approach to segment the choroidal vasculature, see Figures 3.1(d) and 3.3.

Choroidal and Choriocapillaris-equivalent Thickness Maps

After choroidal vasculature segmentation, a Thin Plate Spline (TPS) approach [74] is applied to the flattened segmentation result to envelop the upper and lower surfaces of the choroidal vasculature segmentation result, see Figure 3.4. The choroidal vasculature thickness is defined as the Euclidean distance between these two surfaces. To measure the choriocapillaris-equivalent thickness, Bruch's membrane surface is used as a reference surface for the boundary of the entire choroid including the choriocapillaris. The choriocapillaris-equivalent thickness is then defined as the distance between Bruch's membrane and the upper surface of the choroid-equivalent region as defined above. Finally, the choroidal vasculature thickness was defined as

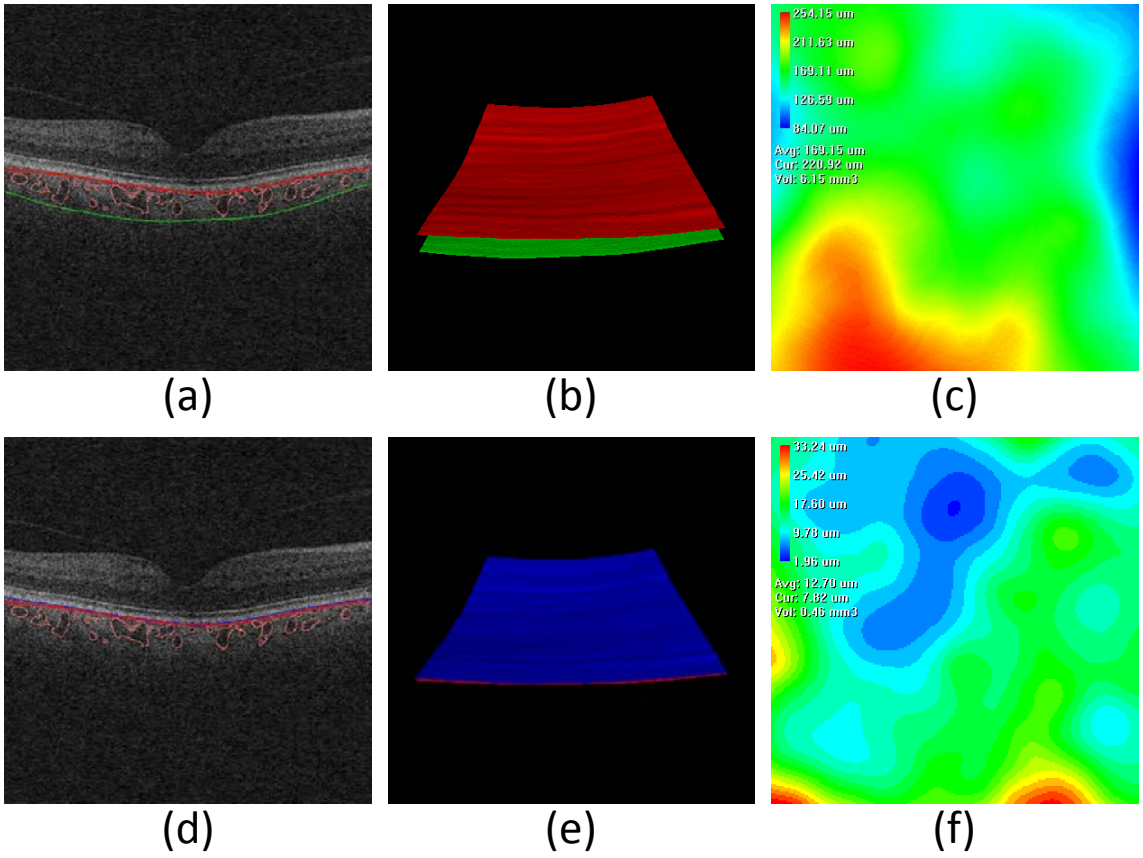

Figure 3.4: Upper and lower surfaces of the choroidal vasculature, used to determine choroidal vasculature thickness and choriocapillaris-equivalent thickness. (a) Upper surface and lower surface of the segmented choroidal vasculature in one B-scan. (b) 3D visualization of the two surfaces as shown in (a). (c) Map of choroidal vasculature thickness. (d) Bruch's membrane and the upper surface of the segmented choroidal vasculature, indicating the boundaries of the choriocapillaris-equivalent region. (e) 3D visualization of the two surfaces shown in (d). (f) Choriocapillaris-equivalent thickness map.

the distance between Bruch's membrane and the lower surface of the choroidal vasculature. Choroidal vasculature and choriocapillaris-equivalent thickness maps were created for all subjects. The relationship of age to choroidal vasculature thickness and choriocapillaris-equivalent thickness was analyzed using scatter plots. Coefficients of variation were calculated using the root mean square (RMS) approach, and mean and 95% confidence intervals are reported. We calculated the volume (inmm^3) of the choroidal vasculature in the 6×6 mm^2 macula-centered region to evaluate the segmentation quality.

Reproducibility Analysis of the Choroidal vasculature Segmentation

Reproducibility analysis of the choroidal vasculature segmentation was performed on repeat scans of the same eye. To align the corresponding volumes from the same subject for further analysis, the two volumetric scans were registered automatically using two-dimensional retinal vessel segmentation and affine registration (Niemeijer M, et al. IOVS 2011;52:ARVO E-Abstract 1304) , see Figure 3.5. After the volumes were registered for each subject, three reproducibility indices of the choroidal vessel segmentation were introduced: overlapping rate, skeletonized overlapping rate, and Dice coefficient. These three indices yield unity for the best reproducibility and null for the worst reproducibility; their definitions follow.

Overlapping rate

Overlapping rate $Overlap_{total}$ was computed from the two choroidal vascula-

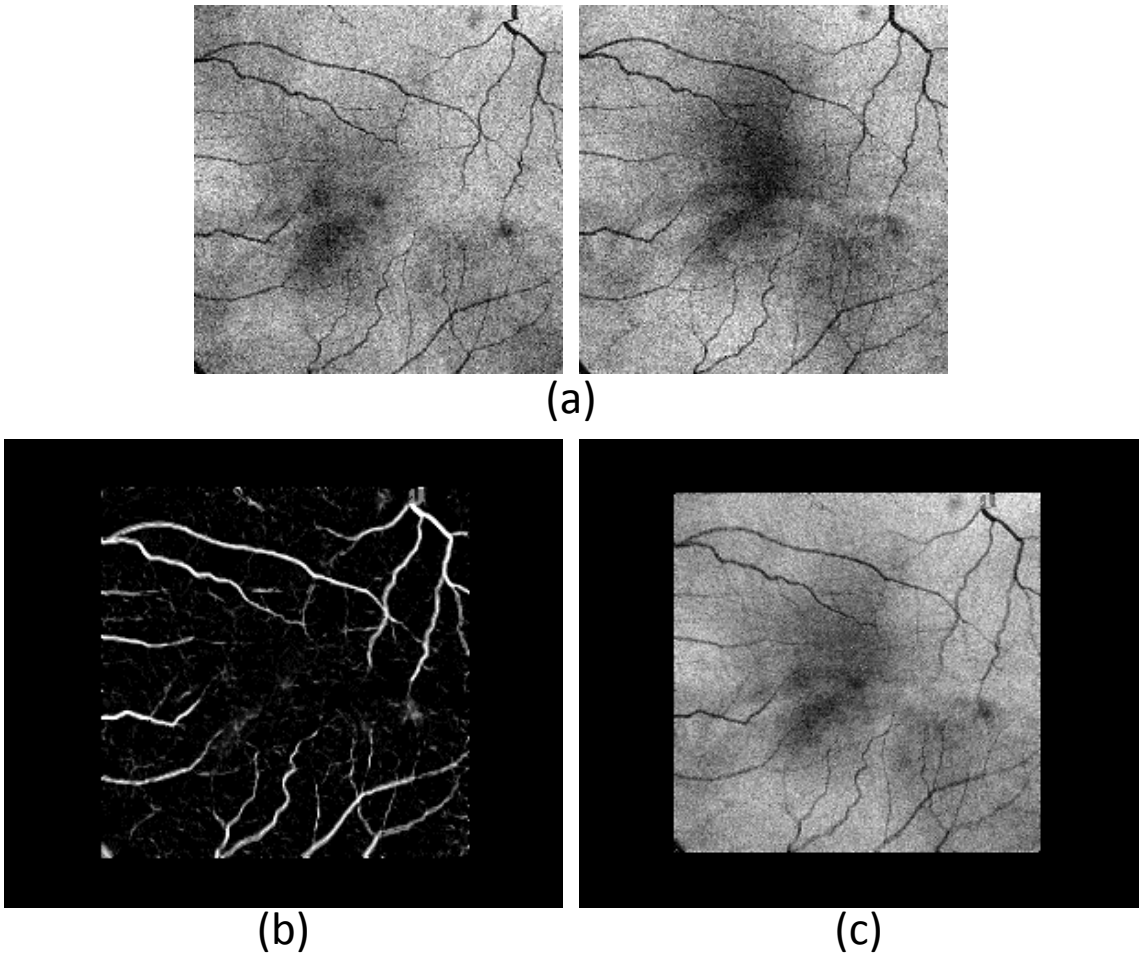

Figure 3.5: Automated retinal vessel based registration. (a) Two OCT projection images from two sequentially-obtained datasets of the same subject. (b) Registration of the retinal vessel segmentation, showing almost perfect match. (c) Registration of the two OCT projection images from two imaging sessions.

ture segmentation results as

$$Overlap_{1st} = \frac{|Vol_{1st}| \cap |Vol_{2nd}|}{|Vol_1 st|}$$

$$Overlap_{2nd} = \frac{|Vol_{1st}| \cap |Vol_{2nd}|}{|Vol_2 nd|}$$

$$Overlap_{total} = \frac{Overlap_{1st} + Overlap_{2nd}}{2}$$

where $|Vol_{1st}|$ represents the choroidal vasculature segmentation result of the first imaging session data; $|Vol_{2nd}|$ represents the choroidal vasculature segmentation result of the second session data.

Skeletonized overlapping rate

To further evaluate the accuracy of the proposed method, central lines of the choroidal vasculature segmentation (skeletons) were generated by using the Insight Segmentation and Registration Toolkit (http://www.itk.org/). Even though the two volumes were registered, slight shift errors may still occur. Although non-affine registration can correct such errors, the required warping of one volume would result in overestimating the correctness of the registration. Therefore, we only used affine registration (translation and rotation) and introduced a narrow-neighborhood band of insensitivity to disregard these small distances between the skeletonization results caused by imperfect registration.

Dice coefficient

The Dice coefficient [75] of the overlap between the two choroidal vasculature segmentation results was also calculated, as yet another metric. The Dice coefficient is defined as follows:

$$DiceCoef = \frac{2(|Vol_{1st}| \cap |Vol_{2nd}|)}{|Vol_{1st}| + |Vol_{2nd}|}$$

where $|Vol_{1st}|$ and $|Vol_{2nd}|$ were defined above.

Results

43 normal subjects were repeat scanned, and in 24/43 subjects, choroidal vessel fraction and the volume of choroidal vasculature in both repeat scans were sufficient for further analysis, even where visual inspection shows little detail of the choroidal vessels in B-scans, see Figure 3.1(d). In these 24 subjects, average volume of choroidal vasculature was $1.12mm^3$ (95%CI, $1.04mm^3$-$1.19mm^3$), and they were included in the study. In 19/43 subjects, one or both repeat scans had insufficient volume of the choroidal vasculature and these subjects were excluded from the study; average volume of choroidal vasculature was 0.58mm3 (95%CI, $0.48mm^3$-$0.67mm^3$). Mean age for the 24 subjects where both scans could be analyzed was 43.96 ($\pm$ stddev 19.18, min 11 years, max 75 years), 5 were male, 19 female. Choroidal vasculature segmentation was applied to all volume sets. Figure 3.6(a-c) shows the x-y slice (projection direction) examples of the flattened sub-volume and vessel segmentation result. Figure 3.6(d) shows a 3D visualization example of the choroidal vasculature segmentation. The minimal diameter of choroidal vessels thus segmented was approximately 60 μm, and the maximal diameter approximately $180\mu m$. The volume of choroidal vasculature in OCT scans that can currently be successfully analyzed by our method is different from those that contain OCT image data unsuitable for analysis, and Figure 3.7 shows an example of one of the scans from the 19/43 subjects where the volume of the detected vasculature are markedly and quantifiably lower than those of analyzable OCT images, such as Figure 3.6(d).

For the 6×6 mm^2 macula-centered region as imaged by the SD-OCT, average

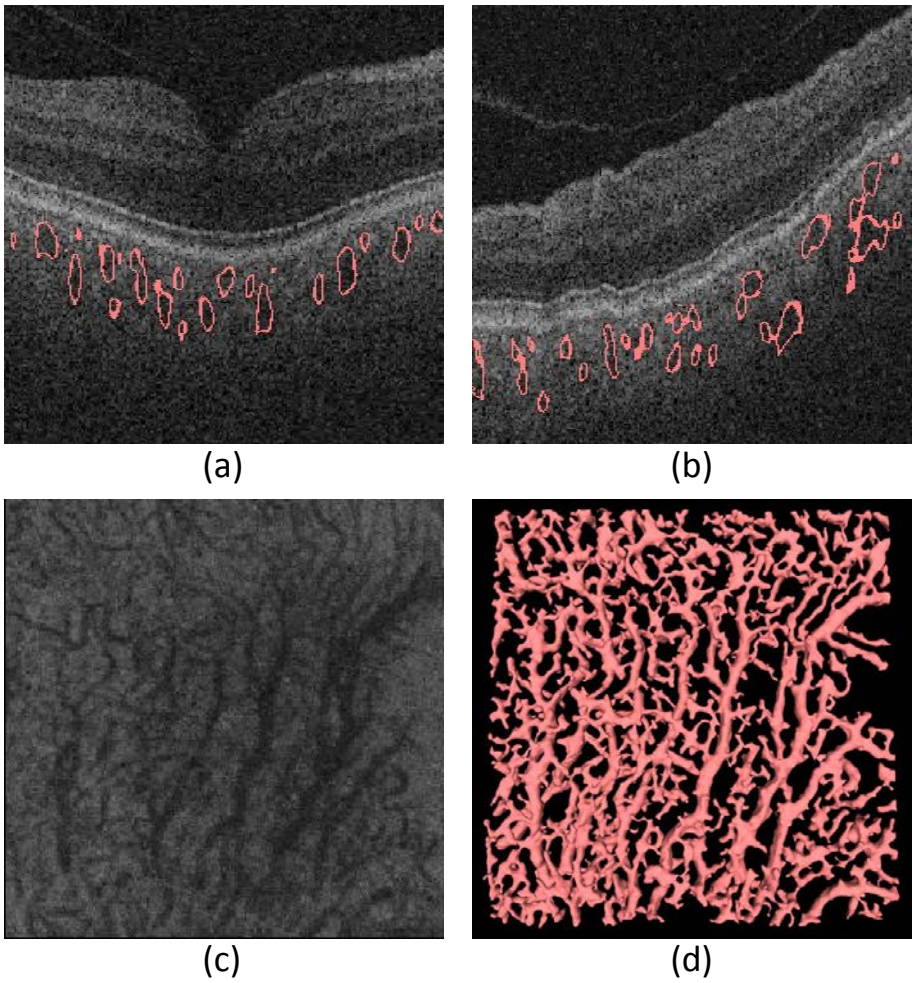

Figure 3.6: Visualization of choroidal vessel segmentation. Panels (a) and (b) show example x-z and y-z slices of the vessel segmentation result. (c) Example x-y slice of flattened OCT volume. (d) Surface rendering of 3-D segmented choroidal vasculature. The volume of the choroidal vasculature is 1.15 mm^3.

choroidal vasculature thickness was 172.1 μm (95% CI, 163.7-180.5μm), and average choriocapillaris-equivalent thickness was 23.1 μm (95% CI, 20.0-26.2μm). These values are comparable to histological findings of human choriocapillaris [61, 62]. The

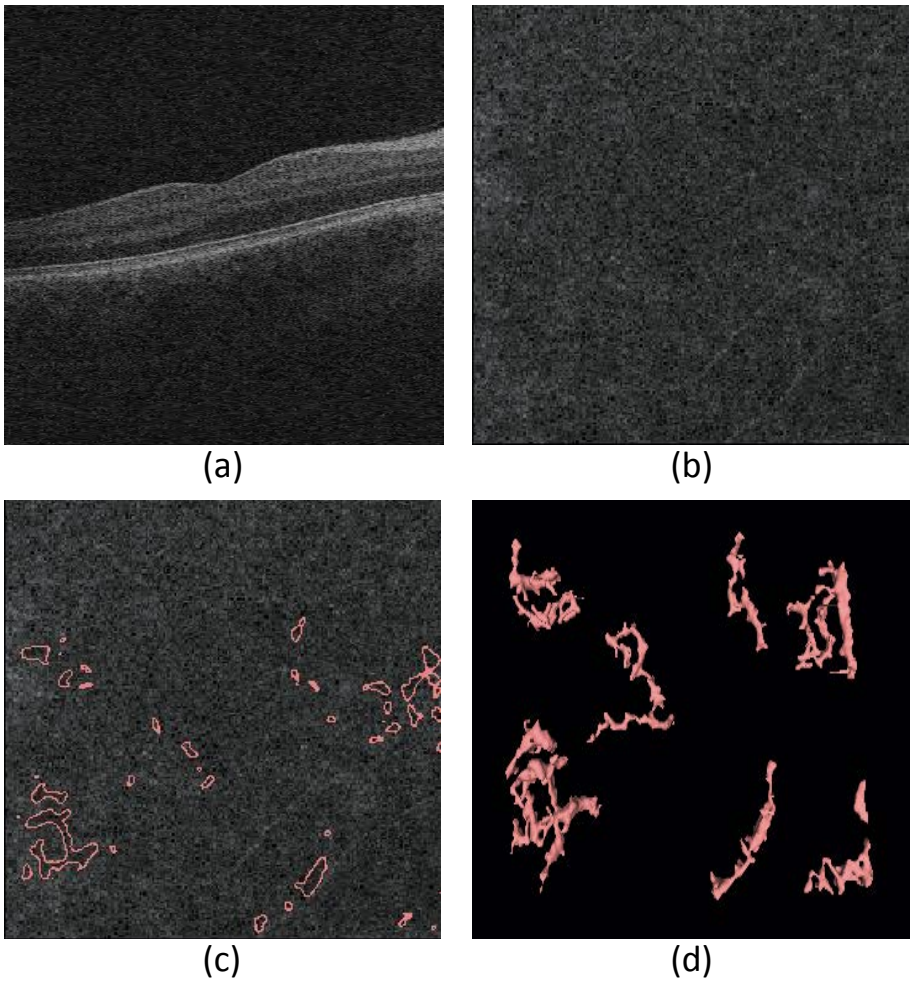

Figure 3.7: Example of OCT data with low volume of choroidal vasculature, unsuitable for segmentation and analysis of choroidal vasculature. (a) Central B-scan. (b) Example x-y slice of flattened OCT volume. (c,d) Silhouettes and surface rendering of the 3-D segmentation of choroidal vasculature. Note the low volume of detected vessels compared with Fig. 6(d). This low volume of choroidal vasculature are used for automated labeling of non-analyzable scans. The volume of the choroidal vasculature is 0.19 mm^3.

scatter plots of average choroidal vasculature thickness and average choriocapillaris-equivalent thickness are in Figure 3.8. In this small set of normal subjects, choroidal vasculature thickness decreased with age at a rate of 0.72 μm per year, and choriocapill-aris-equivalent thickness decreased at 0.25 μm per year.

Reproducibility tests were applied to all 24 subjects, see Figure 3.9. In all cases, a 2-pixel narrow band of distance insensitivity was used. The average overlapping rate was 0.79 $\pm$ 0.07. The mean skeletonized overlapping rate was 0.75 $\pm$ 0.06. Average Dice coefficient was 0.78 $\pm$ 0.08. Choroidal vasculature thickness RMS Coefficient of Variation (CV) was 8.0% (95% CI, 6.3%-9.4%), while choriocapillaris-equivalent thickness CV was 27.9% (95% CI, 21.0%-33.3%).

Discussion

The results of the presented pilot study show a fully automated three-dimensional method capable of segmenting the choroidal vessels, as well as of quantifying choroidal vasculature thickness and choriocapillaris-equivalent thickness. Volume of the choroidal vasculature allowed automatic separation of those subjects in which the OCT image quality was too low to detect any choroidal vessels. The method works on standard clinically available SD-OCTs devices, in this study the Zeiss Cirrus. The reproducibility of the automated method was high, as shown by overlapping and skeletonized overlapping rates of 0.79 and 0.75, Dice coefficient of 0.78, and coefficients of variation of 8.0% for choroidal vasculature thickness. Choriocapillaris-equivalent thickness measures were more variable with an average coefficient of varia-

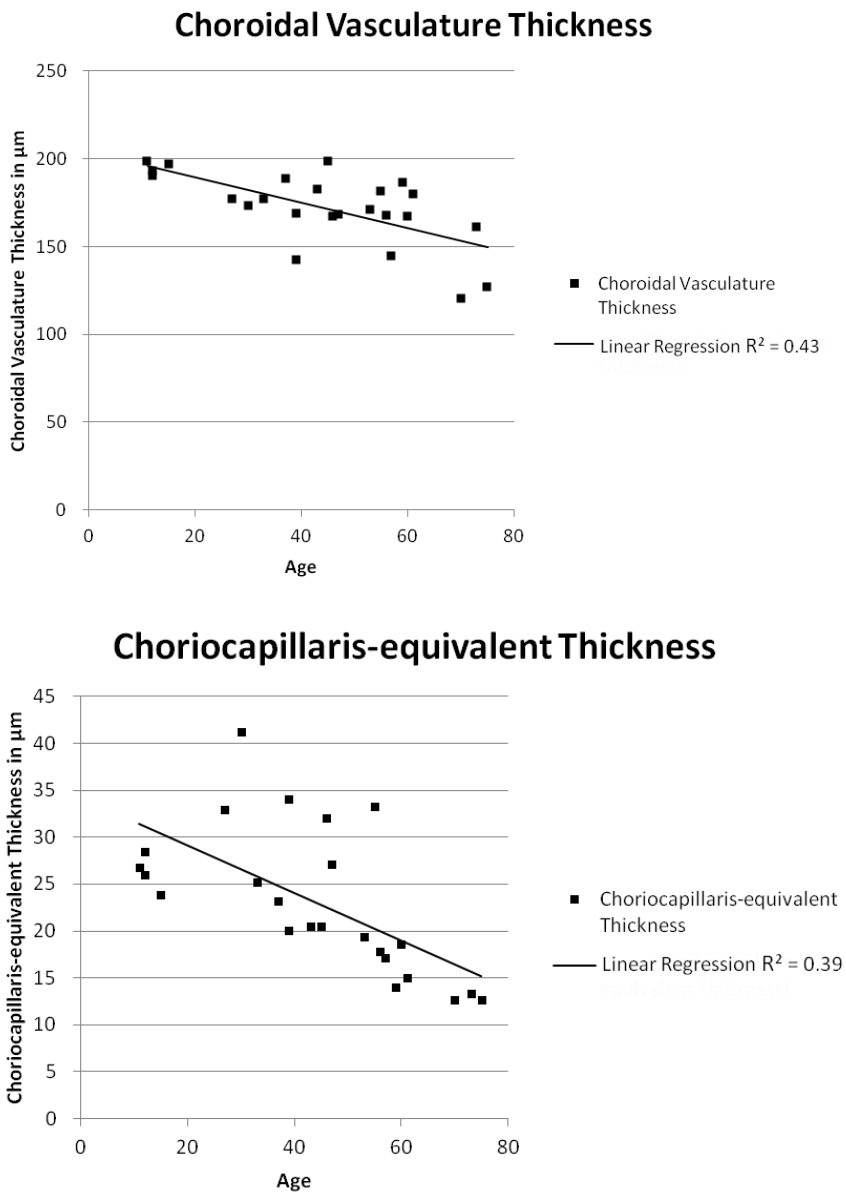

Figure 3.8: Relationship of choroidal vasculature thickness(top) and choriocapillaris-equivalent thickness (bottom) to age in normal subjects.

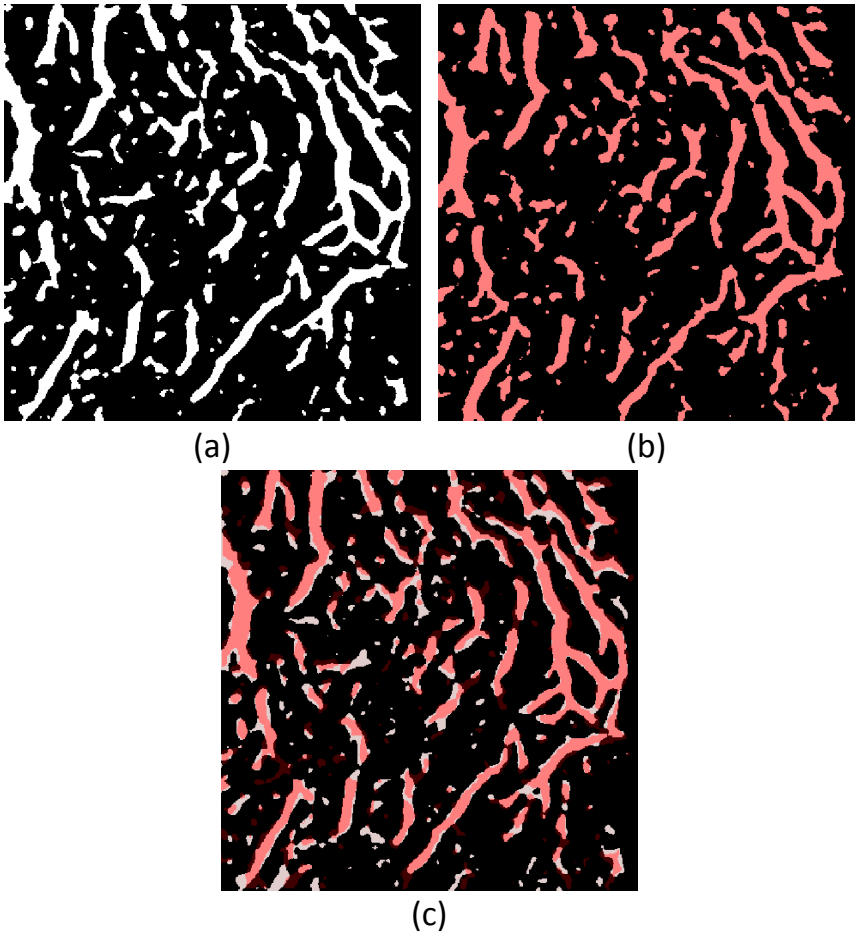

Figure 3.9: Overlapping analysis of reproducibility of choroidal vasculature segmentation. (a) x-y slice of choroidal vasculature segmentation from the first scan of a subject, choroidal vessels in white. (b) x-y slice at the same z-level of the choroidal vasculature segmentation in the repeat, second, scan of the same subject, after affine registration to the first, with choroidal vessels in red. (c) Overlay of the two choroidal vessel segmentations, where pink areas indicate overlapping choroidal vessels in both scans, black depict areas with no choroidal vessels, and white and red areas where choroidal vasculature was segmented in first and second scans respectively.

tion of 27.9%. We confirmed that choroidal vasculature thickness and choriocapillaris-equivalent thickness decrease with age, as was found in earlier studies (for total thickness) using different manual techniques [63, 33].

To the best of our knowledge, this is the first method to achieve segmentation of the choroid, including OCT equivalents of both the outer choroidal vasculature as well as the choriocapillaris. In standard clinical SD-OCT, with axial resolution of 4-8μm and x-y resolution of no better than 30μm, individual capillaries in the choriocapillaris, while large compared to most capillary beds, cannot be resolved. However using our approach, we can estimate the thickness of a layer that does not contain larger choroidal vessels and is below Bruch's membrane. Though we expect this layer to be similar to the choriocapillaris, we took pains to call it the choriocapillaris-equivalent.

While the clinical utility of segmenting the choroid and measuring the choriocapillaris and choroidal vasculature locally is not clear at this time, as has been shown for ICGA [66], we hypothesize that the present method may clarify some of the inconsistencies in the literature about changes in the choroid in different disease states, since a more precise delineation of the different layers and the regional/local availability of measurements may reveal relationships that are difficult to observe when the entire choroid is summed.

Because we achieve true segmentation of the larger choroidal vessels, our method facilitates their 3-D visualization. The resulting patterns are highly similar to those obtained in indocyanine green (ICG) angiography [76], and those in

postmortem alkaline phosphatase stained preparations and choroidal casts [61, 77].

A major concern in this study has been to validate the method. Though ICGA provides 2D projections of the choroidal vessel pattern, there are ethical concerns with administering ICG to normal subjects, because of the risk for an allergic response, anaphylactic shock, and even death [78]. Fundus photography may occasionally show the choroidal vessel pattern in specific regions, especially in lightly pigmented individuals. In our subjects, the choroidal pattern was rarely visualized well enough to be able to serve for validation. In addition, the OCT scans used in this study cover the area of $6\times6\ mm^2$ centered on the fovea, which usually contains more pigment than the rest of the macula, so that prevents using fluorescein angiography for validation. Though the choroid can be cast in postmortem eyes, the retinal edema that occurs immediately after death prevents obtaining high quality OCT scans, especially of the deeper layers. Thus, instead of comparing the results to an accepted reference standard, in this study we have focused on analyzing the reproducibility of the method, using repeat scans taken on the same day and comparing the segmentations for repeat scans. We conclude that the reproducibility of choroidal vasculature thickness is excellent, while that of the choriocapillaris-equivalent is good. Clearly, our automated method is measuring a real structure, and comparison to well-known choroidal patterns strengthens the idea that the choroidal vasculature is indeed segmented.

Interestingly, our method shows that in the majority of normal subjects, most of the choroidal vasculature in the macula can be segmented successfully in standard clinical SD-OCT, even though cursory examination of B-scans shows very little con-

trast in this region, as shown in Figure 3.1. Because of the large number of B-scans achievable with modern clinical SD-OCT, there is sufficient information for segmentation of the choroidal vessels as long as the 3-D context is utilized. Achieving good performance likely depends on the x-y isotropy of the acquired images, meaning that the A-scans are spaced evenly in all directions, instead of having large numbers of A-scans in one direction and large spaces between the slices in another [79].

Two studies using manual segmentation of OCT have been published. In the first study of 34 normals and 19 patients with cataract, the authors compared choroidal thickness maps, obtained using manual expert segmentation, from standard clinical (Cirrus) OCT and experimental swept source 1000nm OCT device, and showed that swept source OCT results in higher quality maps, especially in eyes with cataract [80]. Our approach for automated segmentation with low inter-visit variability can be expected to also perform better, i.e. fewer failed segmentations, in longer center wavelength OCT scans. The second study, 3 normal subjects were studies using swept source 1000nm, OCT and manually segmented maps of choriocapillaris (CC), Sattler's layer (SL), Haller's layer (HL), and lamina suprachoroid layer (LSL) were obtained successfully [67]. Using our automated approach on SD-OCT images limits the segmentation to what can be visualized, and what we term choriocapillaris equivalent is equivalent to choriocapillaris layer, choroidal vasculature is equivalent to Satller's and Haller's layer, and the lamina suprachoroid layer cannot be visualized at all.

Other studies have also estimated the thickness of the total choroid, between

Bruch's membrane and the outermost part of the choroidal vessels [80]. For example, Shin et al. found that the average thickness of the choroid was 285.9 $\pm$ 53.0 μm, thicker than the 193.1 μm (172.1 $\pm$ 21.0) that we report here [33]. The reason for this discrepancy is likely that Shin et al. measured the choroid as extending from Bruch's' membrane to the sclera, while we only measured the choroid extending as far as the vessel walls closest to the sclera. Thus, tissue of the suprachoroidea, present between the outer vessel walls and the sclera, is not included in our measure of choroidal vasculature thickness. We found that choroidal vasculature thickness decreases at a rate of 0.72 μm per year, which is comparable to 0.97 μm per year found by Shin et al., and 1.4-1.56 μm per year using different approaches of Agawa et al. and Ikuno et al. [81, 82].

There are some limitations to this pilot study of a fully automated three-dimensional method for segmentation of the choroidal vessels. First of all, the number of subjects was relatively small. We are currently pursuing a study in a much larger population, as well as in patients with various retinal abnormalities.

Second, we achieved successful segmentation for two repeat scans in just over half, 24/43 subjects, while in 19/43 subjects needed to be excluded because at least one OCT volume had insufficient image quality for further analysis. Choroidal vessel fraction and the volume of choroidal vasculature allow sufficient OCT quality to be automatically determined. Possibly, Enhanced Depth Imaging and a longer center wavelength (with these scans, 840nm) such as 1040nm, that penetrates deeper, may allow a larger percentage of subjects to be successfully measured [83].

Third, we have only studied reproducibility in normal subjects. In subjects with less normal choroid, such as subjects suffering from macular degeneration or choroiditis, the measurement reproducibility may well be less favorable.

In summary, we have developed and validated a fully automated three-dimensional method capable of segmentation of the choroidal vessels, as well as quantification of choroidal vasculature thickness and choriocapillaris-equivalent thickness. The method works on standard clinically available SD-OCT devices, in this study the Zeiss Cirrus, and has good reproducibility, as shown from the repeat-variability studies. Potentially, our method may improve the diagnosis and management of patients with eye diseases in which the choroid is affected.

3.2 Automated Choroidal Surface Segmentation in SS-OCT and SD-OCT

Abstract

Purpose: To evaluate the validity of a novel fully automated 3D method capable of segmenting the choroid from two different optical coherence tomography scanners: swept-source OCT (SS-OCT) and spectral-domain OCT (SD-OCT).

Methods: One hundred and eight subjects were imaged using SS-OCT and SD-OCT. A 3D method was used to segment the choroid and quantify the choroidal thickness along each A-scan. The segmented choroidal posterior boundary was evaluated by comparing to manual segmentation. Differences were assessed to test the agreement between segmentation results of the same subject. Choroidal thickness was

defined as the Euclidian distance between Bruch's membrane and the choroidal posterior boundary, and reproducibility was analyzed using automatically and manually determined choroidal thicknesses.

Results: For SS-OCT, the average choroidal thickness of the entire 6-by-6 mm^2 macular region was 219.5μm (95% CI, 204.9-234.2μm), and for SD-OCT, that was 209.5μm (95% CI, 197.9-221.0μm). The agreement between automated and manual segmentations was high: average relative difference was less than 5μm and average absolute difference was less than 15μm. Reproducibility of choroidal thickness between repeated SS-OCT scans was high (CV of 3.3%, ICC of 0.98), and differences between SS-OCT and SD-OCT results were small (CV of 11.0%, ICC of 0.73).

Conclusion: We have developed a fully automated 3D method for segmenting the choroid and quantifying choroidal thickness along each A-scan. The method yielded high validity. Our method can be used reliably to study local choroidal changes and may improve the diagnosis and management of patients with ocular diseases in which the choroid is affected.

Introduction

The choroid provides oxygen and nourishment to the outer retinal layers and is crucial for metabolic activity in the retina [24]. Choroidal changes are associated with many eye diseases, such as age-related macular degeneration (AMD) [60], age-related choroidal atrophy [27], central serous retinopathy [25] and choroiditis. It has been also reported that choroidal thickness increases during childhood and decreases dur-

ing adulthood [63, 84]. Accurately and automatically measuring choroidal thickness is therefore of great interest. Spectral domain optical coherence tomography (SD-OCT) provides a cross-sectional, three-dimensional, micro-scale depiction of ocular tissues [5] and clearly distinguishable retinal layers, as shown in Figure 3.10. However, without the use of enhanced-depth imaging or image enhancement techniques, the visualization of the choroid, including choroid-sclera junction, remains challenging (see Figure 3.10). Due to the high backscatter by the retinal pigment epithelium layer (RPE), the intensity contrast in the choroid region can be insufficient for applying straightforward image analysis algorithms.

Swept-source OCT (SS-OCT) allows increased scanning speed [52]. In many SS-OCT prototype systems, a longer central wavelength (1060nm versus 840nm in SD-OCT) is adopted to allow deeper penetration through the RPE. Consequently, the choroid-sclera boundary has higher contrast in SS-OCT (see Figure 3.11). We and others have previously developed fully automated three-dimensional algorithms for segmenting choroid on standard clinically available SD-OCT scans [28, 34, 85, 35, 86, 87]. In our approach, choroidal thickness was estimated by defining the Euclidian distance between the enveloping surfaces of a choroidal vasculature segmentation (see Figure 3.12).

The purpose of this study was to develop and evaluate the validity of a fully automated three-dimensional method capable of segmenting the choroid over the entire scan and quantifying choroidal thicknesses of the macula in both SS-OCT and SD-OCT image data of the same subjects, without a preceding vasculature segmentation

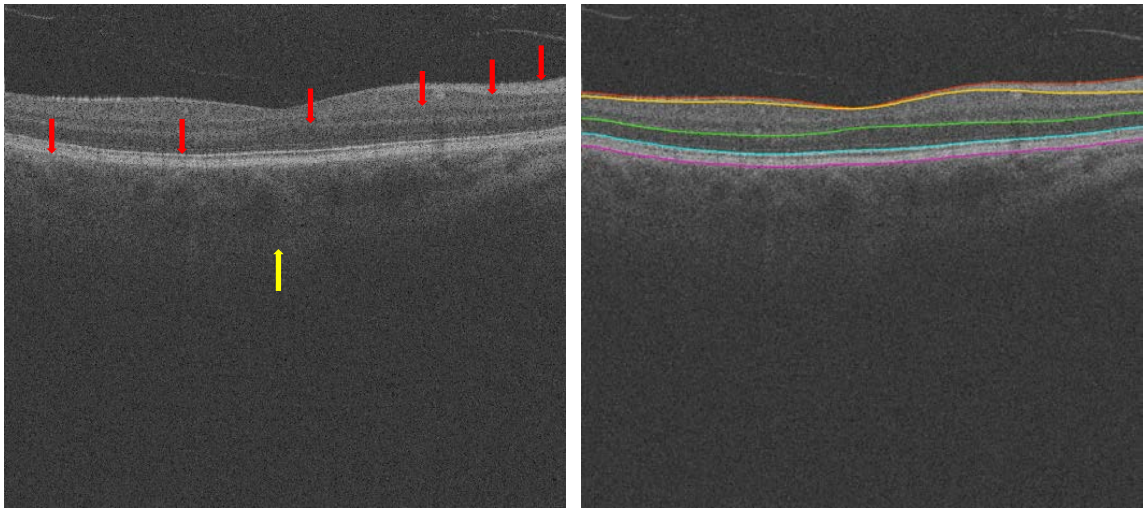

Figure 3.10: In the standard clinically available SD-OCT scans, retinal layer structures are clear (red arrows), but the posterior choroidal boundary is difficult to be distinguished (yellow arrow). In the right panel, the surfaces from top to bottom are: Internal limiting membrane, the transition between retinal nerve fiber layer and ganglion cell layer, outer boundary of outer plexiform layer, boundary of myoid and ellipsoid of inner segments and Bruch's membrane.

step, so that choroidal thickness can be measured for each A-scan.

Method

Subject and Data Collection

The Rotterdam study is a prospective population-based cohort study, which investigates chronic diseases in the middle-aged and elderly [88]. Inhabitants of Ommoord, a suburb of Rotterdam, the Netherlands, were invited to participate in this

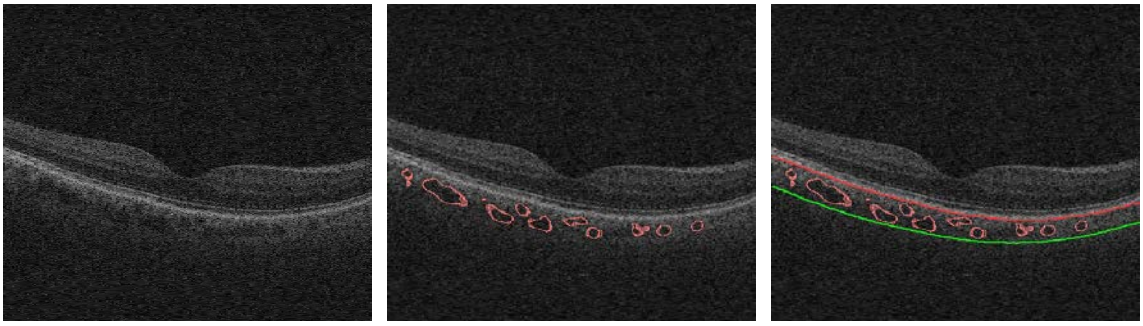

Figure 3.11: Segmentation results from the previous method on clinically available SD-OCT image (Zeiss Cirrus, EDI mode was not used): (a) Original B-scan; (b) 3D choroidal vasculature segmentation; (c) the outer boundary of choroidal vasculature is estimated using thin-plate-spline surface fitting, real segmentation of choroidal-scleral interface was not achieved.

study at three different times: 1989, 2000 and 2006. This resulted in three cohorts: Rotterdam Study I (N=7,983 aged 55 years and older), Rotterdam Study II (N=3,011 aged 55-years and older) and Rotterdam Study III (N=3,982, aged 45 years and older). Follow-up examinations took place every 2-4 years and are still ongoing.

For this study we included one hundred and eight randomly selected subjects from the Rotterdam study II (second follow-up round) and Rotterdam Study III (first follow-up round), whom participated between April 3rd 2013 April 26th 2013. All participants underwent an extensive ophthalmologic examination including swept-source OCT (SS-OCT, Topcon Corp., Tokyo, Japan) and spectral domain-OCT (SD-OCT, Topcon Corp., Tokyo, Japan) imaging. Subjects were imaged on one day,

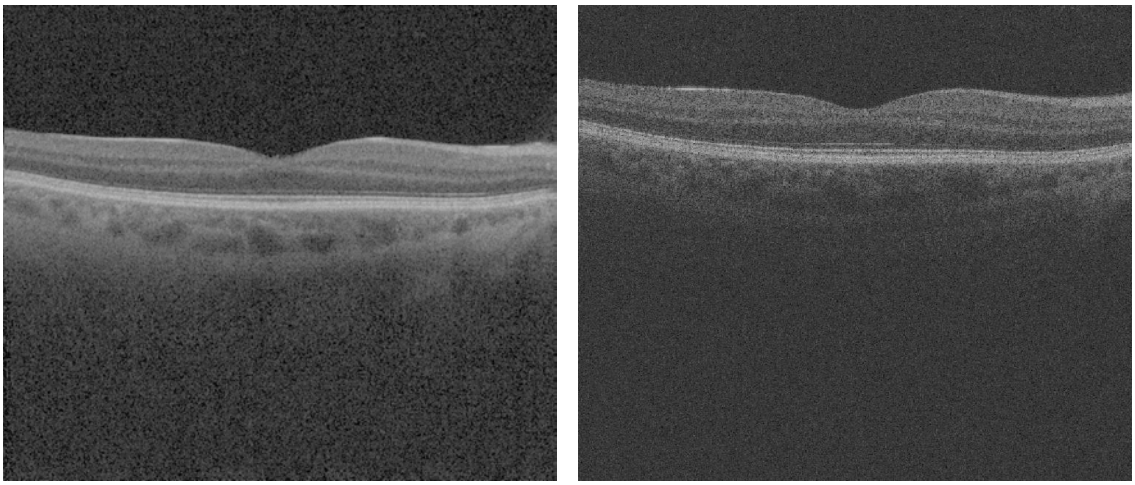

Figure 3.12: Swept-source OCT and Spectral-domain OCT show difference of intensity contrast around choroidal-scleral interface. An example of the difference of intensity contrast at same location from the same eye in (a) SS-OCT image data and in (b) SD-OCT image data.

once using SD-OCT and twice using SS-OCT. Enhanced Depth Imaging (EDI) mode was not used [83]. In between scans, the head was lifted from the chin rest and subjects were asked to relax for no more than 15 minutes. Each volume scan was 512(width of B-scan)×128(number of B-scans)×885(height of B-scan) voxels, corresponding to physical dimensions of approximately $6.0\times6.0\times2.3mm^3$, the voxel size was $11.72\times46.88\times2.60\mu m^3$. The mean age of the 108 subjects was 61.4 ($\pm$ std. dev. of 5.2, range 52-78 years), with 45 male and 63 female subjects (41.7% and 58.3%, respectively). Over 92% of the participants were of European descent. Best corrected visual acuity (BCVA) was measured using the Lighthouse Distance Visual Acuity test,

a corrected Early Treatment Diabetic Retinopathy Study chart (ETDRS Research Group Early Treatment Diabetic Retinopathy Study (ETDRS) Manual of Operations Springfield, VA: National Technical Information Service, 1985; 174.) BCVA was impaired (BCVA $\leq$ 0.50, decimal notation was 20) in three eyes of three subjects due to cataract in two eyes and amblyopia in one eye. Mean spherical equivalent (SphE) was calculated using a standard formula (SphE=spherical value+0.5$\times$cylinder. Mean SphE of the 108 subjects was 0.02 D ($\pm$ std. dev. of 3.8 D, range -10.7 9.6 D). Mean axial eye length (Lenstar, Haag-Streit Diagnostics, Koeniz, Switzerland) was 23.6 mm ($\pm$ std. dev. of 1.2, range 20.80-26.39mm). According to the fundus photographs and OCT scans, none of the included eyes showed retinal pathology in the posterior pole. Volumetric scan data were de-identified before image analysis. The Rotterdam Study has been approved by the Medical Ethics Committee of the Erasmus MC and by the Ministry of Health, Welfare and Sport of the Netherlands, implementing the "Wet Bevolkingsonderzoek: ERGO (Population Studies Act: Rotterdam Study)". All participants provided written informed consent to participate in the study and to obtain information from their treating physicians. De-identified volume scans were transferred to the University of Iowa XNAT image database for offline processing [89]. The study adhered to the tenets of the Declaration of Helsinki.

Choroidal Segmentation

We have developed a three-stage segmentation approach. First, to reduce the geometric distortion of the choroid layer caused by the relative position of the OCT

scanner's optical axis to the subject's optical axis, an angle adjustment approach was applied to the original OCT volume [90], as shown in the Figure 3.13(b). Bruch's membrane (BM) was transformed to a relatively flat surface in the OCT image volume [7]. Second, BM was modeled as a convex arc on each B-scan, and the radius of this convex arc was computed using the average physical size of a human eyeball [91]. A shape-prior based soft-constraint graph-search method was employed to segment BM by utilizing this arc model [42] (see Figure 3.13(c)). In the third stage, the choroid layer was identified immediately beneath Bruch's membrane. A sufficiently large sub-volume containing the choroid layer was selected as the target region to apply choroidal segmentation. A combined graph-cut-graph-search method was utilized to segment choroidal surfaces (see Figure 3.13(d)). Intensity contrast was expected to be present around the choroidal posterior boundary and vertical intensity gradient image was thus used to form the cost functions. To ensure the continuity of the segmented surface, smoothness constraints were adopted between neighboring A-scans. Due to the unequal voxel dimensions in the OCT volume scan (512 voxels in temporal-nasal direction and 128 voxels in superior-inferior direction), anisotropic smoothness constraints were established. More relaxed constraints were applied along the low-resolved direction (superior-inferior) and less relaxed constraints were employed along the high-resolved direction (temporal-nasal). The choroidal posterior boundary was subsequently segmented by graph optimization via identifying the minimum s-t cut in the employed geometric graph. Method details were described in Chapter 5 Section 5.1.

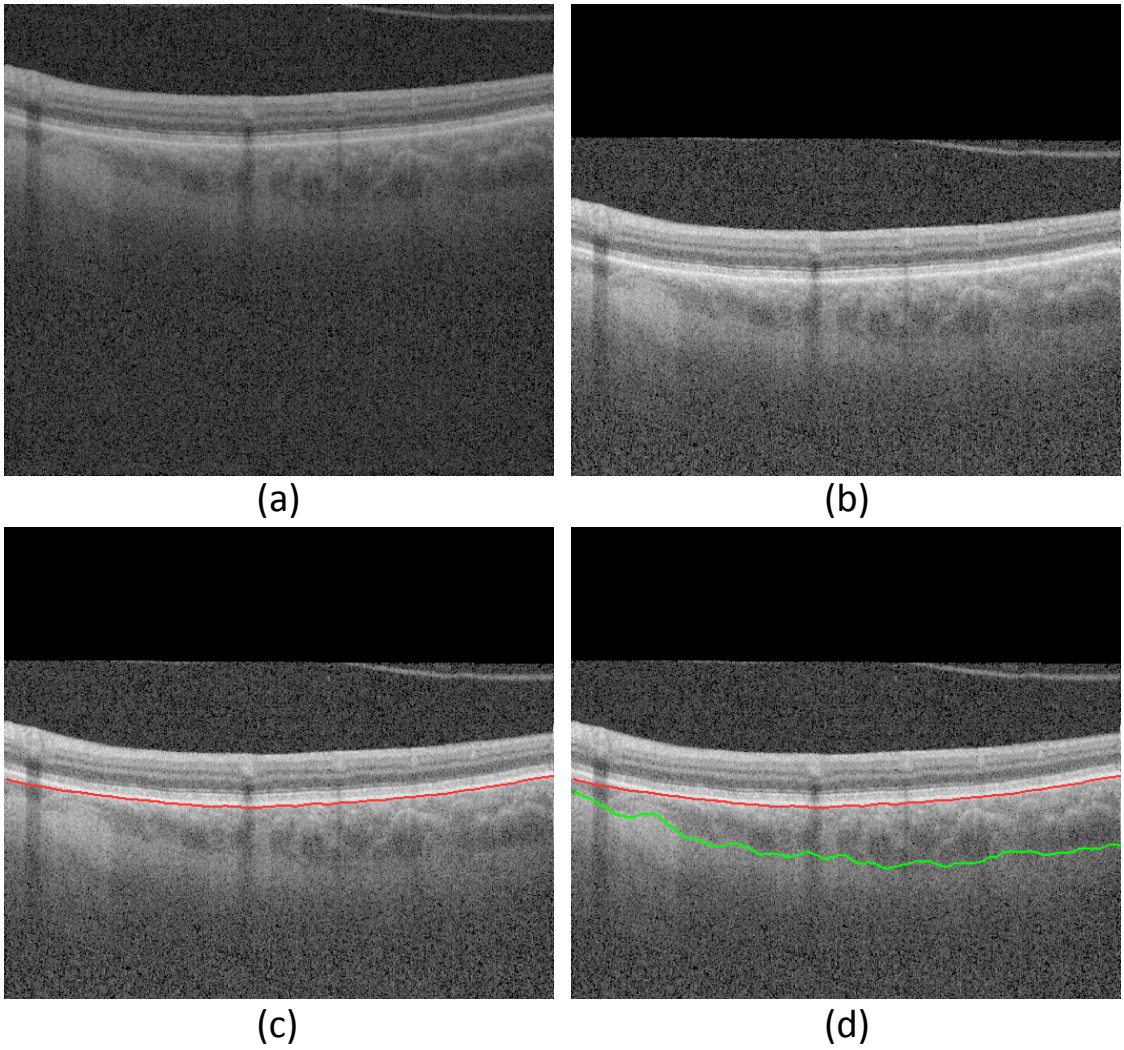

Figure 3.13: Three-dimensional choroidal segmentation using our proposed method: (a) An example B-scan from the original data; (b) The B-scan after applying the angle adjustment; (c) Bruch's membrane segmentation result; (d) Choroidal posterior segmentation result. The red curve is the segmentation of Bruch's membrane; the green curve is the segmentation of choroidal posterior boundary. Though only a single B-scan is showed, the method operates in 3D across all B-scans.

Validation of the choroidal segmentation

The central B-scan and a random B-scan were extracted from each volumetric image. An experienced OCT analyst masked to the algorithm output manually segmented the choroidal posterior boundary on all selected B-scans. For each A-scan, the position of the segmented surface was defined as the depth from the top of the volumetric image in voxel domain. The outcome measure was the absolute and relative differences between the positions of the automated and manual segmentation results of the choroidal posterior boundary on two manually marked B-scans for each volumetric image. The relative difference was defined as automated value minus manual value. Bland-Altman plots were used to assess effect size on discrepancy: the relative differences were plotted against the mean position of automatically and manually segmented surfaces. A 95% limit of agreement (LOA) was defined as the average difference $\pm$ 1.96$\times$standard deviation (std.) of the difference, i.e. the degree of agreement between automatically and manually segmented choroidal posterior boundaries. As described in [92], systematic error (SE) limit and total error (TE) limit were defined. The 95% confidence interval of the relative difference was compared with the pre-defined SE limit and the 95% confidence interval of LOA was comparted with the pre-defined TE limit. In order to further test the systematic bias in the automated algorithm, a paired t-test was performed on the difference between the manual and automated segmentation results. To eliminate the possible systematic bias in the proposed method, a three-fold cross-validation approach [93] was applied on the results of the proposed method.

Thickness assessment

The choroidal thickness was calculated for each A-scan, defined as the Euclidian distance between Bruch's membrane and the posterior surface of the choroid. Choroidal thickness maps for the $6\times6mm^2$ macula-centered region imaged by SS-OCT and SD-OCT scans were then created. The average thicknesses were reported in μm, with 95% confidence intervals (95% CI). In addition to the average choroidal thickness for the $6\times6mm^2$ macula-centered region, the fovea location was automatically detected using the Iowa Reference Algorithm [7] and the subfoveal choroidal thickness was determined.

Reproducibility assessment of the choroidal thickness

For each subject, choroidal thickness was computed from two SS-OCT scans and SD-OCT scan over the entire $6\times6mm^2$ macula-centered region. Reproducibility analysis of the choroidal thickness was performed on the repeated SS-OCT scans and between SS-OCT and SD-OCT scans. To evaluate the test-retest reproducibility in repeated SS-OCT images, coefficients of variation (CV) and intra-class correlation coefficients (ICC) of the average choroidal thicknesses from automated and manual segmentation methods were determined using the root mean square (RMS) approach [81]. Similarly, the RMS CV and ICC between the average choroidal thicknesses from two SS-OCT scans and that of SD-OCT thickness were computed as well. To further test the algorithm on those scans with thicker choroids, subjects with subfoveal choroidal thickness greater than $300\mu m$ were selected to run the validity analyses,

including thickness assessment and reproducibility assessment.

Comparison between proposed method and previous method

We have previously reported an automated method for segmenting choroidal vasculature and estimating the posterior boundary of the choroidal vasculature using Hessian vesselness analysis and thin-plate-spline surface fitting approach in a sequential fashion. In order to compare our new and previous results, we ran our earlier choroidal vasculature based method on this dataset. The absolute and relative differences were computed between the automated segmentation results of the old method and the manual segmentation results. A paired t-test was then used to compare the absolute and relative differences between the new and old methods. A p value of 0.05 was considered significant.

Results

The agreement between automated and manual segmentations was high. The mean standard deviation of the relative differences for the entire dataset (216 SS-OCT images and 108 SD-OCT images), was -4.2±20.5μm (-1.6±7.9 voxels); for the first SS-OCT dataset, the relative difference was -3.9±18.7μm (-1.5±7.2 voxels); for the second SS-OCT dataset, the relative difference was -2.6±19.5μm (-1.0±7.5 voxels); for the SD-OCT dataset, the relative difference was 6.2±22.6μm (-2.4±8.7 voxels).

As shown in the Bland-Altman plots (Figure 3.14), the difference between automated and manual results (automated result minus manual result) is relatively small; about 95% of the difference values are located within the limit of agreement

(LOA). The 95% LOA for the entire dataset (216 SS-OCT images and 108 SD-OCT images) was [-17.0μm, 13.8μm]; for the first SS-OCT dataset, the 95% LOA was [-15.7μm, 12.6μm]; for the second SS-OCT dataset, the 95% LOA was [-15.7μm, 13.8μm]; for the SD-OCT dataset, the 95% LOA was [-19.5μm, 14.8μm].

The mean ± standard deviation of absolute differences for the entire dataset (216 SS-OCT images and 108 SD-OCT images) was 13.8±15.6μm (5.3±6.0 voxels); for the first SS-OCT dataset, the absolute difference was 12.6±14.4μm (4.9±5.5 voxels); for the second SS-OCT dataset, the absolute difference was 12.3±15.4μm (4.7±5.9 voxels); for the SD-OCT dataset, the absolute difference was 16.6±16.6μm (6.4±6.4 voxels).

The mean difference between automated and manual segmentations were significantly smaller than a predefined systematic error (SE) of 3% of average thickness and the 95% LOA's were significantly smaller than a predefined total error (TE) of 10% of average thickness [92]. For the SD-OCT dataset, the mean difference between automated and manual segmentation was significantly less than the SE, but 95% LOA approached the TE with no significant difference (see Figure 3.14).

According to the result of paired t-test between the manual and automated segmentations, a systematic bias was found in our proposed method (mean difference was -4.2μm, $p < 0.01$). As shown in Figure 3.14, the systematic bias was small and did not exceed the predefined systematic error (SE) limit. A three-fold cross-validation approach [93] was then applied on the results of the proposed method. Paired t-test was performed again on the adjusted automated results and manual segmentation

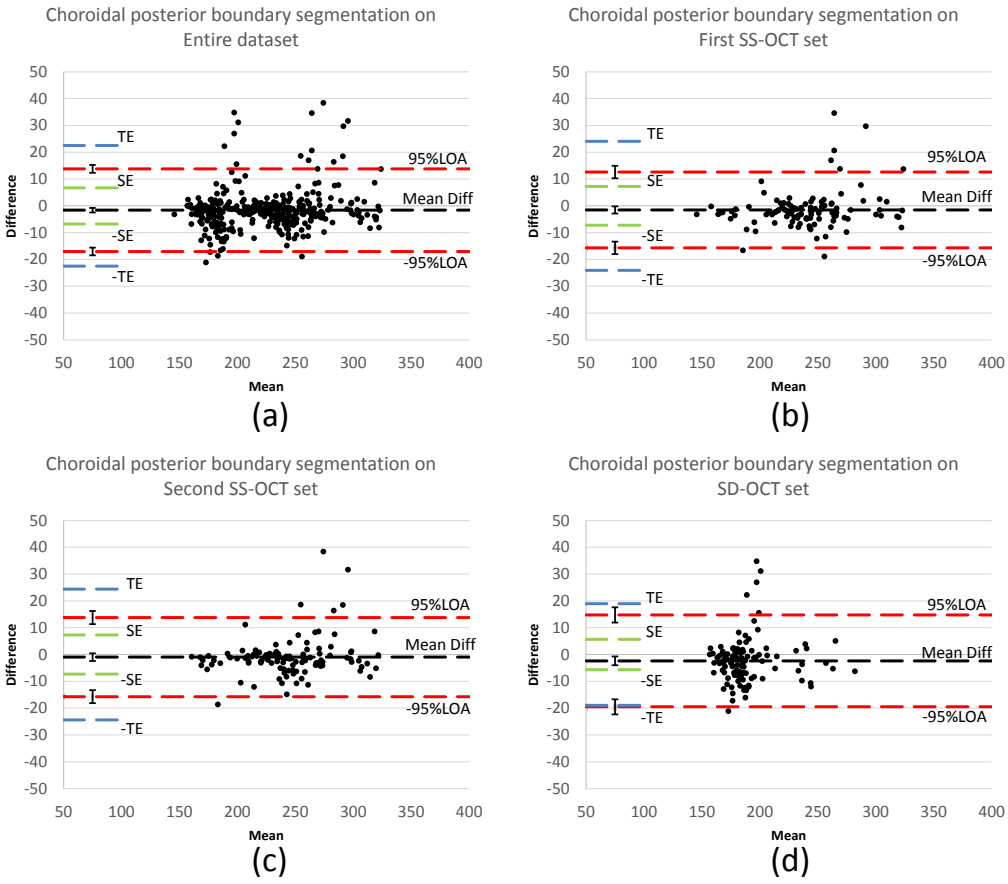

Figure 3.14: Difference assessment between automated and manual segmentations (Bland-Altman plots): (a) on entire datasets: 216 SS-OCT scans and 108 SD-OCT scans; (b) on the first SS-OCT set; (c) on the second SS-OCT set; (d) on the SD-OCT set. Black dashed lines represent the mean of relative difference between automated and manual segmentations and red dashed lines represent the 95% limits of agreement (LOA), 95% confidence interval of the mean difference and 95% LOA are added on the left end of the corresponding dashed lines; blue dashed lines represent the predefined total error (TE) as 10% of the average thickness; green dashed lines represent the redefined systematic error (SE) as 3% of the average thickness.

results and the bias was eliminated ($p = 0.72$).

For the $6{\times}6\ mm^2$ macula-centered region imaged by SS-OCT, average choroidal thickness was $219.5\mu m$ (95% CI, 204.9-234.2μm), and for SD-OCT, was $209.5\mu m$ (95% CI, 197.9-221.0μm), corresponding to subfoveal choroidal thicknesses on SS-OCT of $246.7 \pm 97.9\ \mu m$ (max was $457.6\ \mu m$; min was $83.2\ \mu m$) and on SD-OCT of $229.7 \pm 82.1\ \mu m$; (max was $429.0\ \mu m$; min was $85.8\ \mu m$).

The root mean square coefficient of variation (RMS CV) of the automatically determined average choroidal thickness of repeated SS-OCT scans was 3.3% (95% CI, 2.2%-4.1%) and had an intra-class correlation coefficient (ICC) of 0.98 ($p < 0.001$), see Figure 3.15(a). The reproducibility between the manual segmentation of repeated SS-OCT scans showed an RMS CV of 3.8% (95% CI, 3.2%-4.4%) and ICC of 0.96 ($p < 0.001$) (see Figure 3.15(b)). The automated method was not significantly better than the manual expert ($p = 0.28$). The RMS CV between automatically determined average choroidal thickness of two SS-OCT scans and one SD-OCT scan was 11.0% (95% CI, 8.0%-13.3%) along with an ICC of 0.73 ($p < 0.001$), see Figure 3.16(a). The RMS CV between the manually determined average choroidal thickness of two SS-OCT scans and that of one SD-OCT scan was 9.1% (95% CI, 7.7%-10.3%) with an ICC of 0.75 ($p < 0.001$), see Figure 3.16(b), however these differences between automated and manual segmentation CVs were not significant ($p = 0.24$).

Thirty-six subjects (72 SS-OCT scans and 36 SD-OCT scans) with subfoveal choroidal thickness greater than $300\mu m$ were selected to run the validity analyses. The average subfoveal choroidal thickness on SS-OCT in this subset was $363.8\mu m$

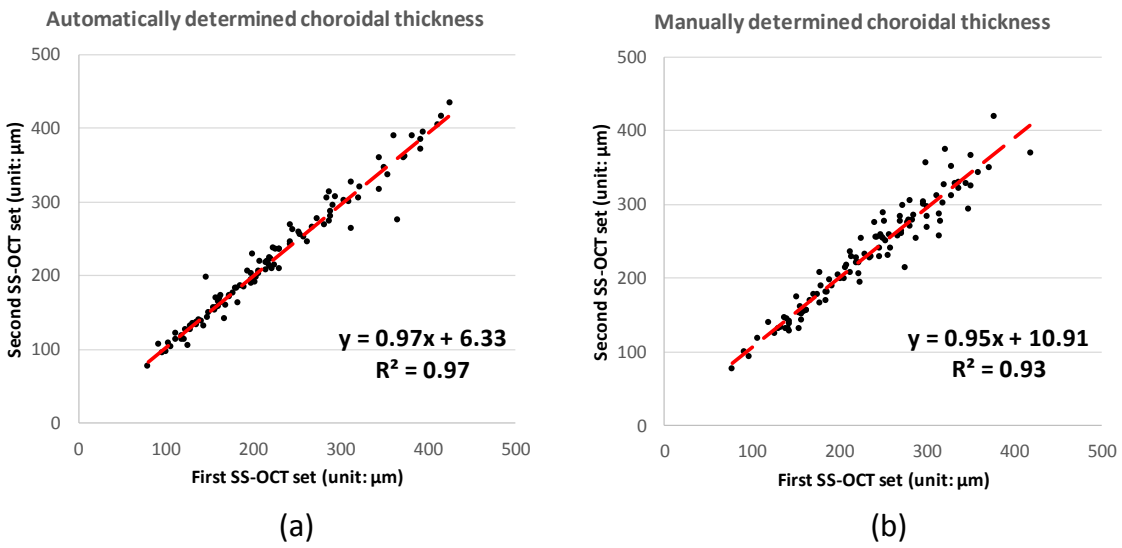

Figure 3.15: Correlation analysis of the choroidal thickness on entire 6-by-6 macular region between SS-OCT repeated scans: (a) automated segmentation; (b) manual segmentation.

(95% CI, 352.6-374.4μm) and was 301.4μm (95% CI, 274.1-328.7μm) on SD-OCT. The average choroidal thickness over the entire 6×6 mm^2 macula-centered region imaged by SS-OCT in this subset was 305.8μm (95% CI, 292.7-318.8μm), and on SD-OCT, was 259.5μm (95% CI, 239.0-279.7μm). The root mean square coefficient of variation (RMS CV) of the automatically determined average choroidal thickness of repeated SS-OCT scans with thick choroid was 3.4% (95% CI, 0.3%-4.7%) and had an intra-class correlation coefficient (ICC) of 0.93 ($p < 0.001$), The RMS CV between automatically determined average choroidal thickness of two SS-OCT scans and one SD-OCT scan with thick choroid was 16.4% (95% CI, 10.5%-20.7%) along with an

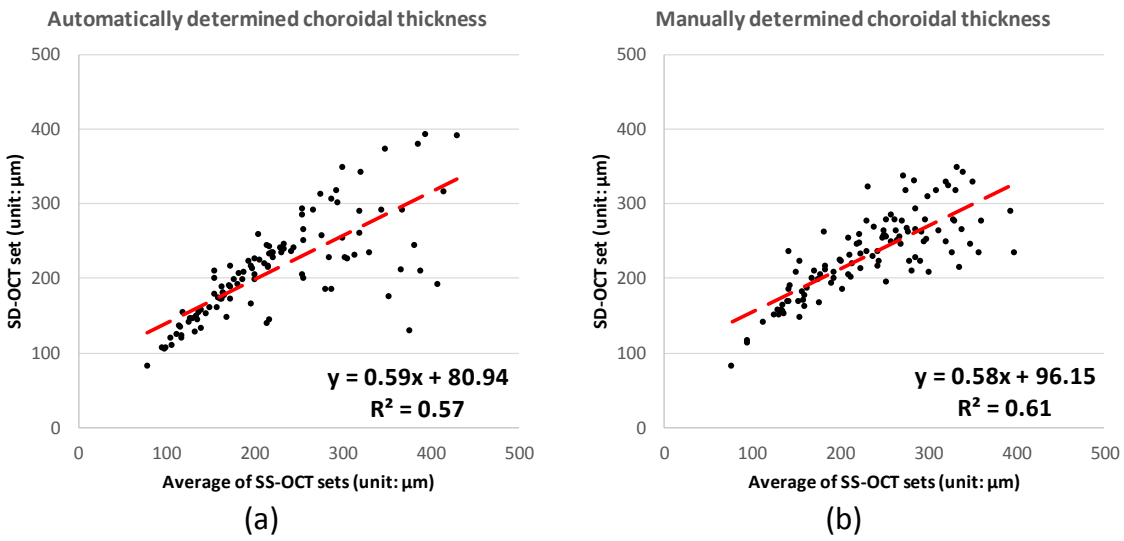

Figure 3.16: Correlation analysis of the choroidal thickness on entire 6-by-6 macular region between the mean of SS-OCT repeated scans and SD-OCT scan from the same subject: (a) automated segmentation; (b) manual segmentation.

ICC of 0.18 ($p = 0.1$). The difference in CV between thinner and thicker choroids was not significant ($p > 0.05$).

For the old choroidal vasculature based method, the mean ± standard deviation of the relative difference was -23.5±34.4μm (-9.0±13.2 voxels) and the mean ± standard deviation of absolute difference was 33.4±24.9μm (12.8±9.6 voxels) - for the entire dataset (216 SS-OCT images and 108 SD-OCT images). The proposed graph-based method in the current study outperformed the previous vasculature based method ($p < 0.001$).

Discussion

The results of this study show the validity of a fully automated three-dimensional method capable of segmenting the entire choroid and quantifying choroidal thickness of the macula in both SS-OCT and SD-OCT image of the same subjects, without a preceding vasculature segmentation step. Choroidal thickness can now be measured for each A-scan.

In the SS-OCT volumes, the volumetric data have sufficient image quality and high intensity contrast in the choroid region, so that our method successfully identifies the choroid borders in all SS-OCT scans accurately. In SD-OCT volumes, the intensity contrast is relatively lower, due to the increased backscattering of the retinal nerve fiber layer and retinal pigment epithelium layer, caused by the shorter 840nm wavelength used in these scanners. Swept-source OCT scanners use light with central wavelength of 1060nm, providing enough intensity contrast and choroidal border information. As shown in Figure 3.17, the choroidal posterior boundaries are less well visualized in these types of SD-OCT scans. Despite the relative insufficiency of the choroidal border information in SD-OCT images, the agreement between automated and manual segmentations was still good.

The results of layer thickness assessment show that the average choroidal thickness obtained from SS-OCT scans is 219.5μm (95% CI, 204.9-234.2μm) and average choroidal thickness obtained from SD-OCT scans is 209.5μm (95% CI, 197.9-221.0μm), corresponding to subfoveal choroidal thicknesses on SS-OCT of 246.7μm (max is 457.6μm; min is 83.2μm) and on SD-OCT of 229.7μm;(max is 429.0μm; min

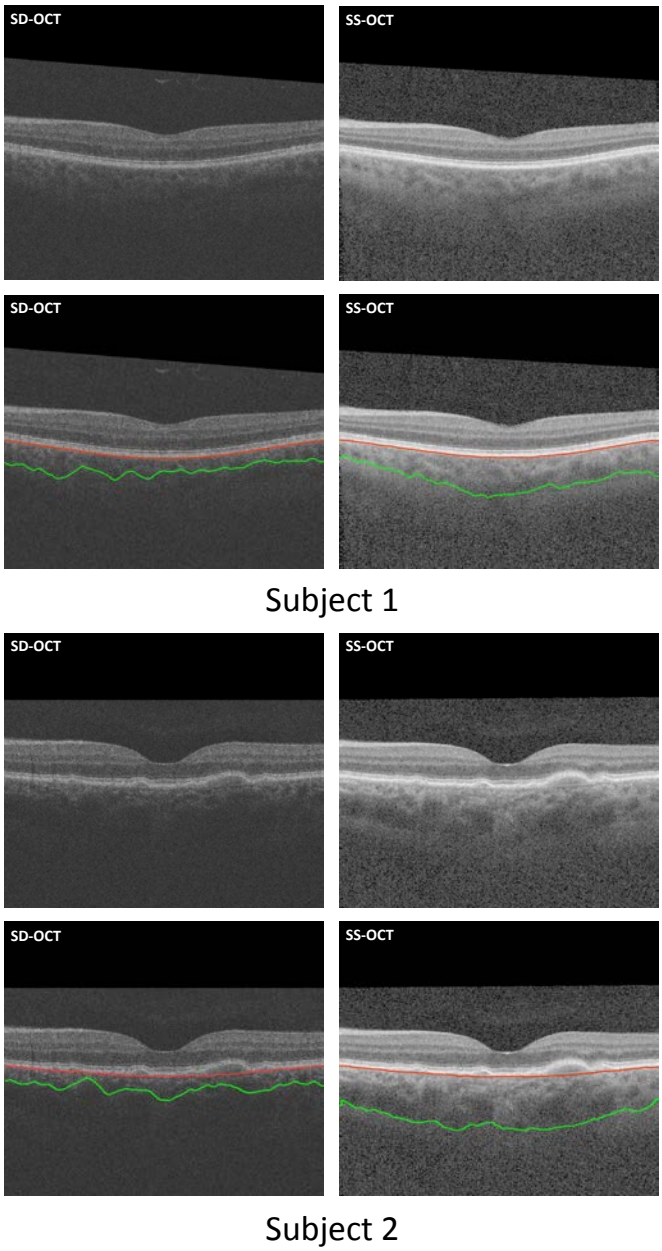

Figure 3.17: Two examples of subjects in which the proposed choroidal segmentation of SD-OCT scans (left column) resulted in a large underestimation, due to the lower contrast in that region, while segmentation of the SS-OCT scans of the same subjects (right column) led to adequate estimates.

is 85.8μm). These thicknesses are comparable to the choroidal thickness reported by other studies [80, 33, 94]. In reproducibility analysis of the choroidal thickness, the proposed method shows outstanding reproducibility in SS-OCT: RMS CV is 3.3% (95% CI, 2.2%-4.1%) along with an ICC of 0.98. Meanwhile, the proposed method shows good reproducibility between SS-OCT and SD-OCT: RMS CV is 11.0% (95% CI, 8.0%-13.3%) along with an ICC of 0.73 ($p < 0.001$). However, for a subset of thicker choroids, the proposed method performed significantly better ($p < 0.001$) on SS-OCT than on SD-OCT.

The present graph-based method also outperforms ($p < 0.001$) the earlier vasculature based method in reproducibility [28]. In the earlier vessel-based method, about 50% of the SD-OCT scans were successfully segmented; the other half of the SD-OCT scans were automatically detected as lacking choroidal vessel information [28]. Similar issues occur in the SD-OCT set of this new study. Inconsistency of the choroidal thickness is discovered in the correlation analysis between SS-OCT and SD-OCT. The correlation from automatically segmented choroid is shown by the R^2 of 0.57 with CV of 10.9% and that from manually segmented choroid is shown by the R^2 of 0.61 with CV of 9.1% (no significantly difference between choroidal thicknesses from manually and automatically segmentations, $p = 0.24$), see Figure 3.16. In the correlation analysis between automatically determined choroidal thicknesses of SS-OCT and SD-OCT images, some segmentations show a relative large distance to the identity line, as shown in the region outlined with red solid segments in the Figure 3.18. Spectral domain-OCT underestimates thickness relative to Swept Source-OCT

with low contrast. If we remove these problematic scans from analysis (20 out of 108 SD-OCT scans), the remaining scans show a reasonably good CV and ICC: for automatically segmented choroid, CV is 5.4% and ICC is 0.96 ($p < 0.001$); for manually segmented choroid, CV is 8.1% and ICC is 0.83 ($p < 0.001$). Thus, we may conclude that these 20 out of 108 SD-OCT scans do not have enough intensity contrast around the choroidal-scleral interface for automated or manual segmentations.

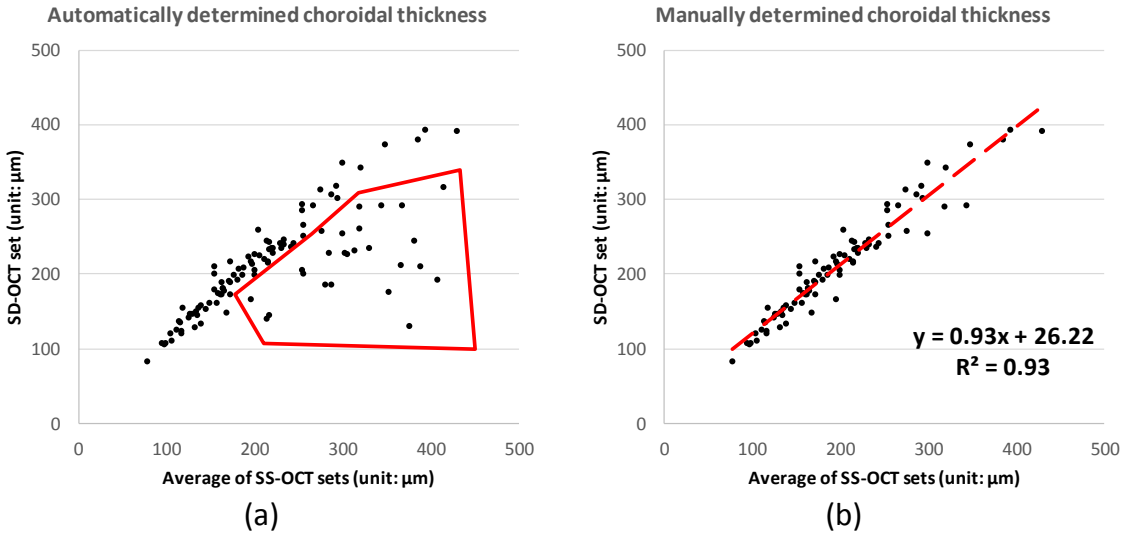

Figure 3.18: (a) The correlation between the choroidal thicknesses from SS-OCT and SD-OCT is fair as shown in Figure 3.16 (R^2<0.65). The region outlined by the red segments represents where some SD-OCT images do not have enough intensity contrast around choroidal-scleral interface; (b) The correlation was largely improved if we only consider those images with sufficient image quality.

In summary, the present method shows outstanding performance for segmenting choroid in all SS-OCT scans and good performance for segmenting choroid in more than 80% of SD-OCT scans (88 out of 108 scans). For the other 20 out of 108 SD-OCT scans, although the automated method agrees highly with manual method, but the real accuracy of the segmentation results may be problematic. In this sense, SS-OCT imaging at 1060nm is better for automated (and manual analysis) than SD-OCT imaging with at 840nm.

Recently, other groups have reported evaluations of semi-automated or automated segmentation of the choroid. These studies used surface fitting, surface smoothing or post-processing steps for identifying the choroidal borders. However, such approaches can only produce an approximate segmentation of choroid and deliver approximations of the overall average choroidal thickness. To the best of our knowledge, the method we report here is the first fully 3D automated method capable of accurately identifying the local thickness of the choroid for each A-scan. Figure 3.19 shows choroidal thickness maps and difference maps for one subject, demonstrating high reproducibility of choroidal thickness across OCT analyses of the same subjects.

There are several limitations to this study. First, due to the large data set, only two B-scans – the central B-scan and a random B-scan were selected from each volumetric image for manually identifying the choroidal posterior boundaries. As shown in the method details, the proposed graph-based method treats every B-scan evenly and the location of the random B-scans should represent all non-foveal re-

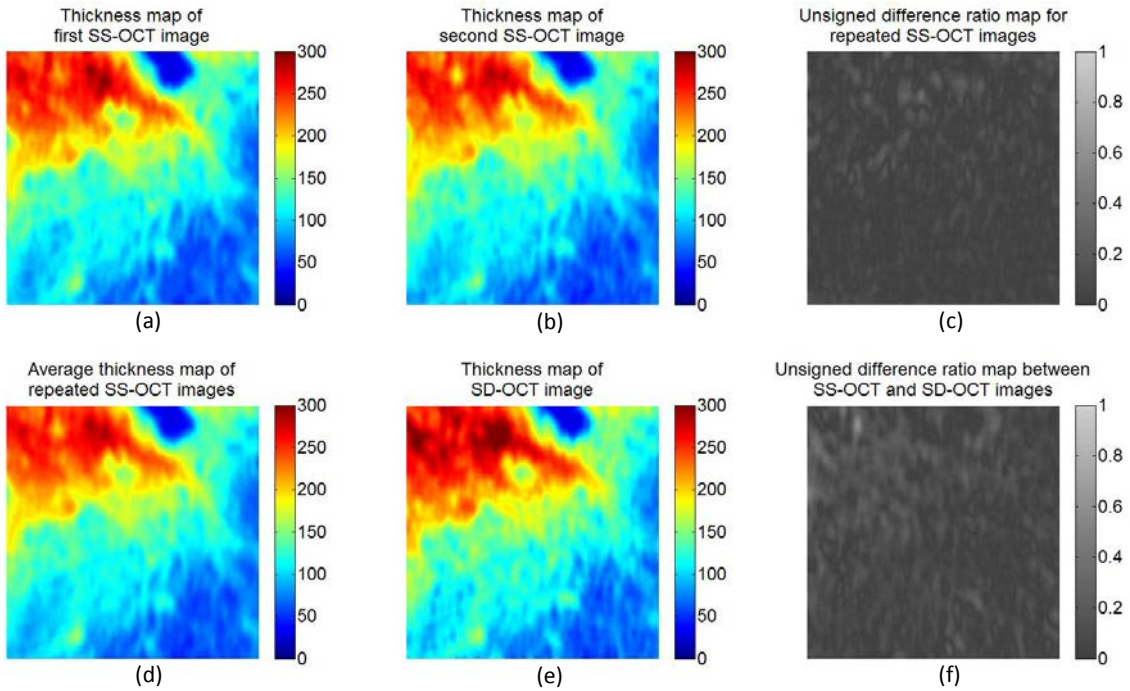

Figure 3.19: Choroidal thickness maps and relative difference ratio maps from the same subject. (a) Thickness map of the first SS-OCT image; (b) Thickness map of the second SS-OCT image; (c) Absolute difference ratio map for the repeated SS-OCT images; (d) Average thickness map of the repeated SS-OCT images; (e) Thickness map of SD-OCT image; (f) Absolute difference ratio map between the average SS-OCT image and SD-OCT image. The absolute difference ratio is computed as the result of the absolute difference along each A-scan divide by the average thickness between the thicknesses. The absolute difference ratio map between SS-OCT and SD-OCT images shows relatively larger difference than the absolute difference ratio map for repeated SS-OCT images.

gions around macula across the entire dataset. Furthermore, the tests of RMS CV, ICC were performed on the entire 6-by-6 mm^2 macula-centered region. In a future study, we plan to evaluate the all B-scans if the manual segmentation is available for the entire macula-centered region. Second, the selected subjects were relatively old adults and did not have diseases such as Central Serous Retinopathy (known to result in a thickened choroid). The presented method should also be evaluated in younger persons and persons with choroidal abnormalities. Such studies are currently being pursued. Third, all scans were scanned in horizontal (temporal-nasal) B-line mode. Each volumetric image had dimensions of 512 voxels temporal-nasally and 128 voxels on superior-inferiorly. This required us to use anisotropic smoothness constraints as more relaxed constraints on superior-inferior direction and less relaxed constraints on temporal-nasal direction. Fourth, systematic differences were discovered between manual measurements and automated or semi-automated measurement when segmenting the choroidal posterior boundary [87].

In summary, we have developed a fully automated three-dimensional method for segmenting choroid layer and quantifying choroidal thickness in SS-OCT and SD-OCT volumetric data. The method yielded highly accurate segmentation results in SS-OCT and relatively good segmentation results in SD-OCT compared to a human expert. This is the first fully three-dimensional automated method capable of accurately identifying the local thickness of the choroid in each A-scan. Potentially, our method may enhance the understanding of regional choroid changes and improve the diagnosis and management of patients with diseases in which the choroid is affected.

CHAPTER 4
AUTOMATED SEGMENTATION OF OUTER RETINAL STRUCTURES

In this Chapter, we will discuss the developed methods for segmenting sub-retinal tissues (Aim 2). In Section 4.1, we consider the space from photoreceptor layer to Bruch's membrane as one combined layer, named outer-retinal sub-retinal (ORSR) layer. Thickness changes of ORSR layer implies the growth of abnormal regions in this space. Thus, we design new costs and constraints to improve the previously reported multi-layer segmentation [95] for segmenting ORSR layer. This work was published in *Investigative Ophthalmology and Visual Science, 2014*. In Section 4.2, we focus on the measurement of drusen — the abnormal deposits between RPE layer and Bruch's membrane. A multi-surface graph-search approach is introduced to segment the drusen-related surfaces. Due to the varied shape and appearance, distinct settings are applied on different surfaces. We then use the segmented surfaces to identify the outline of drusen.

4.1 Quantifying Disrupted Outer Retinal-Subretinal Layer in SD-OCT Images in Choroidal Neovascularization

Abstract

Purpose: To report a fully automated method to identify and quantify the thickness of the outer retinal-subretinal (ORSR) layer from clinical spectral-domain optical coherence tomography (SD-OCT) scans of choroidal neovascularization (CNV)

due to exudative age-related macular degeneration (e-AMD).

Methods: 23 Subjects with CNV met eligibility. Volumetric SD-OCT scans of 23 eyes were obtained (Zeiss Cirrus, 200×200×1024 voxels). In a subset of eyes, scans were repeated. OCT volumes were analyzed using our standard parameters and using a 3D graph-search approach with an adaptive cost function. A retinal specialist graded the segmentation as generally accurate, local segmentation inaccuracies, or failure. Reproducibility on repeat scans was analyzed using root mean square coefficient of variation (RMS CV) of the average ORSR thickness.

Results: Using a standard segmentation approach, 1/23 was graded generally accurate, and 22/23 OCT segmentations were failure(s). With the adaptive method 21/23 segmentations were graded generally accurate; 2/23 were local segmentation inaccuracies and none was failure. The inter-method quality of segmentation was significant difference ($p << 0.001$). The average ORSR thickness measured on CNV patients ($78.0\mu m$, 95% Confidence Interval: $72.5\mu m$ $83.4\mu m$) is significantly larger ($p << 0.001$) than normal average ORSR layer thickness ($51.5\mu m \pm 3.3\mu m$). RMS CV was 8.1%.

Conclusion: We have developed a fully automated 3D method for segmenting the ORSR layer in SD-OCT of patients with CNV from eAMD. Our method can quantify the ORSR layer thickness in the presence of fluid, which has the potential to augment management accuracy and efficiency of anti-VEGF treatment.

Introduction

Approximately 10% of patients with age related macular degeneration (AMD) have the exudative form of this disease [96]. Exudative AMD (eAMD) typically includes overt evidence of choroidal neovascularization (CNV), manifesting as retinal pigment epithelial detachment, subretinal and intraretinal cysts and fluid, retinal pigment epithelial tears, fibrovascular disciform scarring and vitreous hemorrhage [97]. Recently, anti-vascular endothelial growth factor (anti-VEGF) agents have become the mainstay of treatment for CNV [13] in eAMD. In addition to visual acuity as a functional measurement, retinal thickening, location, and amount of intra- and subretinal fluid as imaged by optical coherence tomography (OCT) have become the principal milestones in the management of CNV with anti-VEGF agents [98] .Therefore, accurately and automatically segmenting the retinal structures in CNV is of great interest. Such a method has the potential to increase management accuracy and efficiency. However, CNV-associated retinal layer distortion that results from intra- and sub-retinal fluid accumulation makes accurate segmentation more challenging than in normal subjects or patients with, atrophic diseases such as glaucoma [7]. Fluid-associated abnormalities (Figure 4.1) have been segmented using manual or semi-manual approaches [99, 100] but these methods are time-consuming and suffer from intra- and inter-observer variability. Previously, our group has developed the Iowa Reference Algorithms, an environment for fully automated 3D segmentation of retinal layer structures [51] and also reported methods for detecting fluid-filled abnormalities in 2D OCT projection images and in 3D volumes [39, 42]. To enhance

the robustness when segmenting intra-retinal surfaces in normal subjects, these algorithms employ a strong distance constraint between myoid inner segment - ellipsoid inner segment (myoid IS - ellipsoid IS) and Bruch's membrane (BM). The increased thickness of the subretinal layers typical for CNV violates such distance constraints and may lead to segmentation errors. The present approach solves this problem by employing an adaptive cost function that is modulated based on the detection and OCT image properties describing the local structural abnormalities and augments the distance constraints. We report a fully automated 3D method for segmenting the outer retinal-subretinal (ORSR) layer in SD-OCT of patients with CNV and quantifying the ORSR layer thickness in the disrupted outer retina.

Methods

Subject and Data Collection

Twenty-three (23) patients, with an average age of 80.4 (95%CI: 77.7-83.0) years; 39.1% (9 out of 23) male, with clinically significant CNV underwent SD-OCT imaging (Zeiss Cirrus; Carl Zeiss Meditec, Inc., Dublin, CA). Twenty-three (23) independent macula-centered volumetric scans were obtained from 23 eyes of these patients at the University of Iowa. Each volume was 200×200×1024 voxels (width of B-scan × number of B-scans × depth of B-scan), corresponding to physical dimensions of 6.0×6.0×2.0 mm^3, and voxel size was 30.0×30.0×2.0μm^3. In 11 eyes from 11 subjects, repeat scans were obtained. Written informed consent was obtained from all subjects. The collection and analysis of image data were approved by Institutional

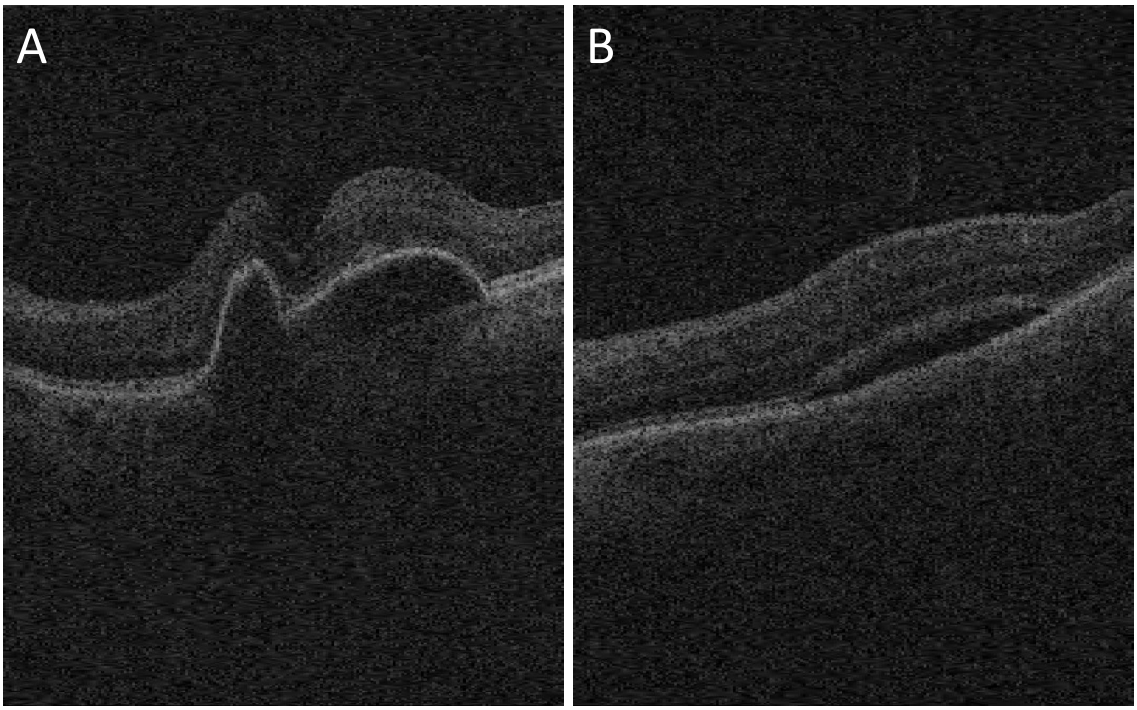

Figure 4.1: Exudative AMD in spectral domain optical coherence tomography: A) Pigment epithelial detachment; B) Subretinal fluid.

Review Board of the University of Iowa and adhered to the tenets of the Declaration of Helsinki.

Initial Segmentation

To reduce effects of and artifacts associated with retinal OCT imaging and achieve successful retinal segmentation, the developed image analysis approach consists of four subsequent stages. First, an initial segmentation is employed to detect ORSR layer using our previously reported 3D graph-based multilayer segmentation approach [69] (Figure 4.2.B). The initial segmentation provides approximate depth

of the ORSR layer in the SD-OCT image. As expected, due to the shape complexity and random distribution of subretinal fluids and pigment epithelial detachments, segmentation errors are present at this stage (see Figure 4.2.D).

Fluid-Associated Abnormalities Detection

As discussed above, the varying shapes of ORSR layer resulting from the abnormalities increase the likelihood of incorrect segmentation. Stages 2 and 3 are used to locate the abnormal regions. By comparing textural properties of initially-segmented layers in AMD scans with an average texture of those layers in normal scans, a two-dimensional "footprint" is computed in stage 2, identifying the locations of abnormal regions in the X-Y plane (see Figure 4.3) [39]. To reduce the processing time, the "footprint" results was down-sampled by the rate of 10 on each of the directions. The "footprint" In stage three, we apply a supervised voxel classification method to detect fluid-filled abnormalities in 3D. The inputs of this classification method, including structural, positional and textural features, are derived from the original 3D volume data, 2D footprint images, and the initial segmentation. The structural and textural features describe the local and regional image information while positional features describe the distance of individual layers from the initial segmentation. A k-nearest neighbor (kNN) classifier was chosen to classify OCT image voxels and evaluate in a leave-one-out fashion. A three-dimensional probability map was calculated by determining the probability whether a voxel was located inside a fluid-filled region (see Figures 4.4.A and 4.4.B) [42].

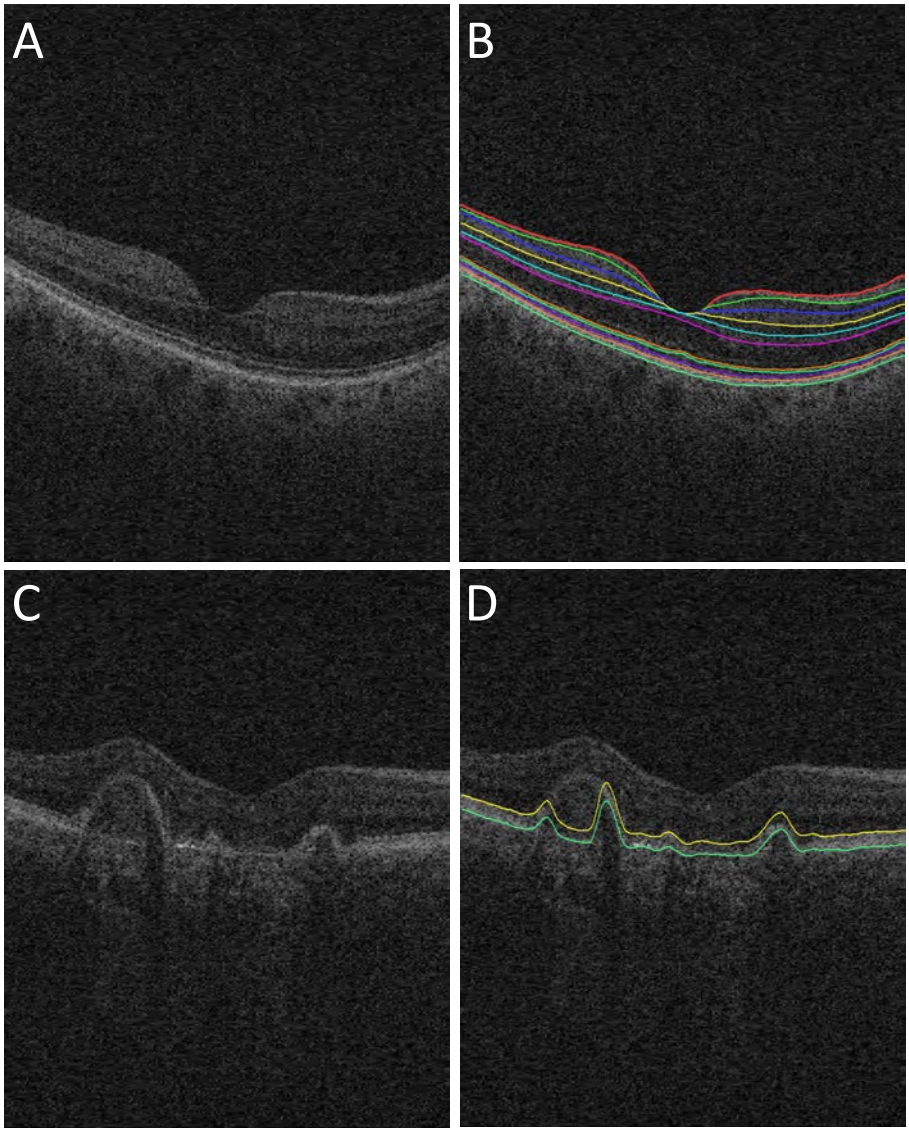

Figure 4.2: Retinal surfaces segmentation: A) Original B-scan of 3D SD-OCT image from a normal subject; B) Eleven retinal surfaces segmentation for the normal subject; C) Original B-scan of SD-OCT image from an exudative AMD patient; D) Initial segmentation of ORSR surfaces of the exudative AMD patient, showing incorrect segmentation.

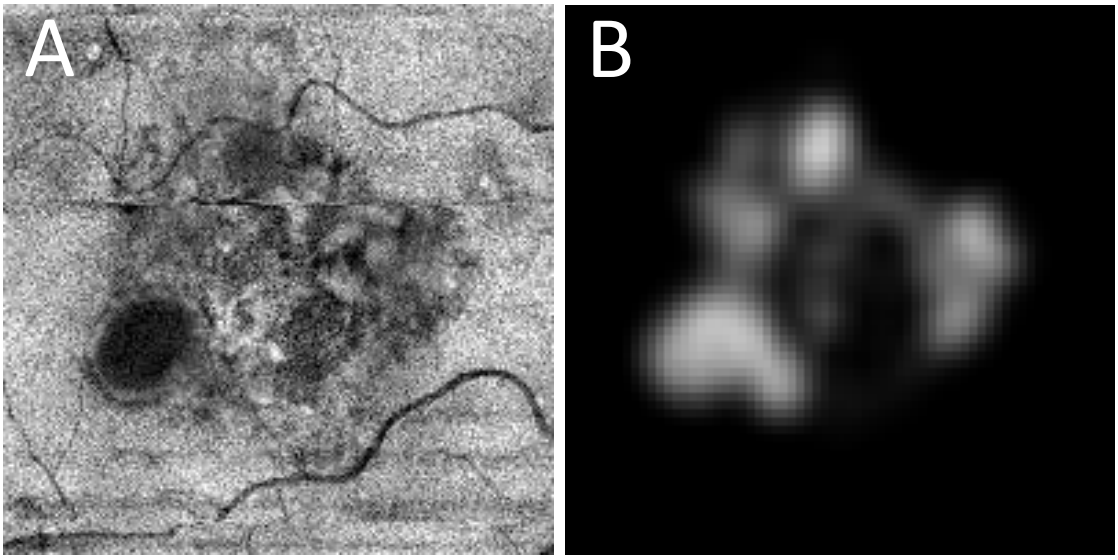

Figure 4.3: A) Outer retinal-subretinal projection image; B) "Footprint" image of the fluid-filled abnormalities detected in the subretinal space.

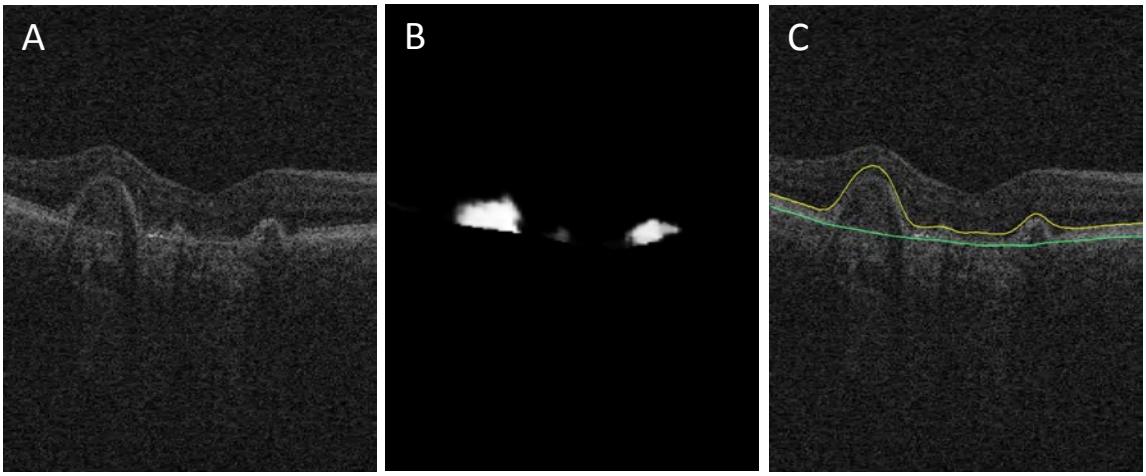

Figure 4.4: A) Original B-scan; B) Detection result of fluid-filled regions the output of 3D voxel classification; C) Surfaces segmentation result of ORSR layer: Bruch's membrane (green surface) and the surface that corresponds to the transition between the myoid and ellipsoid inner segment (myoid IS - ellipsoid IS, yellow surface).

Outer retinal-Subretinal Layer Segmentation

In stage four, intensity gradient images are used to form the initial cost functions for a graph-search method to identify a full set of ORSR using a multi-scale graph-search method [95, 101]. As shown in Figure 4.4.C, the bright line corresponding to Bruch's membrane (green line) was defined as the outer boundary of ORSR. The surface that corresponds to the transition between the myoid and ellipsoid inner segment (yellow line) was defined as the inner boundary of our outer retina segmentation [102]. For every node in the graph, the corresponding likelihood value on the 3D probability map was used as a weighting value to modify the initial gradient-based cost function. Distance constraints were modified in response to the 3D probability map. For each A-scan, a higher probability value contributed to utilizing a larger distance constraint. Subsequently, the surfaces (myoid IS - ellipsoid IS and BM) are hierarchically segmented by identifying the minimum s-t cut in the employed geometric graphs, in which the weighted cost functions of vertical gradient transitions were utilized. Method details were described in Chapter 5 Section 5.2.

Validation of the Outer retinal-Subretinal Layer Segmentation

After ORSR layer segmentation, the local ORSR thickness defined as the Euclidian distance between myoid IS ellipsoid IS and BM was calculated along each A-scan, which is the summation of RPE thickness, outer segment length (OSL) ellipsoid inner segments [103], and the height of any fluid-filled abnormalities. Outer retinal-subretinal layer thickness map for the $6\times6mm^2$ macula-centered region as im-

aged by the SD-OCT was then created for all subjects (see Figure 4.5.B). A retinal specialist who was blinded to the employed algorithm evaluated the segmentation performance of the original and new methods using a manual segmentation/review tool. Twenty three surface segmentation results of the present method and 23 results of the original method were mixed together in a random order. One original B-scan and the same B-scan with segmented surfaces depicted as layer boundaries were always displayed simultaneously to provide original unprocessed image to the expert observer. For each SD-OCT image data, the expert graded the segmentation result based on its correctness using three performance levels: a) generally accurate, b) local segmentation inaccuracies, and c) failure. The grading results of the two methods were compared using Fisher's exact test. A p value of 0.05 was considered significant.

Reproducibility assessment

To evaluate the reproducibility of the proposed computerized method in the 11 repeat images (see Figure 4.6), coefficients of variation (CV) of the average ORSR thickness were calculated from two independent automated analyses using the root mean square (RMS) approach and the coefficient of variation across the repeat analyses was computed.

Layer thickness assessment

Once the performance of the new method was established by the above validation experiment, the average thicknesses of the ORSR layers were computed from the results of the new image segmentation analysis in all 23 datasets no datasets were

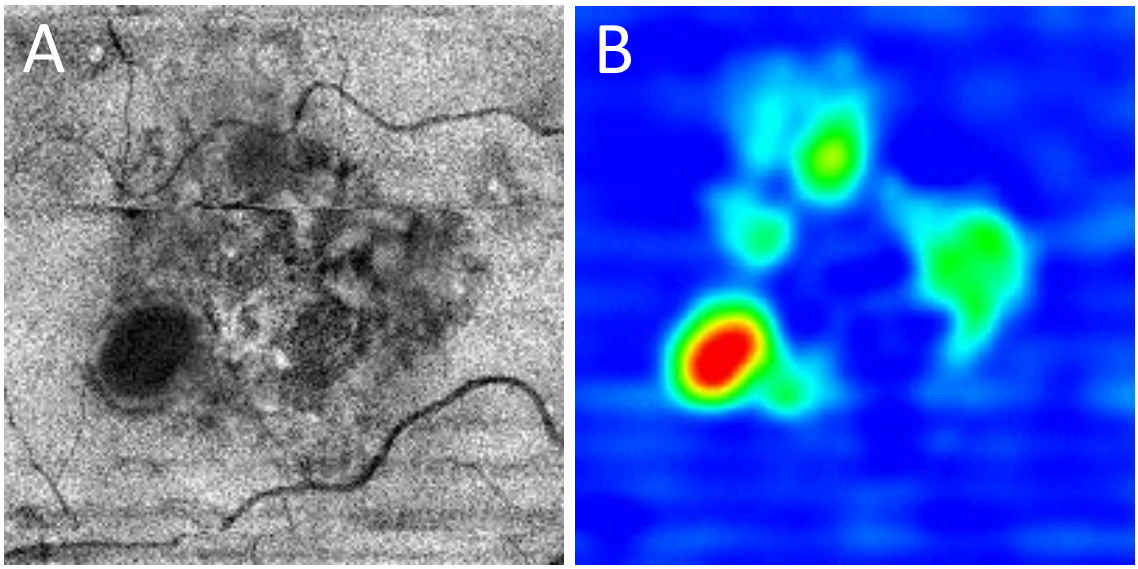

Figure 4.5: Outer retinal-subretinal layer thickness maps: A) ORSR projection image from the SD-OCT volume data; (B) An example thickness map of the proposed ORSR layer segmentation method, the average thickness on the analyzed 23 patients with CNV was 71.40μm (max: 336.27μm, min: 29.33μm).

excluded from the analysis and no segmentations were manually edited. The average thickness was reported in μm, 95% confidence intervals were determined, and the obtained ORSR layer thickness compared with OCT specimens-established ORSR layer thickness in normal subjects [104, 105]. The layer thicknesses of the two groups were statistically compared using t-test with a p value of 0.05 considered significant.

Results

With the original approach 1/23 was "generally accurate" none were graded "local segmentation inaccuracies" and the remaining 22/23 OCT datasets were graded

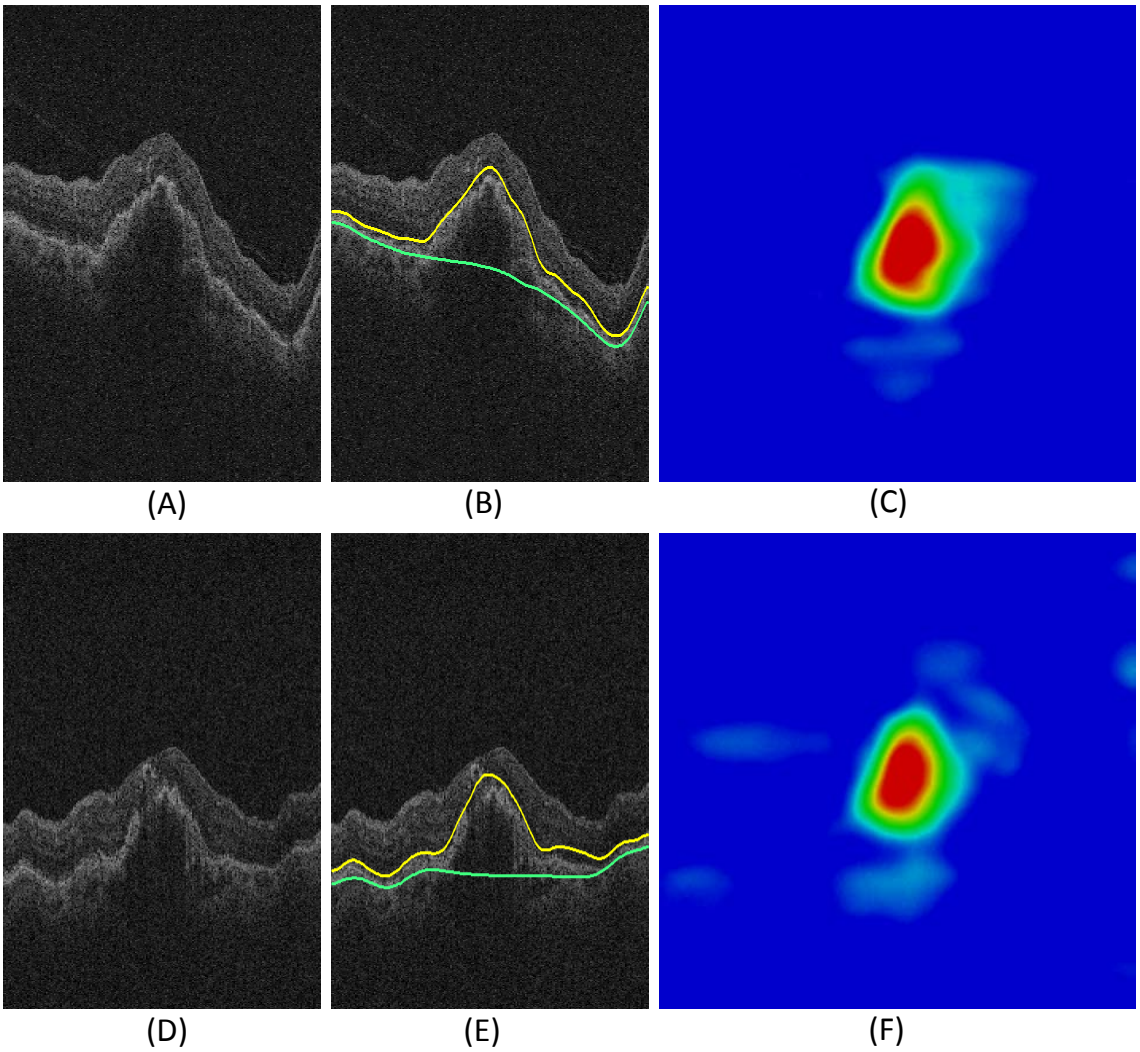

Figure 4.6: Reproducibility of ORSR layer segmentation. (A-C) First visit image data of an example subject: (A) Original slice; (B) ORSR segmentation; (C) Thickness map of the first visit image data. (D-F) Second visit image data of the same example subject: (D) Original slice; (E) ORSR segmentation; (F) Thickness map of the second visit image data.

as "failure" (see Figures 4.7.C). With the new approach, 21/ 23 segmentations were expert-graded as "generally accurate" (see Figures 4.7.A); the remaining 2/23 were graded as "local segmentation inaccuracies" (see Figure 4.7.B), and none was considered a "failure". This is a significant improvement (Fisher's exact test, $p << 0.001$) (Figure 4.8).

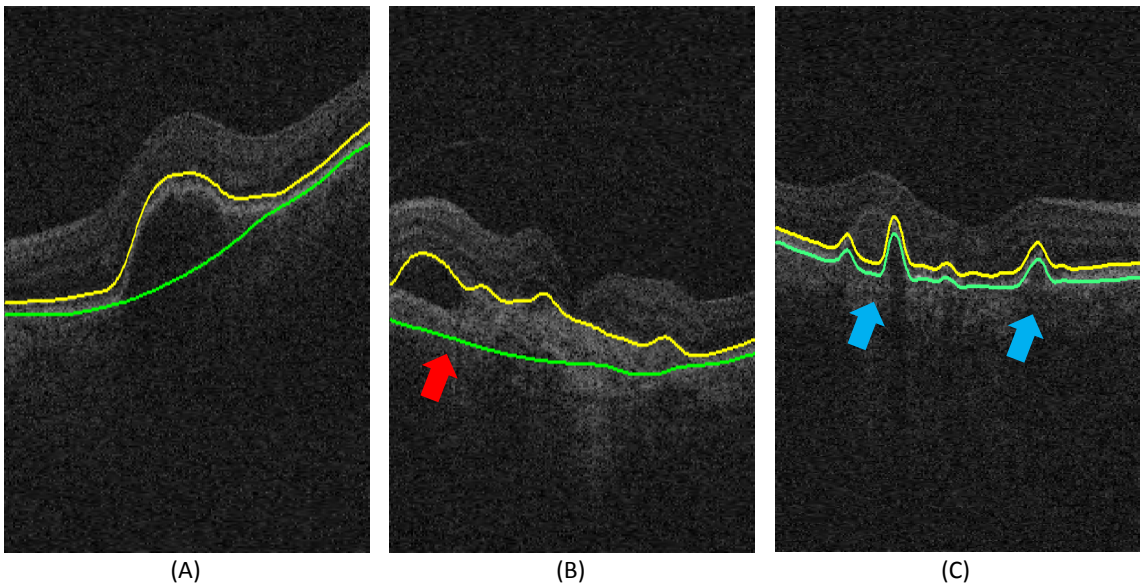

Figure 4.7: Examples of performance grading: (A) "Generally accurate" segmentation, (B) Segmentation that "includes local segmentation inaccuracies" - marked by a red arrow; (C) "Failure", in proximity to the choroidal region, marked by blue arrows.

The reproducibility analysis tested the average ORSR thickness of repeat scans from the same patient and showed that the segmentation results of the present method are highly reproducible. As shown in the Figure 4.9, RMS CV for ORSR was 8.1%.

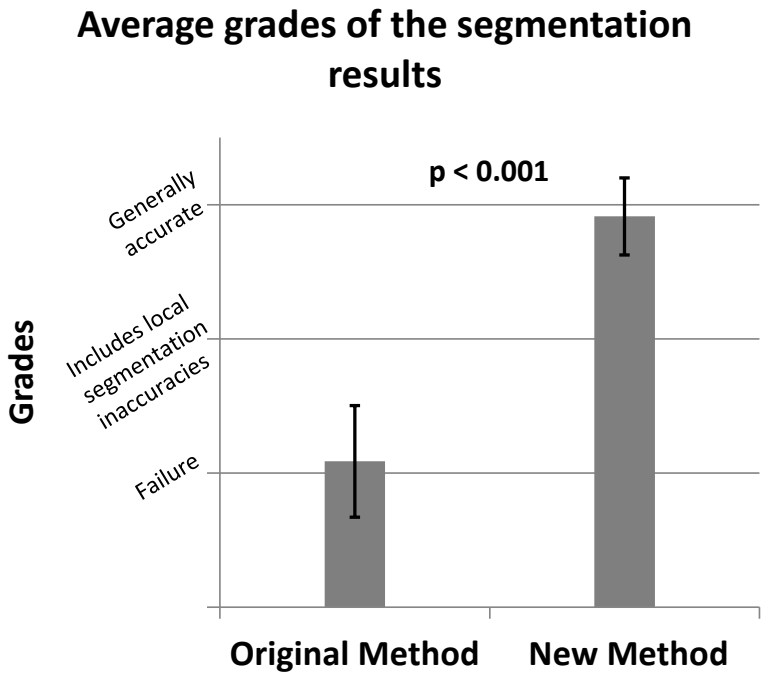

Figure 4.8: Performance comparison of the original and our new ORSR layer segmentation approaches based on expert evaluation.

Average ORSR thickness of the exudative AMD subjects in this study was 78.0μm (95% CI 72.5μm 83.4μm) for the 6×6mm^2 macula-centered region. Comparison with the finding on normal outer retinas in OCT specimens showed that average thickness (± standard deviation) of the normal ORSR layer was 51.5μm (± 3.3μm) [106]. Not surprisingly, the ORSR thickness measured on CNV patients is significantly larger ($p << 0.001$) than the normal average ORSR layer thickness.

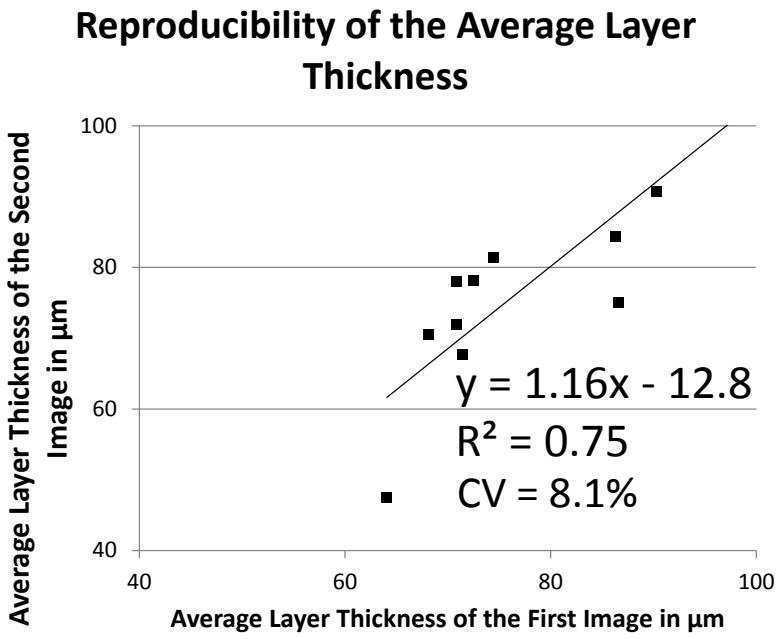

Figure 4.9: Reproducibility of automatically determined average ORSR layer thickness (n=11).

Discussion

The results show that our new fully automated 3D method for segmenting the ORSR layer in SD-OCT of patients with CNV is able to successfully segment and subsequently quantify the ORSR layer thickness in the disrupted outer retina. Our new method successfully identified the ORSR layer affected with fluid-filled abnormalities in more than 90% (21 out of 23) of cases in this data set. The segmentation inaccuracies that occurred in 2 out of 23 datasets showed local inaccuracies that did not prevent the segmentation results from being used for quantitative analysis of the ORSR layer. The observed segmentation inaccuracies typically resulted from large

solid tissue accumulation in the outer retina. In the OCT images, these solid tissues reduced the contrast around the ORSR, thus preventing the segmentation result to exactly locate the proper layer surface in the subretinal space. Simultaneously, the segmented surface of Bruch's membrane may in these regions be attracted by a higher contrast appearance of choroidal vessels as shown in Figure 4.7.B. This dual effect may be the key reason for the observed local segmentation inaccuracies in the 2 identified datasets.

In our previously reported standard layer segmentation, fixed and strong constraints limited the distance between myoid IS ellipsoid IS and BM, resulting in segmentation failure as shown in the expert evaluation. The reproducibility test showed the root mean square CV of the standard layer segmentation is 4.3%, which means similar segmentation failure may occur in the repeat scans of the patient. Compared to the standard layer segmentation with fixed and strong distance constraints, our new segmentation approach offers markedly better performance and improved the outcome in over 95% (22 out of 23) cases. Reproducibility of the new method is also high as shown by a root mean square CV of 8.1%.

Due to the relatively low signal strength in standard clinically available SD-OCT data and random distribution of the fluid-filled abnormalities, automated segmentation of ORSR layer is challenging and surface detection results may become locally inaccurate within the subretinal space. However, as our study shows, these inaccuracies do not prevent the segmentation results to be used for quantitative analysis without manual editing.

To the best of our knowledge, this is the first 3D automated method capable of successfully segmenting the ORSR layer with a disrupted outer retina in exudative AMD scans. An example of 3D visualization of our new method's segmentation is provided in Figure 4.10. Accurate segmentation of the ORSR is essential for better automated quantification of subretinal and sub-RPE deposits such as drusen, which are associated with the progression of AMD.

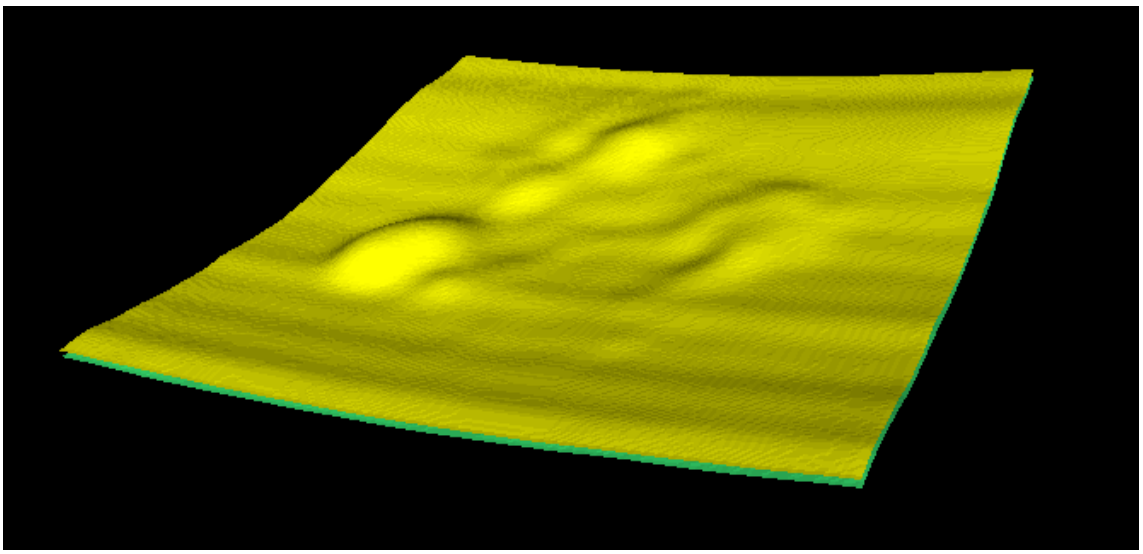

Figure 4.10: 3D visualization of the ORSR layer obtained using the new segmentation approach in an OCT image of a CNV patient.

This study is not free of several limitations. First of all, the number of subjects was relatively small. Technically, the expert evaluation result showed the present method has improved the segmentation of outer retina affected by subretinal fluid and

pigment epithelial detachment. However, the restricted size of the data set prevented us from learning clinically more important information, even though the proposed method provided more accurate segmentation results. We are currently pursuing a study with a larger population.

Second, we used clinically standard SD-OCT scanners with a center wavelength of 840nm. The existence of fluid-filled regions may resist the penetration of light, thus causing lower contrast around Bruch's membrane. Although the reproducibility analysis showed our proposed method performed robustly, enhanced depth imaging (EDI) and a longer center wavelength may further improve the accuracy of the layer segmentation.

In summary, we have developed a fully automated 3D method for segmenting the ORSR layer in SD-OCT of patients with exudative AMD and quantifying the ORSR layer thickness in the occurrence of subretinal fluids and pigment epithelial detachments. The method outperformed our original layer segmentation and yielded robust segmentation outcomes as evaluated in the reproducibility studies. Our method has a potential to improve the diagnosis and management of patients with AMD and CNV.

4.2 Automated Segmentation of Drusen in Non-neovascular Age-related Macular Degeneration using SD-OCT Images

Abstract

Purpose: To develop a fully automated three-dimensional method for segmentation of drusen in non-neovascular age-related macular degeneration (AMD), quantification of drusen load in macula region, and evaluate repeat variability of manual grading and automated segmentation using spectral-domain OCT.

Methods: Patients (209) with non-neovascular AMD were imaged using three-dimensional spectral-domain optical coherence tomography (Topcon Corp., Tokyo, Japan). A 3D method was used to segment the drusen and quantify the drusen load. The severity of drusen was automatically determined from drusen segmentation. To evaluate the drusen segmentation, manually graded severity of drusen on color fundus photographs was introduced and compared with the automatically determined severity of drusen. Test retest repeatability and reproducibility were analyzed using manually and automatically determined results.

Results: 627 grading values were assessed between automated and manual grading using confusion matrix. 43.5% of the automated grading values (273) exactly matched with manual results, 41.6% of the automated grading values (261) were off-diagonal with distance of one to the identical line (red diagonal cells). The Cohen's kappa value is 0.551 corresponding to a "moderate" agreement. The reproducibility analysis showed the segmentations on repeated scans were highly reproducible as the dice coefficient of 0.803.

Conclusion: We have developed a fully automated 3D method for segmenting the drusen in SD-OCT. Our method can assess the severity of drusen load and quantify the drusen volume, which has the potential to improve the diagnosis and management of non-neovascular AMD.

Introduction

Age-related macular degeneration (AMD) is the leading cause of severe visual loss and blindness in patients over the age of 50 [8]. One of its early clinical finding is the presence of drusen [8]. Drusen are focal deposits of extracellular material that accumulate between the lower boundary of RPE and Bruch's membrane [107]. Drusen are associated with aging; the presence of a few small solid drusen (called "hard drusen") is normal in adults. However, several studies show that the progression of AMD has a positive correlation with drusen load in macular region [108, 109].

Color fundus photographs (CFPs) are used clinically to evaluate the drusen load. Drusen are shown as yellow or white abnormal regions in color fundus photographs. However, reliably delineating the drusen outline is challenging. Due to the lack of depth information, the margins of drusen is difficult to be identified and drusen measurement could be affected by the abnormal foldings on retinal pigment epithelium (RPE) layer or retinal nerve fiber layer (RNFL), where show the bright intensity as well. Many research groups have reported manual and automated segmentation of drusen for CFPs [110, 111, 112, 113, 114, 46]. However, true volume of drusen cannot be assessed using this two-dimensional imaging modality.

Optical coherence tomography (OCT) provides in vivo non-invasive cross-sectional imaging of retinal structure [115, 116, 117]. Recently, our group has developed the Iowa Reference Algorithms, a set of fully automated 3D segmentation algorithms for the analysis of retinal layer structures [7]. With high image resolution and sufficient image quality, spectral domain OCT (SD-OCT) provides a promising alternative modality for imaging the drusen. The complete segmentation of drusen is thus becoming feasible. To achieve drusen measurement in OCT images, many studies use manual or semi-manual approaches for segmenting drusen and quantifying druson load [118, 119, 120, 121, 122]. Recently, a few groups have presented automated segmentation of drusen in 2D OCT B-scan [123].

The purpose of this paper was to develop and evaluate the validity of a novel fully automated three-dimensional method capable of segmenting the drusen and quantifying the drusen load including drusen volume and drusen area in SD-OCT image data.

Methods

Subject and Data Collection

The Rotterdam study is a prospective population-based cohort study, which investigates chronic diseases in the middle-aged and elderly [88]. Inhabitants of Ommoord, a suburb of Rotterdam, the Netherlands, were invited to participate in this study at three different times: 1989, 2000 and 2006. This resulted in three cohorts: Rotterdam Study I (N=7,983 aged 55 years and older), Rotterdam Study II (N=3,011

aged 55 years and older) and Rotterdam Study III (N=3,982, aged 45 years and older). Follow-up examinations took place every 2-4 years and are still ongoing.

For this study we included two hundred and nine (209) subjects from the Rotterdam study, who were identified as contracting dry-AMD. All subjects, with an average age of 74.1 $\pm$ 9.2 years; 38.8% (81 out of 209) male, underwent spectral domain-OCT imaging (SD-OCT, Topcon Corp., Tokyo, Japan). Two hundred and nine (209) independent macula-centered volumetric scans were obtained and enhanced Depth Imaging (EDI) mode was not used [83]. Each volume scan was 512(width of B-scan)$\times$128(number of B-scans)$\times$885(height of B-scan) voxels, corresponding to physical dimensions of approximately 6.0$\times$6.0$\times$2.3mm^3, the voxel size was 11.72$\times$46.88$\times$2.60μm^3. Forty-two repeat scans with qualified image quality were obtained for reproducibility analysis. Volumetric scan data were de-identified before image analysis. The Rotterdam Study has been approved by the Medical Ethics Committee of the Erasmus MC and by the Ministry of Health, Welfare and Sport of the Netherlands, implementing the "Wet Bevolkingsonderzoek: ERGO (Population Studies Act: Rotterdam Study)". All participants provided written informed consent to participate in the study and to obtain information from their treating physicians. De-identified volume scans were transferred to the University of Iowa XNAT image database for offline processing [89]. The study adhered to the tenets of the Declaration of Helsinki.

Drusen Segmentation

We have developed a three-stage approach for segmenting drusen. First, since the retinal angle between the incident light and subject's optical axis varied in OCT volumetric images, the geometric distortion occurred in retinal pigment epithelium (RPE) layer. An angle adjustment approach was thus applied to the original OCT volume (see Figure 4.11). Bruch's membrane was then transformed to a relatively symmetrical surface in the OCT image. Second, a multi-surface graph-search method was utilized to segment the outer retinal layers (see Figure 4.12). From top to bottom, these surfaces are upper boundary of RPE (uRPE), lower boundary of RPE (lRPE) and Bruch's membrane (BM). Multiple intensity transitions were expected to be present around the RPE complex region and vertical intensity gradient images were thus introduced to construct the cost function in the graph-based method. To represent the shape and continuity of the segmented surfaces, smoothness constraints were adopted between neighboring A-scans in different settings. During the progression of drusen, two boundaries of RPE layer (uRPE and lRPE) became corrugated, larger smoothness constraint was thus set to allow geometric changes in the corresponding segmented surfaces. To ensure the relative stiffness of Bruch's membrane, smaller smoothness constraint was then applied to the segmented BM. Furthermore, due to the unequal voxel dimensions in the Topcon OCT images (512 voxels in temporal-nasal direction and 128 voxels in superior-inferior direction), anisotropic constraints were established; more relaxed constraint in superior-inferior direction and less relaxed constraint in temporal-nasal direction. The three surfaces were subsequently

segmented by graph optimization via computing the maximum flow/minimum s-t cut in the employed graph construction. Drusen were defined as the regions between the segmented lRPE and BM. Method details were described in Chapter 5 Section 5.3.

Validation of drusen segmentation

An experienced OCT analyst (from Rotterdam group) masked to the algorithm output manually graded the severity of the drusen using a three-circle grid (as shown in Figure 4.13) on fundus photograph. The grid was consisted of three circles centering at fovea, which were named as the central, inner and outer subfields, respectively. For each of the subfields in the grid, the analyst graded from level 0 to level 4 (from mild to severe) based on the drusen coverage of that particular region. If the drusen coverage is less than 1%, the severity of the region was marked as level 0; if the drusen coverage is greater than or equal to 1% and less than 10%, the severity of the region was marked as level 1; if the drusen coverage is greater than or equal to 10% and less than 25%, the severity of the region was marked as level 2; if the drusen coverage is greater than or equal to 25% and less than 50%, the severity of the region was marked as level 3; if the drusen coverage is greater than or equal to 50%, the severity of the region was marked as level 4. Similar grading approach was introduced to the automated segmentation of drusen in OCT images. Fovea location was first automatically detected using the previously reported Iowa Reference Algorithm and the same three-circle grid on OCT enface view was constructed. Drusen footprint was then generated from the 3D segmentation result. In each of the three-circle regions,

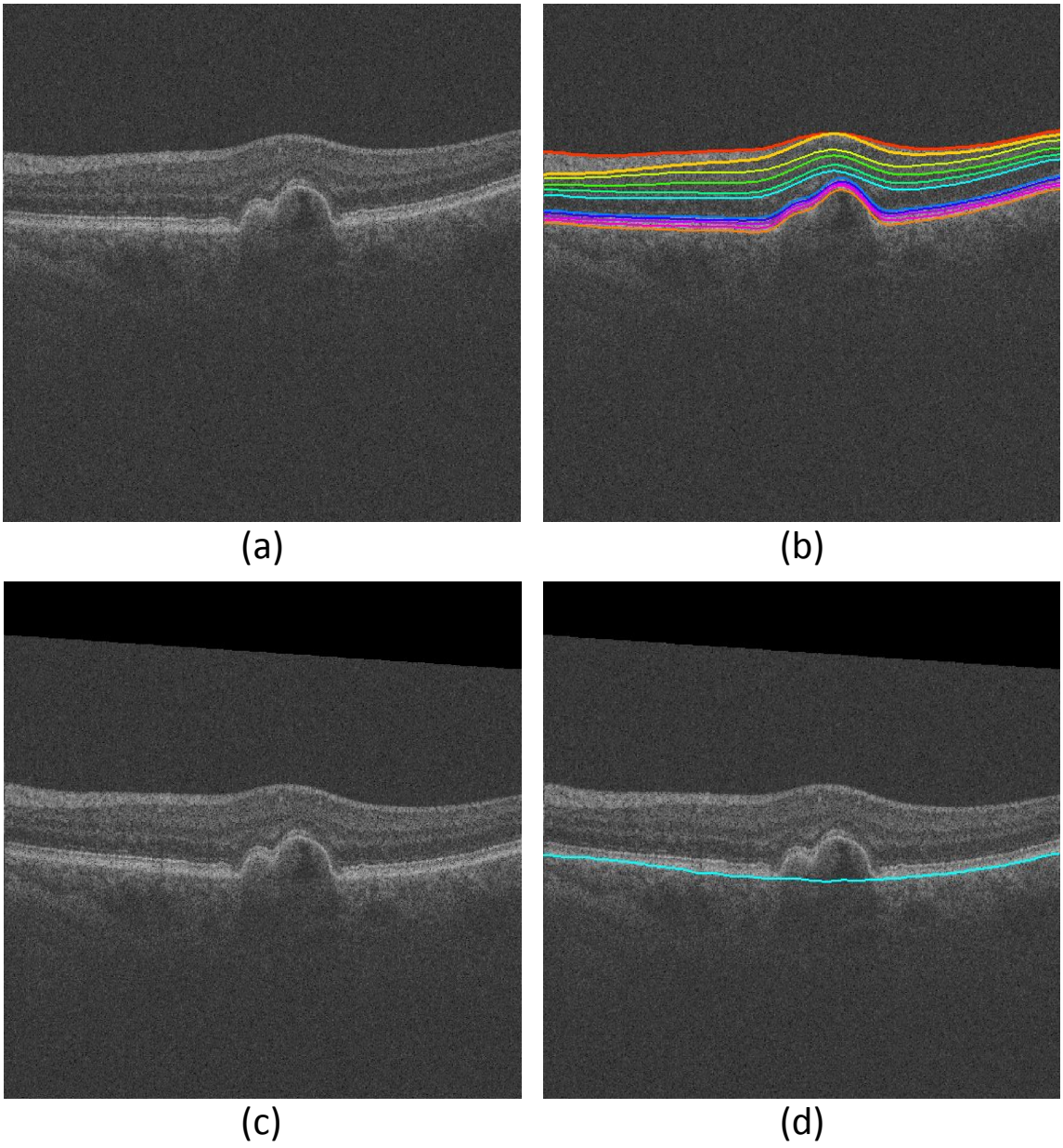

Figure 4.11: The preprocessing before drusen segmentation: (a) An example of original B-scan; (b) The same B-scan with 10 intra-retinal layer segmented; (c) The same B-scan after angle adjustment; (d) The same B-scan with Bruch's membrane segmented).

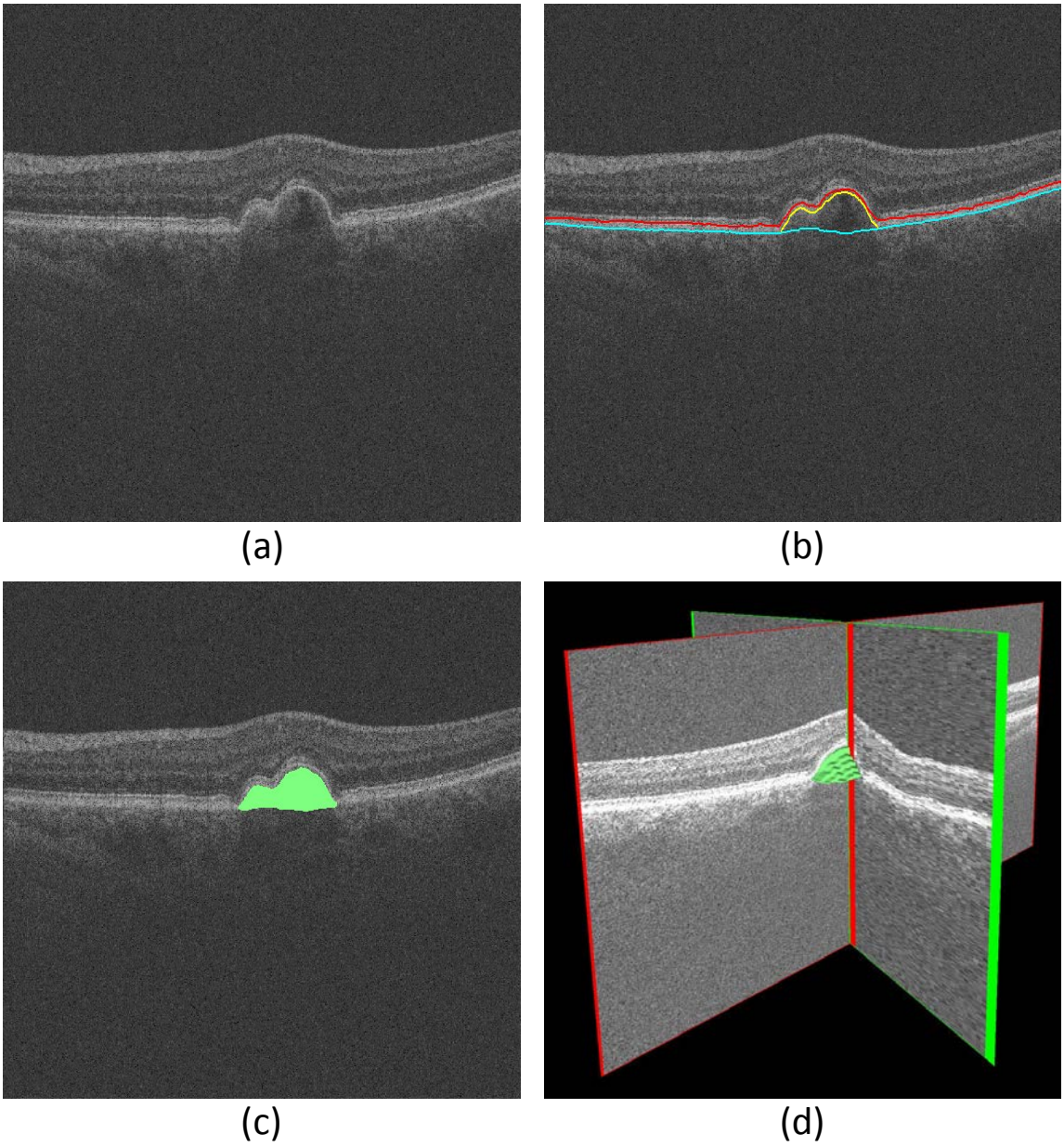

Figure 4.12: Drusen segmentation: (a) An example of original B-scan; (b) The same B-scan with 3 target surfaces segmented: upper RPE (red line), lower RPE (yellow line) and Bruch's membrane (light blue line); (c) The same B-scan with the overlay of 3D drusen segmentation result; (d) The 3D visualization of the drusen segmentation.

automatically determined drusen coverage was computed and grading level was given. A 5-by-5 confusion matrix was used to assess the agreement between automated grading results and manual grading results. Cohen's kappa value was introduced as the validation index of measuring inter-rater agreement: Cohen's kappa value yielded unity for the best agreement and null for the worst agreement (see Figure 4.14). To further evaluate the automated grading regionally, the 5-by-5 confusion matrices and Cohen's kappa values were performed on the central, inner and outer subfields of the three-circle grid.

Volume assessment of drusen load

The volume of drusen load was defined as the physical space between lower boundary of RPE and Bruch's membrane over the entire $6\times6mm^2$ macula-centered area. The volume were reported in mm^3.

Repeatability and reproducibility analysis

In forty-two (42) subjects out of the original 209 subjects, repeated scans were obtained with sufficient image quality (Lee et al. *Validation of Segmentability Index for Automated Prediction of Segmentation Reliability in SD-OCT Scans.* ARVO annual meeting 2015.). For each of these 42 subjects, reproducibility analysis of automated segmentation was performed on the pairs of repeated OCT images.

A 5-by-5 confusion matrix was used to assess the agreement between automated grading results and Cohen's kappa value was introduced as the validation index of measuring intra-rater agreement as well. To further test the reproducibility

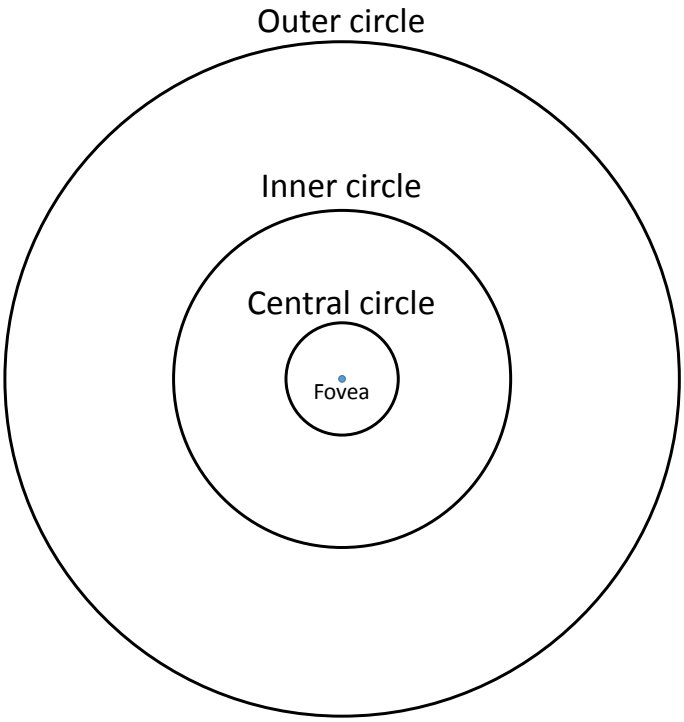

Figure 4.13: The grid was consisting of three circles, from inside to outside as central circle, inner circle and outer circle. All circles were centered at fovea. The radius of central circle was 0.5mm; the radius of inner circle was 1.5mm; the radius of outer circle was 3.0mm.

of the proposed automated method, dice coefficient of the segmentation results on two repeated scans was also reported. The dice coefficient yielded unity for the most overlap of the segmentation results and null for the least overlap.

Results

The agreement on the severity of drusen between automatically and manually determined grading levels was relatively good. As shown in the Figure (confusion

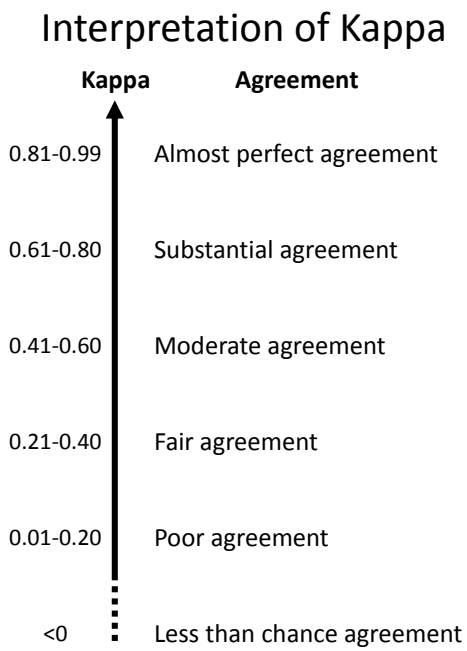

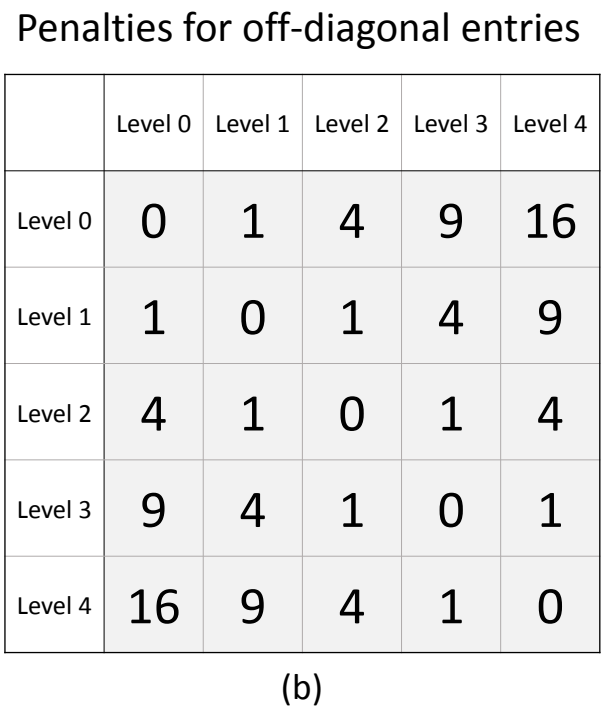

Figure 4.14: (a) The interpretation of Cohen's kappa value, larger value of kappa represented higher agreement; (b) The penalty weights for the entries in confusion matrix used for computing Cohen's kappa value, the diagonal entries were not penalized; the entries with distance of 1 to diagonal line were penalized by 1 (1^2); the entries with distance of 2 to diagonal line were penalized by 4 (2^2); the entries with distance of 3 to diagonal line were penalized by 9 (3^2); the entries with distance of 4 to diagonal line were penalized by 16 (4^2).

matrix), 627 grading values were assessed using confusion matrix. 43.5% of the automated grading values (273) exactly matched with manual results, 41.6% of the automated grading values (261) were off-diagonal with distance of one to the iden-

tical line (red diagonal cells), and 14.9% of the automated grading values (93) were off-diagonal with distance of more than or equal to two to the identical line (see Figure 4.15).

For the central subfield, 209 grading values were assessed using confusion matrix. 41.6% of the automated grading values (87) exactly matched with manual results, 37.8% of the automated grading values (79) were off-diagonal with distance of one to the identical line (red diagonal cells), and 20.6% of the automated grading values (43) were off-diagonal with distance of more than or equal to two to the identical line. For the inner subfield, 209 grading values were assessed using confusion matrix. 46.9% of the automated grading values (98) exactly matched with manual results, 45.5% of the automated grading values (95) were off-diagonal with distance of one to the identical line (red diagonal cells), and 7.6% of the automated grading values (16) were off-diagonal with distance of more than or equal to two to the identical line. For the outer subfield, 209 grading values were assessed using confusion matrix. 42.1% of the automated grading values (88) exactly matched with manual results, 41.6% of the automated grading values (87) were off-diagonal with distance of one to the identical line (red diagonal cells), and 16.2% of the automated grading values (34) were off-diagonal with distance of more than or equal to two to the identical line (see Figure 4.15).

In the Cohen's kappa analyses, the kappa value for the all grading levels was 0.551, corresponding to an "moderate" agreement. For the central subfield, the kappa value was 0.487, corresponding to an "moderate" agreement. For the inner subfield,

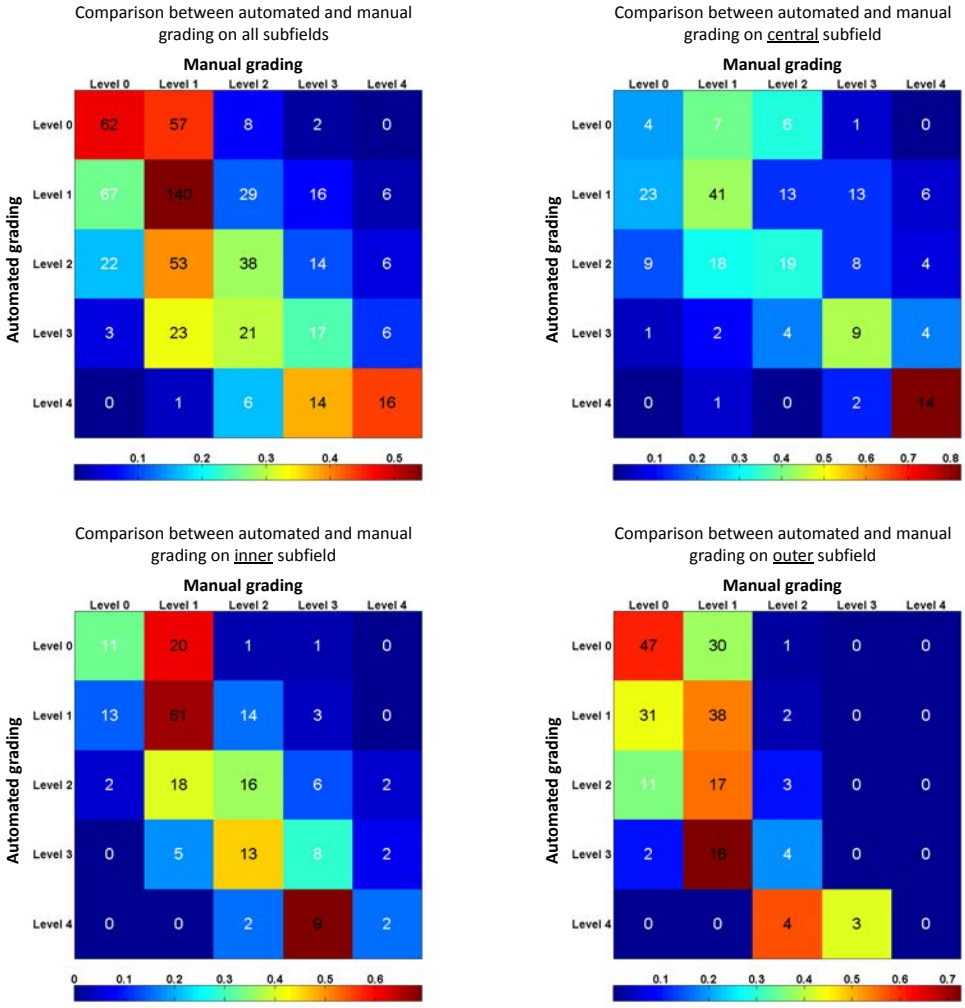

Figure 4.15: Confusion matrices: Upper-left panel: agreement on all subfields, 627 samples in total, 43.5% of the samples exactly matched. Upper-right panel: agreement on central subfield, 209 samples in total, 41.6% of the samples exactly matched. Lower-left panel: agreement on inner subfield, 209 samples in total, 46.9% of the samples exactly matched. Lower-right panel: agreement on outer subfield, 209 samples in total, 42.1% of the samples exactly matched.

the kappa value was 0.632, corresponding to an "substential" agreement. For the outer subfield, the kappa value was 0.401, corresponding to an "moderate" agreement.

The reproducibility analysis tested the automated grading on repeated scans from the same patient and showed that the segmentation results of the present method are highly reproducible. 126 grading values were assessed using confusion matrix. 81.0% of the automated grading values (102) exactly matched with manual results, 16.7% of the automated grading values (21) were off-diagonal with distance of one to the identical line, and 2.3% of the automated grading values (3) were off-diagonal with distance of more than or equal to two to the identical line (see Figure 4.16). The Cohen's kappa value was 0.894, corresponding to an "almost perfect" agreement.

For the 6×6 mm^2 macula-centered region as imaged by SD-OCT, average volume of drusen for each volumetric image was $0.033mm^3$. Reproducibility test of the overlapping areas was applied on the 3D voxel-based renderings of the automated segemntation. Average Dice coefficient was 0.803 ± 0.151 (95%CI, 0.758 - 0.849) (see Figure 4.17).

Discussion

The results of the presented study showed a fully automated three-dimensional method capable of segmenting the drusen in non-neovascular age-related macular degeneration, as well as of quantifying drusen volume in the regional and entire macular regions. The method worked on standard spectral-domain OCT images, in this study the Topcon OCT and enhanced depth imaging or high-definition techniques were not

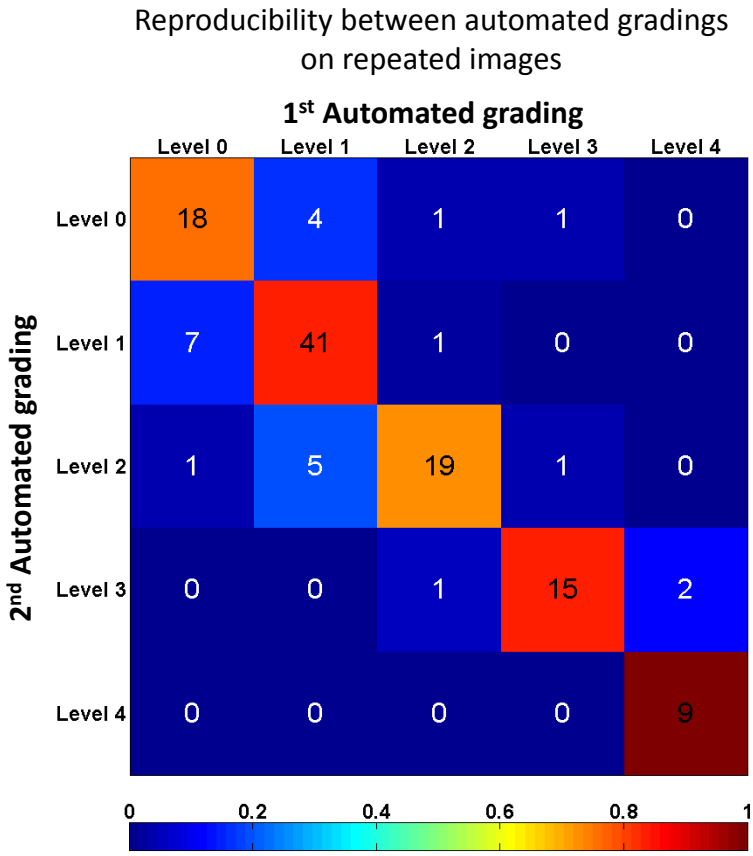

Figure 4.16: Confusion matrix of the reproducibility analysis: agreement on all subfields, 126 samples in total, 81.0% of the samples exactly matched. The Cohen's kappa value was about 0.90 representing an "almost perfect" agreement between the automated grading of drusen severity on repeated SD-OCT volumetric images.

used.

Compared with the manual grading process, the method automatically generated the severity grading of drusen. The comparison between automated and manual grading results showed a relatively good agreement on all subfields of the macula, with

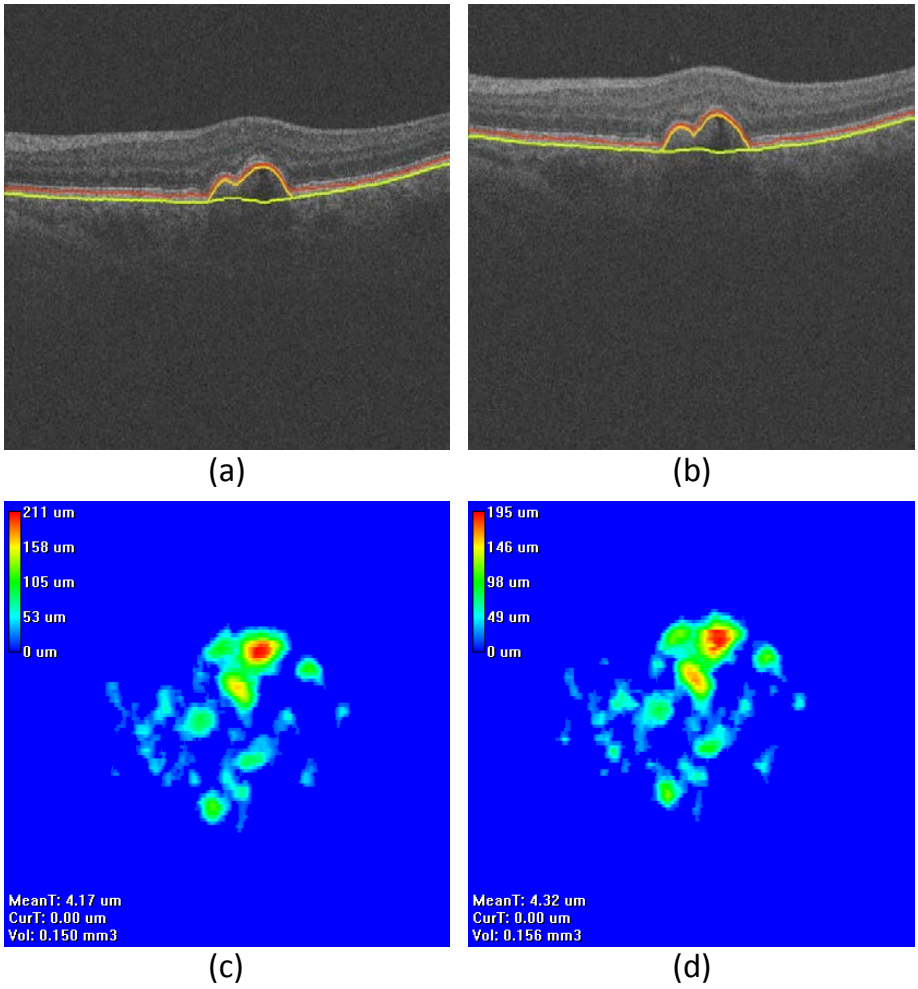

Figure 4.17: Reproducibility analysis of the 3D drusen segmentation results: panels (a) and (b) are example B-scans on the same location from two repeated SD-OCT images; panels (c) and (d) are corresponding drusen height maps over the entire 6×6 mm^2 macula-centered region.

Cohen's kappa value of 0.551 representing a moderate level of agreement. For all three subfields, the agreements between automated and manual grading were evaluated as good and the inner region (distance from 0.5mm to 1.5mm) showed an above-average

result among three subfields, marked as “substantial agreement”.

However, the exact matches between automated and manual grading results was about 50% of all samples. The key reason was possible to be that the manual grading process used the 2D color fundus photographs (CFP) and the automated algorithm was performed on 3D SD-OCT volumetric images. The grading drusen on CFP could be difficult due to the large variability of fundus pigmentation, media opacities, the variability of drusen appearance, the presence of small satellites of depigmentation consistent with atrophy and abnormal foldings around retinal nerve fiber layer. The reproducibility of the automated method was high, as shown by the confusion matrix of the repeated volumetric images, the corresponding Cohen’s kappa value and the dice coefficient assessing the overlapping area between the segmented drusen on the repeated scans.

There are several limitations to this study. First, due to the large data set, we did not use manual tracing of drusen outline to evaluate the automated segmentation of drusen. Although we compared the automated and manual results using a more clinically relevant index – the severity level of drusen, the comparison between real automatically determined and manually determined segmentation would improve the validity of our evaluation experiments. In a future study, we plan to evaluate the automatically segmented drusen on all B-scans with manual traced drusen outlines.

Second, the image quality of this dataset restricted the size of the samples in reproducibility analysis. Flipping and partially mirroring images were found occasionally from the SD-OCT images in the study. We are pursuing a following study

using all consorts of the Rotterdam Eye study. This issue should be solved with the increased size of the studying sample.

Third, all subjects underwent OCT imaging using same SD-OCT scanner. Each volumetric image had dimensions of 512 voxels temporal-nasally and 128 voxels on superior-inferiorly. This required us to use anisotropic smoothness constraints as more relaxed constraints on superior-inferior direction and less relaxed constraints on temporal-nasal direction. Furthermore, the gap between adjacent B-scans may miss real outline of drusen. We will apply this automated algorithm to OCT images from other companies and with more "C-scan isotropic" protocol settings.

In summary, we have developed a fully automated three-dimensional method for segmenting drusen in non-neovascular AMD, assessing the severity of drusen and quantifying the volume of drusen in SD-OCT volumetric data. The method yielded relatively good agreement comparing to a human determined severity of drusen. The reproducibility of the segmented drusen on repeated scans was also high. Previously, we have reported a fully automated segmentation of choroidal layer with graph-based algorithm. This may be combined with the proposed method. The joint segmentation of the choroid and drusen in 3D OCT volumetric images with non-neovascular AMD may reveal a clearer relationship between drusen and the choroidal layer. Potentially, our method may enhance the understanding of clinical information of drusen and improve the diagnosis and management of patients with non-neovascular AMD diseases.

CHAPTER 5
DEVELOPED METHODS IN THIS WORK

We developed multiple methods for segmenting different structures and layers in the posterior segment of human eye. In this chapter, we will introduce all the related methods in this work.

5.1 Similarity Constraint Graph-Cut-Graph-Search method

The choroid layer was identified immediately beneath Bruchs membrane. A sufficiently large sub-volume containing the choroid layer was selected as the target region to apply choroidal segmentation. As described in the previous vasculature based method [28], we applied multi-scale Hessian matrix analysis on the selected sub-volume. Three-dimensional vesselness map of the choroidal vasculature was then calculated. Probability values between 0 and 255 represented different vesselness of the choroidal vasculature. This vesselness contributed to the region cost in the graph-based method rather than a segmentation of the choroidal posterior boundary. Cost functions and graph representations were designed accordingly.

Cost functions: One surface cost was defined for the transitions from choroid to sclera. Due to the difference of the density between choroidal vasculature and sclera, the overall intensity of choroidal vasculature is lower than that of sclera. We introduced a dark-to-bright intensity gradient as for the surface between choroid and sclera. The surface cost formed one energy terms in the cost function: $\sum f_{c-s}(x, y, z)$. Object cost was defined as the region intensity difference inside and outside vessel

region of choroidal vasculature, forming another energy term as $\sum f_v(x, y, z)$. The following equation shows the energy function of our graph-based method:

$$C(G) = \sum f_{c-s}(x, y, z) + \sum f_v(x, y, z) \tag{5.1}$$

$\sum f_{c-s}(x, y, z)$ is the cost of relevant surface (transition) which are identical to the cost of a minimum closed set enveloped by the surface in the graph $\sum f_v(x, y, z)$ is defined as the region term of the energy function, which shows the likelihood of vertex-associated costs inside the vasculature regions.

Graph representation: The main idea for solving the energy optimization problem was to reduce it into a maximum-flow minimum cut graph problem. A graph $G = (V, E)$ as the collection of vertices V and arcs E was constructed for representing the problem. The specific constructions were described as follows:

Surface-specified sub-graphs: Similar to the configuration in [55], node costs were assigned according to the intensity values from the original OCT image. For each surface, a directed sub-graph as a part of entire graph G was constructed to present a non-empty closed set. An optimal surface segmentation problem can be converted to solving a minimum closed set problem in this directed sub-graph (see Figure 5.1).

Object-specified sub-graphs: As discussed in [53] and [54], object and background nodes were pre-determined by the detection of the choroidal vasculature. For the region term, t-links are assigned between terminals (source s, sink t) and vertices. The capacities of t-links were defined using the likelihood of whether the vertex was belongs to object set. For the boundary term, n-links were assigned between neigh-

boring vertices to represent whether these neighboring vertices should be in the same set (source set or sink set) (see Figure 5.1).

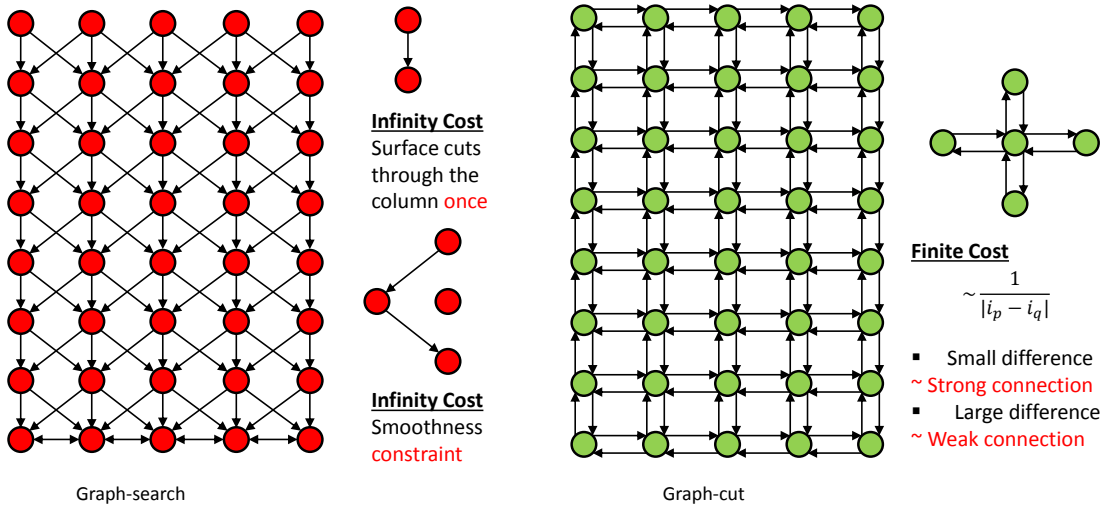

Figure 5.1: Left — Surface-specified sub-graph: Intra-column and inter-column arcs constructed close-sets. All arcs carried infinity cost. Vertical intra-column arc promised surface cut through the column only once and inter-column restricted the smoothness of the surface. Right — Object-specified sub-graph: Arcs with finite cost were added between adjacent nodes. The cost was inversely related to the absolute intensity difference such nodes.

Multi-object Interactions: As shown in [56], certain maximum and minimum distances were considered as the prior knowledge of the relative position among multiple surfaces and objects. Inter-subgraph arcs were introduced at the interacting

areas to represent the maximum and minimum distances between adjacent structures (see Figure 5.2).

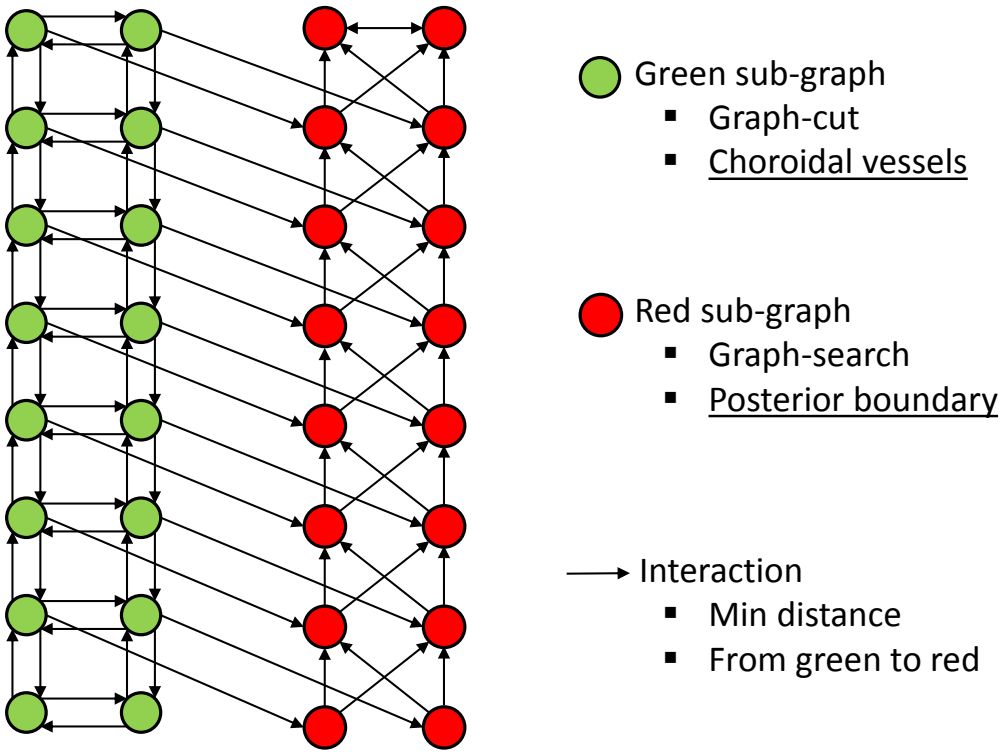

Figure 5.2: Inter-subgraph arcs were added for constraining the minimum distance between segmented vessels and segmented surface.

Similarity Constraints: The segmentation leak was a general issue in graph-cut method [42]. In this project, relatively low intensity contrast around choroidal boundary may cause "leaks" from the choroidal vessels to the sclera. Due to the interaction between the sub-graphs of graph-cut and graph-search, these "leaks" may

push the segmented choroidal posterior boundary into sclera resulting in segmentation errors. We thus developed similarity constraint using the vesselness map from Hessian analysis. The vesselness value was usually high in the central part of vessels and it was usually low around the edge of the vessel. The similarity constraint penalized the graph-cut if it cut through the regions of similar vesselness to reduce the segmentation leaks and to maintain the tube-like shape of choroidal vessels, as shown in the Figure 5.3.

5.2 Adaptive Costs and Constraints using Probability Map from 3D Voxel Classification

The previously reported multi-layer segmentation employed a strong distance constraint between myoid inner segment - ellipsoid inner segment (myoid IS - ellipsoid IS) and Bruch's membrane (BM) for enhancing the robustness when segmenting intra-retinal surfaces in normal subjects. However, in CNV scans, the increased thickness of the outer-retinal subretinal (ORSR) layers violates such distance constraints and may lead to segmentation errors. To improve the ORSR layer segmentation, we adjusted the costs and constraints in the original multi-layer segmentation [95] using the probability map from 3D voxel classification in [42].

Adaptive Costs: Originally, the cost images were generated using the vertical intensity gradients: 1. For the upper boundary of ORSR layer, dark-to-bright intensity transition was observed from outer nuclear layer (ONL) to photoreceptor cells. 2. For the lower boundary of ORSR layer, bright-to-dark intensity transition was found

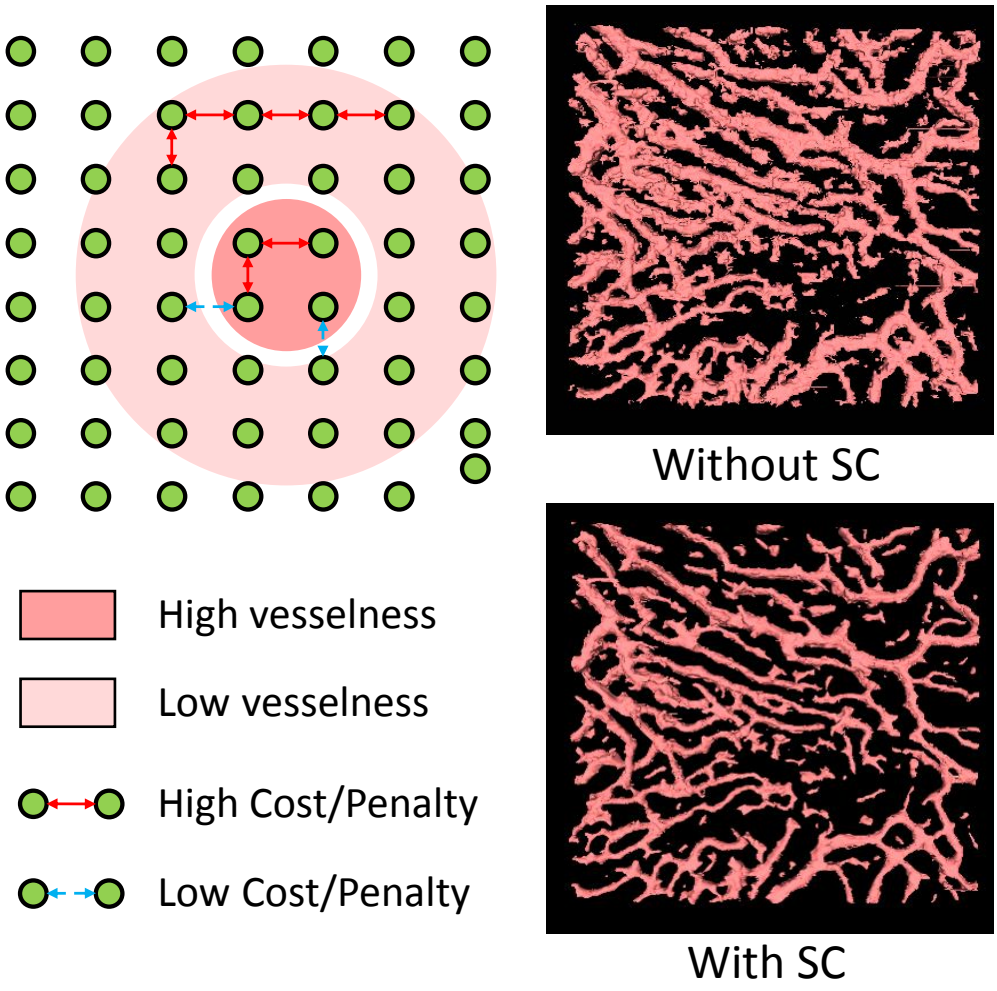

Figure 5.3: Left: High penalties were enforced between the nodes with similar vesselness values; low penalties were introduced between the nodes with large difference in vesselness. Right: On the top, the segmentation leaks occurred when graph-cut was used solely; on the bottem, the segmented vessels were much clean.

from RPE layer to the choroid. However, due to the presence of the fluid-filled abnormalities, noisy intensity transitions occurred in the outer-retinal subretinal space

and the segmented surface may wrongly cut through the fluid-filled regions. We thus modified the original cost in [95] by weighting the cost value with probability value for every voxel in the volume (see Figure 5.4).

$$Cost \times (1 - probability) = Adaptive\ Cost$$

Figure 5.4: Original costs were adjusted by the probability map from 3D voxel classification approach. The noisy intensity transitions in the fluid-filled regions were removed.

Adaptive Constraints: In CNV scan, ORSR layer thickens around fluid-filled regions and remains flat in normal regions. Thus, to achieve more accurate ORSR layer segmentation, different settings of distance constraints between upper and lower boundaries of ORSR layer were preferable. We used the probability map to differentiate the possible fluid regions and non-fluid regions. Relaxed distance constraint was then applied in the possible fluid regions and the constraints in normal (non-fluid)

regions continued using the original settings (see Figure 5.5).

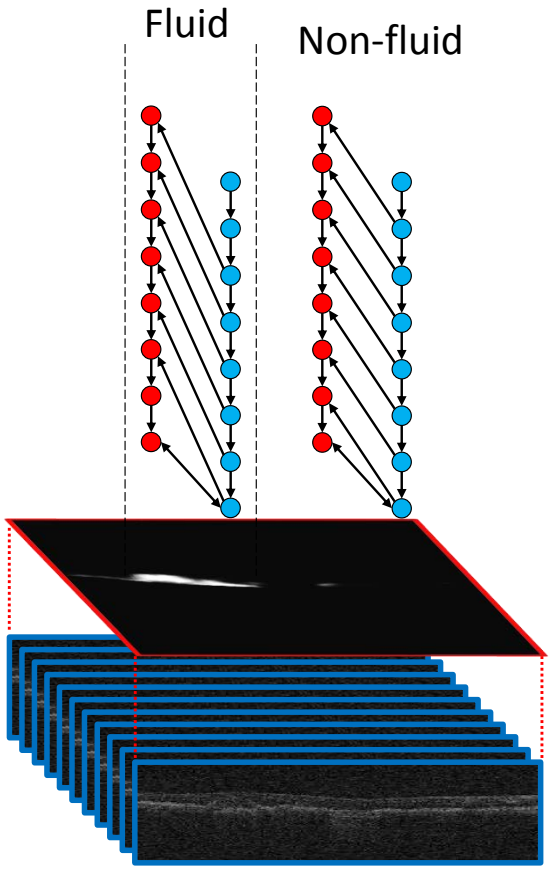

Figure 5.5: Distance constraints on the fluid regions were relaxed and that on the non-fluid regions remained the same as in original multi-layer segmentation.

5.3 Multi-Layer Segmentation using Different Surface Constraints

Virtual sub-RPE space was materialized by drusen in dry-AMD scans. In this project, we segmented drusen outlines by identifying the upper boundary or RPE

(uRPE), the lower boundary of RPE (lRPE) and BM. Depending on the shapes and appearances of these three surfaces, we applied different settings of surface constraints.

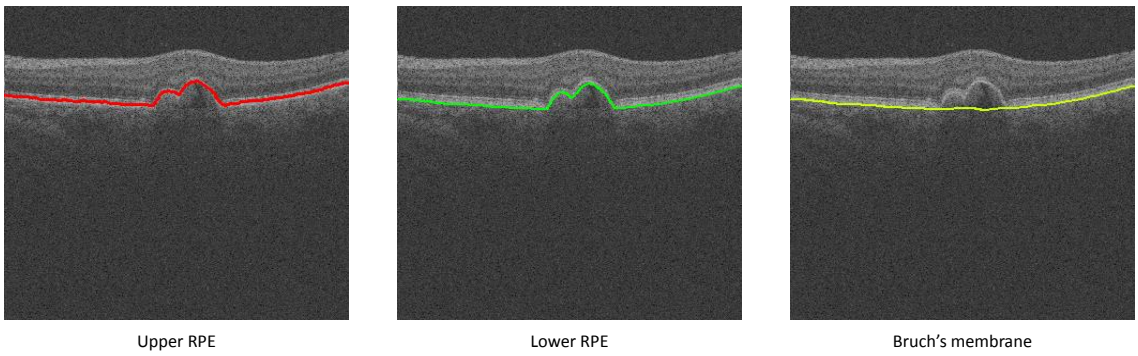

Figure 5.6: The upper and lower boundaries of RPE layer showed rapid changes around drusen. Bruch's membrane showed high stiffness and maintained curvature under drusen.

Upper and Lower Boundaries of RPE: As shown in Figure 5.6, rapid changes occurred on uPRE and lRPE, especially on the edge of the drusen steep slopes were usually observed in OCT. Thus, we introduced large smoothness constraints on these two surfaces (see Figure 5.7). To generate the cost function, dark-to-bright intensity transition was applied on uRPE and bright-to-dark intensity transition was added to lRPE. Retinal pigment epithelium (RPE) usually thins during the progression of AMD, thus, a certain distance constraint was implemented between uRPE and lRPE.

Bruch's Membrane: The stiffness of Bruch's membrane was relatively large

among the retinal layers. As shown in Figure 5.6, BM maintained the curvature under the drusen. Furthermore, BM and lRPE overlapped on the normal regions in the OCT volumetric scan. We thus used bright-to-dark intensity transition to create the cost image of BM. However, due to the absorption and backscattering of RPE, the intensity transition of BM was weak around drusen. The segmented surface of BM was highly possible to be attracted by the strong edge of lRPE. To improve the segmentation of BM, a symmetric bowl shape model was implemented by adjusting the arc connection on the sub-graph of BM. The average model of the hard constraint arcs appeared flatter on the central columns and steeper around the margin of the graph (see Figure 5.7).

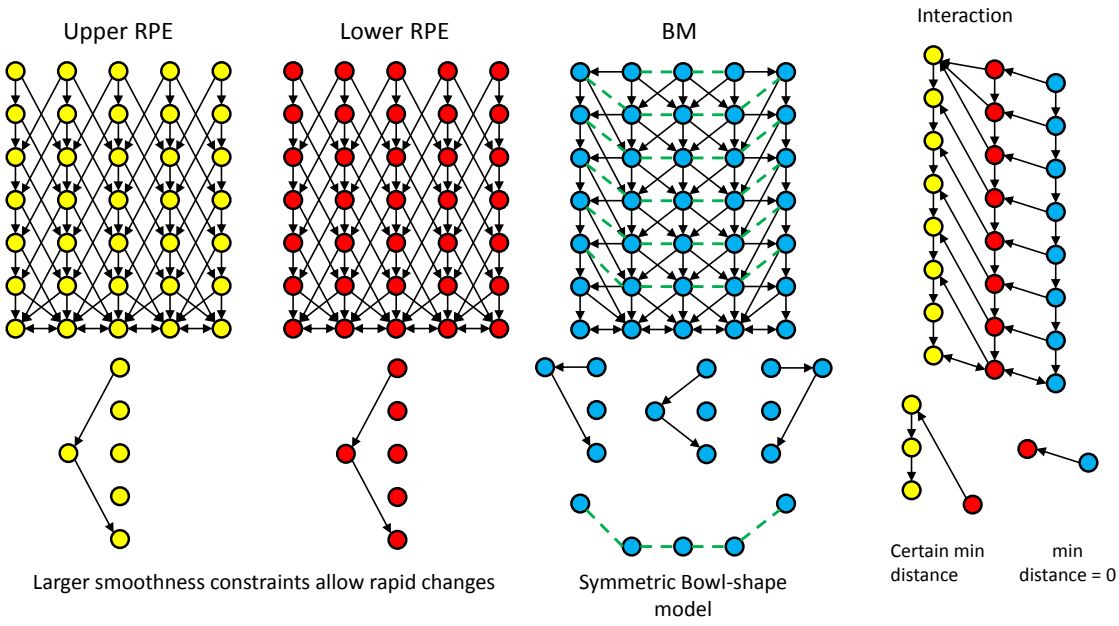

Figure 5.7: Upper RPE and Lower RPE: The smoothness constraints (hard constraints) of uRPE and lRPE were enlarged to fit the rapid changes of these two surfaces. BM: Symmetric bowl shape model was implemented to segment BM and the smoothness constraints of BM were not relaxed. Interaction: Certain distance constraint was added between uRPE and lRPE to enforce the real space of RPE layer. Meanwhile, the virtual space between lRPE and BM was only materialized around drusen and not elsewhere, we thus set minimum distance between lRPE and BM to zero.

CHAPTER 6
GENERAL DISCUSSION AND FUTURE DIRECTIONS

The methods developed for this thesis have a number of potential extensions. For most of the projects in this thesis, we use the clinically available spectral-domain optical coherence tomography (SD-OCT) images. A relatively low signal-to-noise ratio in these types of SD-OCT images limits the accuracy of the proposed methods. Recently, new OCT related techniques have been developed with higher resolution of image details and better intensity contrast for showing the borders of layers/objects. In this chapter, we present several possible extensions and applications of the our proposed methods.

6.1 Vascular and Capillaries Segmentation on OCT Angiography

Optical coherence tomography angiography (OCT angiography) has been developed for imaging ophthalmic micro-vascular structures. Jia et al. reported a split-spectrum amplitude-decorrelation angiography (SSADA) algorithm of generating three dimensional OCT angiography images. The original OCT imaging light has a raw full spectrum producing high-resolution OCT imaging frames (B-scans). The main idea of SSADA is to split the raw full spectrum into multiple spectrums with narrower bandwidths. These "sub-spectrums" produce more OCT imaging frames with lower OCT axial resolution, which are used to compute the decorrelation images. The decorrelation images are determined at each of the narrower spectrum separately and averaged in an inter-B-scan fashion. All decorrelation images for the

same OCT B-scan are then averaged from the multiple narrower spectrums yielding high-quality OCT angiograms. Figure 6.1 shows an en-face view of the OCT angiography imaging of a macula-centered region.

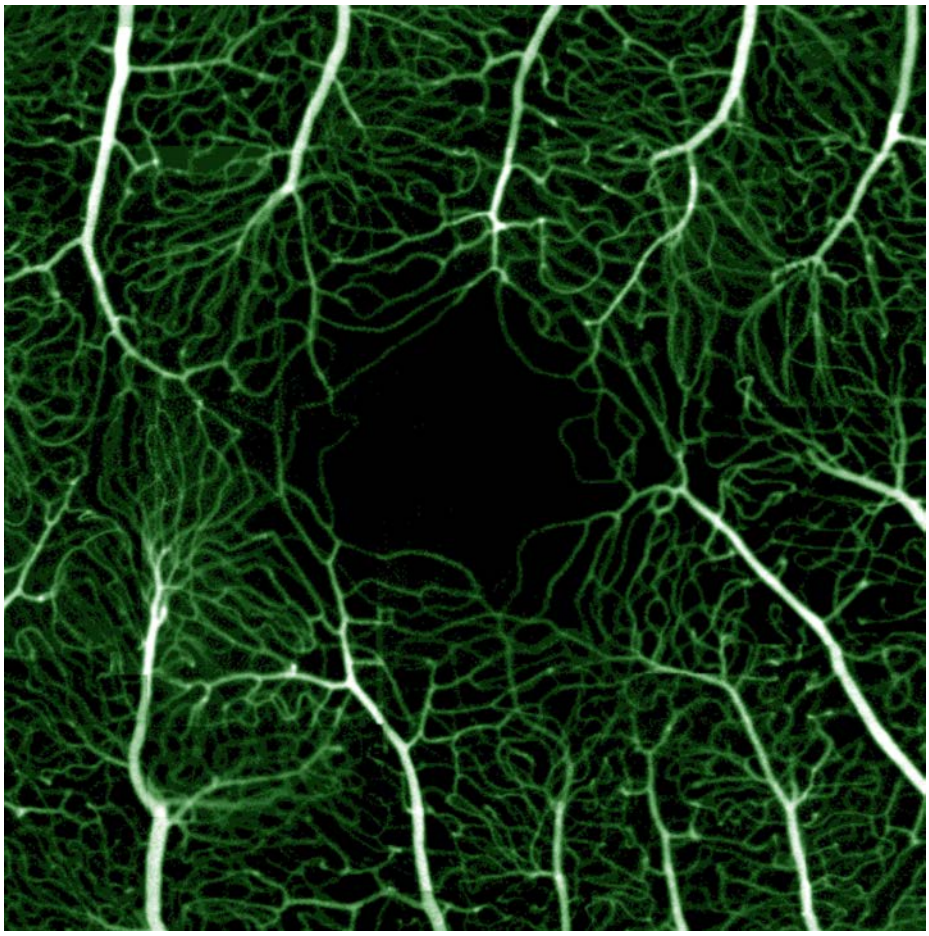

Figure 6.1: Optical coherence tomography angiography imaging over the macula-centered region. Image from https://www.pinterest.com/garchiapet/science/

As described in Chapter 3, vascular structures could be segmented using Hes-

sian analysis based approaches. In a preliminary study, we analyzed few phase-variance OCT volumetric images. These images were similar to the OCT angiography for visualizing vasculature and capillaries, only with more noise. As shown in the Figure 6.2, segmentations of retinal vasculature and capillaries were achieved in 3D phase-variance OCT images. With higher image quality of OCT angiography, we could be possible to create better segmentation of retinal vasculature and capillaries, and also choroidal vessels and choriocapillaris.

6.2 Local Environment of the Drusen in Dry AMD Disease

To study the relationship between retinal structures is of great importance, especially for those with ocular diseases. In this thesis, we have reported individual segmentations of the choroidal layers and drusen. Since macular structures are affected by drusen in nonneovascular AMD, we plan to study the changes of micro-environment of drusen, including photoreceptor cells (outer segments), retinal pigment epithelium (RPE) layer and choriocapillaris.

Choriocapillaris thinning is considered to be associated with the progression of drusen in nonneovascular AMD. In a preliminary study, local/regional quantification of choriocapillaris thickness was achieved in the region around individual drusen. Sixty-nine patients with dry AMD underwent OCT imaging using Heidelberg Spectralis SD-OCT with enhanced depth mode. We segmented choriocapillaris and drusen using the proposed methods discussed in Chapters 3 and 4. Local choriocapillaris thicknesses were averaged over the drusen region as well as in circular regions of 20,

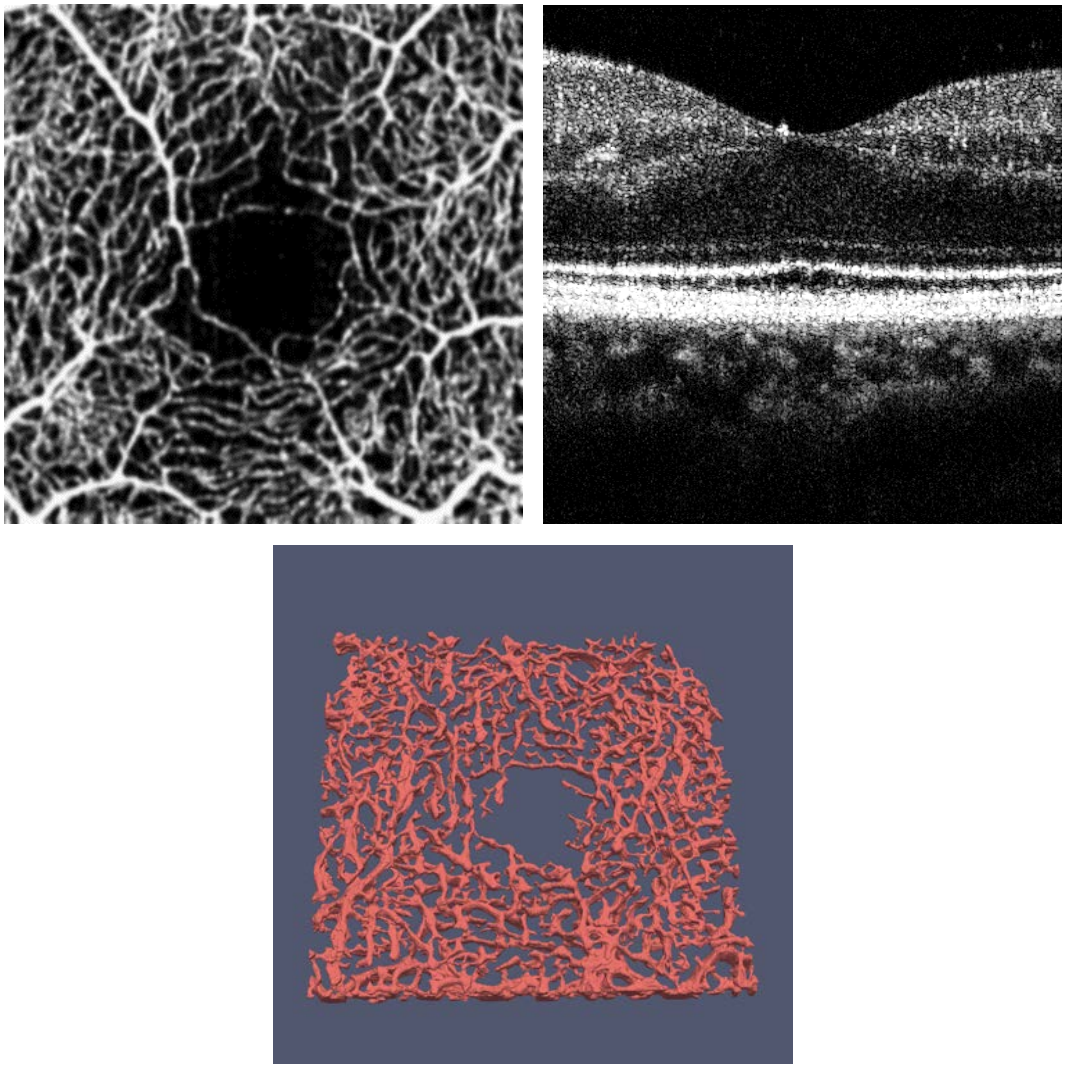

Figure 6.2: (a) The en-face projection of the retinal vasculature and capillaries; (b) An example B-scans of the phase-variance OCT image; (c) three-dimensional rendering of vessel segmentation.

40, ..., 160 microns around drusen. We found that choriocapillaris was significantly thinner ($8.46\mu m$ on average) under the drusen than everywhere else (Figure below). This result is compatible with the findings in histology research [124]. The choriocap-

illaris layer was significantly thicker just outside (20 to 40μm) the drusen boundary (9.19μm on average) (see Figure 6.3).

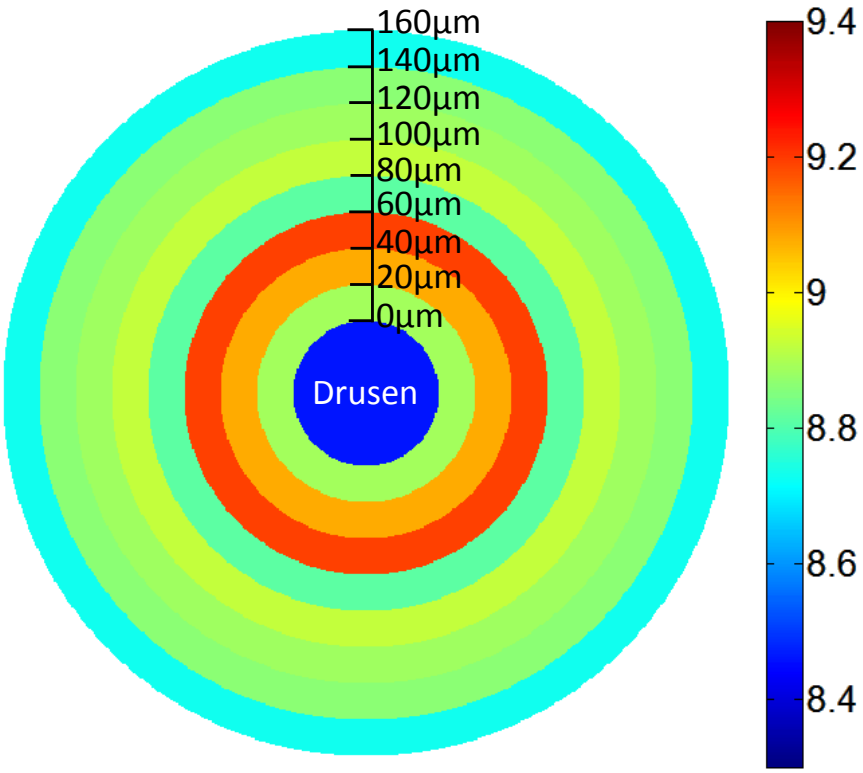

Figure 6.3: Average thickness map in concentric rings from zero to 160 microns outside of drusen are 8.46±0.91μm, 8.89±0.59μm, 9.08±0.60μm, 9.19±0.66μm, 8.81±0.73μm, 8.92±0.87μm, 8.88±0.90μm, 8.86±0.93μm, and 8.73±0.94μm.

Our preliminary results confirmed thinner choriocapillaris under drusen as previously observed on histology, leading to a hypothesis that thinner choriocapillaris under drusen may be caused by lack of blood flow in ghost vessels, as shown in Figure

6.4. For the future study, a larger population could be helpful to answer whether the intriguing finding of slightly thickens choriocapillaris just outside of drusen regions.

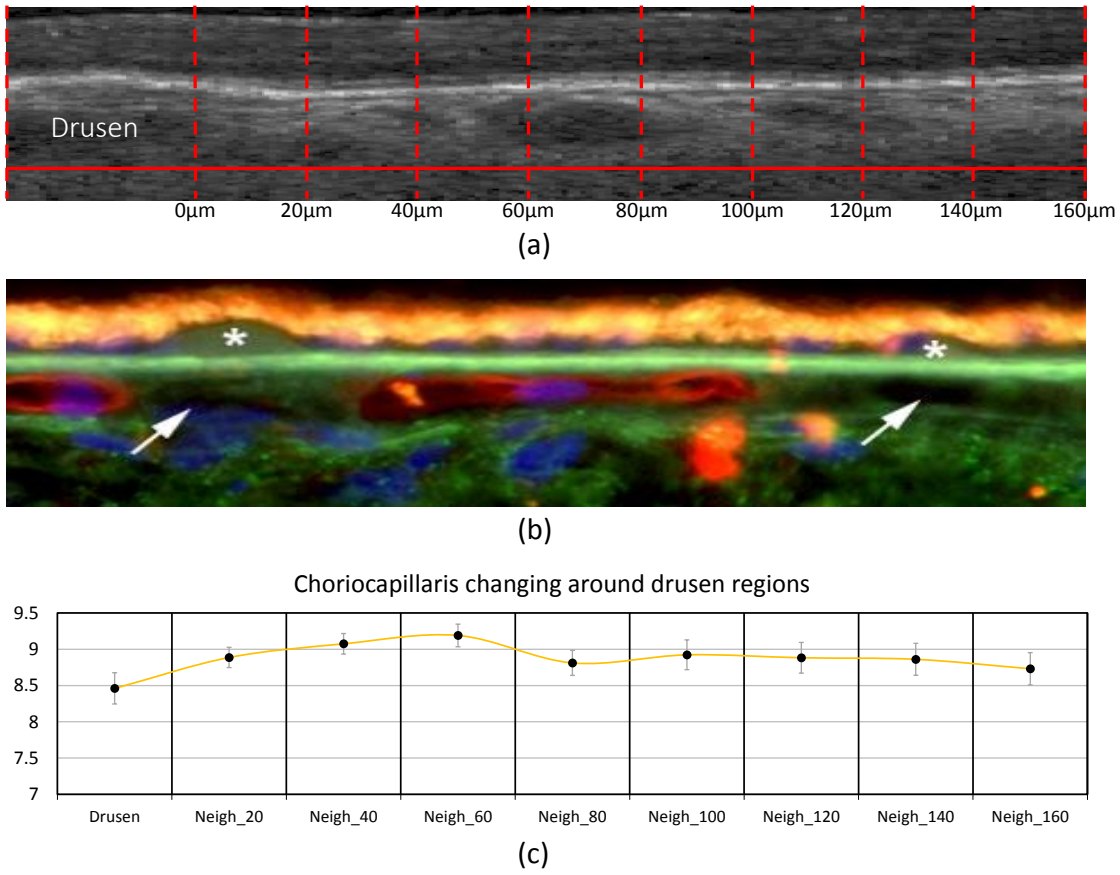

Figure 6.4: (a) and (b) Unrelated OCT image and histology show local environment of drusen and choriocapillaris. Drusen marked by asterisks, ghost vessels by arrows notice the colocation of drusen and ghost vessels. (c) Average thickness plots shows the profile of choriocapillaris in drusen local environment.

CHAPTER 7
CONCLUSIONS

To summarize, first recall the specific aims for this thesis:

- **Aim 1:** Develop and validate methods for segmenting choroid, including choroidal vasculature and the boundaries of choroid layers.
- **Aim 2:** Develop and validate methods for segmenting subretinal tissues, including RPE, photoreceptors in the face of disruptions of the outer retinal architecure caused by retinal diseases. Develop and validate methods for segmenting the realized virtual spaces sketched above including drusen.
- **Aim 3:** Integrate and analyze segmentation results to obtain more clinically useful information.

Chapter 3 introduced two distinctive methods for segmenting the choroidal vasculature and the boundaries of choroid layers (Aim 1). On one hand, the Hessian-analysis based method generated a highly reproducible segmentation of the choroidal vasculature, providing a robust way of assessing the choroidal vessel volume and density in normal or diseased eyes. On the other hand, the graph-based method proposed a 3D fully automated segmentation of the choroidal boundaries, catering for the growing needs for the quantitative analysis of choroidal thickness over all frames in the OCT images.

The developed methods for segmenting sub-retinal tissues were described in Chapter 4 (Aim 2). We considered the space from photoreceptor layer to Bruch's

membrane as one combined layer, named outer-retinal sub-retinal (ORSR) layer. Thickness changes of ORSR layer implied the growth of abnormal regions in this space. The second part of Chapter 4 proposed and validated a robust 3D fully automated segmentation of drusen in non-neovascular AMD.

In the discussions of the above four methods, we studied clinical significance of the segmentation results (Aim 3). The Choroidal vasculature segmentation showed that the thinning of choroidal and choriocapillaris was associated with aging. The graph-based choroidal boundary segmentation assessed the difference of choroidal segmentability between swept-source OCT and spetra-domain OCT. The ORSR layer segmentation provided a general evaluation of the outer retinal thickness. The presences of sub-retinal fluid, PED, and dursen were thus reflected on the thickness changes of ORSR layer. The drusen segmentation showed direct clinical usage of the automated severity grading of drusen load in OCT volumetric data. Finally, in Chapter 6, we provided a few preliminary results to show the possible extensions of the proposed developments to new imaging modalities and also revealed the significance of interpreting clinical biomarkers from the segmentation results (Aim 3).

The success of the research discribed in this thesis owes to everyone in Iowa Retinal Analysis Lab. The completion of this thesis is largely benefited from the guidance of Professor Sonka and Professor Abràmoff and comments of other labmates. My contribution could be sumarized as follows:

- **Aim 1:** (1) Realize the Hessian analysis and thin-plate-spline approaches on Choroidal vasculature segmentation; (2) Design the convex arc model of Bruch's membrane and implement the model in soft-contraint graph-search framework for segmenting choroidal boundaries.
- **Aim 2:** (1) Develop the pipeline of ORSR layer segmentation, combining the 3D voxel classification results with multi-surface segmentation. (2) Design and validate the method utilizing shape-prior information and adaptive constraints for assessing severity and load of drusen.
- **Aim 3:** Evaluate the validity of the methods and discuss the clinical usefulness of the segmentation results.

In summary, the aims of this thesis were fulfilled. This thesis has focused on the segmentations of multiple retinal and choroidal structures. The developed methods have the potential to improve the diagnosis, analysis, and management of a variety of eye disease.

REFERENCES

[1] Catherine Cukras, Yunqing D Wang, Catherine B Meyerle, Farzin Forooghian, Emily Y Chew, and Wai T Wong. Optical coherence tomography-based decision making in exudative age-related macular degeneration: comparison of time-vs spectral-domain devices. *Eye*, 24(5):775–783, 2009.

[2] Joel S Schuman, Michael R Hee, Adarsh V Arya, Tamar Pedut-Kloizman, Carmen A Puliafito, James G Fujimoto, and Eric A Swanson. Optical coherence tomography: a new tool for glaucoma diagnosis. *Current opinion in ophthalmology*, 6(2):89–95, 1995.

[3] Michael R Hee, Carmen A Puliafito, Jay S Duker, Elias Reichel, Jeffrey G Coker, Jason R Wilkins, Joel S Schuman, Eric A Swanson, and James G Fujimoto. Topography of diabetic macular edema with optical coherence tomography. *Ophthalmology*, 105(2):360–370, 1998.

[4] Wolfgang Drexler and James G Fujimoto. State-of-the-art retinal optical coherence tomography. *Progress in retinal and eye research*, 27(1):45–88, 2008.

[5] N Nassif, B Cense, B Park, Me Pierce, S Yun, B Bouma, G Tearney, T Chen, and J de Boer. In vivo high-resolution video-rate spectral-domain optical coherence tomography of the human retina and optic nerve. *Optics Express*, 12(3):367–376, 2004.

[6] Michael R Hee, Joseph A Izatt, Eric A Swanson, David Huang, Joel S Schuman, Charles P Lin, Carmen A Puliafito, and James G Fujimoto. Optical coherence tomography of the human retina. *Archives of ophthalmology*, 113(3):325–332, 1995.

[7] Mona Kathryn Garvin, Michael D Abràmoff, Xiaodong Wu, Stephen R Russell, Trudy L Burns, and Milan Sonka. Automated 3-d intraretinal layer segmentation of macular spectral-domain optical coherence tomography images. *Medical Imaging, IEEE Transactions on*, 28(9):1436–1447, 2009.

[8] Rama D Jager, William F Mieler, and Joan W Miller. Age-related macular degeneration. *New England Journal of Medicine*, 358(24):2606–2617, 2008.

[9] Neil M Bressler. Age-related macular degeneration is the leading cause of blindness... *Jama*, 291(15):1900–1901, 2004.

[10] Frederick L Ferris, CP Wilkinson, Alan Bird, Usha Chakravarthy, Emily Chew,

Karl Csaky, SriniVas R Sadda, Beckman Initiative for Macular Research Classification Committee, et al. Clinical classification of age-related macular degeneration. *Ophthalmology*, 120(4):844–851, 2013.

[11] Yogesan Kanagasingam, Alauddin Bhuiyan, Michael D Abràmoff, R Theodore Smith, Leonard Goldschmidt, and Tien Y Wong. Progress on retinal image analysis for age related macular degeneration. *Progress in retinal and eye research*, 38:20–42, 2014.

[12] Daniel Ardeljan and Chi-Chao Chan. Aging is not a disease: distinguishing age-related macular degeneration from aging. *Progress in retinal and eye research*, 37:68–89, 2013.

[13] James C Folk and Edwin M Stone. Ranibizumab therapy for neovascular age-related macular degeneration. *New England Journal of Medicine*, 363(17):1648–1655, 2010.

[14] Christine A Curcio, Kenneth R Sloan, Robert E Kalina, and Anita E Hendrickson. Human photoreceptor topography. *Journal of Comparative Neurology*, 292(4):497–523, 1990.

[15] MJ Hogan. Role of the retinal pigment epithelium in macular disease. *Transactions of the American Academy of Ophthalmology and Otolaryngology*, 76(1):64–80, 1972.

[16] John W Crabb, Masaru Miyagi, Xiaorong Gu, Karen Shadrach, Karen A West, Hirokazu Sakaguchi, Motohiro Kamei, Azeem Hasan, Lin Yan, Mary E Rayborn, et al. Drusen proteome analysis: an approach to the etiology of age-related macular degeneration. *Proceedings of the National Academy of Sciences*, 99(23):14682–14687, 2002.

[17] Michael J Heiferman, Joshua K Fernandes, Marion Munk, Rukhsana G Mirza, Lee M Jampol, and Amani A Fawzi. Reticular pseudodrusen on infrared imaging are topographically distinct from subretinal drusenoid deposits on en face optical coherence tomography. *Retina (Philadelphia, Pa.)*, 2015.

[18] AC Bird. Pathogenesis of retinal pigment epithelial detachment in the elderly; the relevance of bruch's membrane change. *Eye*, 5(1):1–12, 1991.

[19] M_F Marmor. Control of subretinal fluid: experimental and clinical studies. *Eye*, 4(2):340–344, 1990.

[20] Jayakrishna Ambati, Balamurali K Ambati, Sonia H Yoo, Sean Ianchulev, and

Anthony P Adamis. Age-related macular degeneration: etiology, pathogenesis, and therapeutic strategies. *Survey of ophthalmology*, 48(3):257–293, 2003.

[21] Meindert Niemeijer, Bram van Ginneken, Stephen R Russell, Maria SA Suttorp-Schulten, and Michael D Abramoff. Automated detection and differentiation of drusen, exudates, and cotton-wool spots in digital color fundus photographs for diabetic retinopathy diagnosis. *Investigative ophthalmology & visual science*, 48(5):2260–2267, 2007.

[22] Age-Related Eye Disease Study Research Group et al. The age-related eye disease study system for classifying age-related macular degeneration from stereoscopic color fundus photographs: the age-related eye disease study report number 6. *American journal of ophthalmology*, 132(5):668, 2001.

[23] Richard F Spaide and James M Klancnik Jr. Fundus autofluorescence and central serous chorioretinopathy. *Ophthalmology*, 112(5):825–833, 2005.

[24] Debora L Nickla and Josh Wallman. The multifunctional choroid. *Progress in retinal and eye research*, 29(2):144–168, 2010.

[25] Maria Wang, Inger Christine Munch, Pascal W Hasler, Christian Prünte, and Michael Larsen. Central serous chorioretinopathy. *Acta ophthalmologica*, 86(2):126–145, 2008.

[26] Richard F Dreyer and J Donald M Gass. Multifocal choroiditis and panuveitis: a syndrome that mimics ocular histoplasmosis. *Archives of ophthalmology*, 102(12):1776, 1984.

[27] Richard F Spaide. Age-related choroidal atrophy. *American journal of ophthalmology*, 147(5):801–810, 2009.

[28] Li Zhang, Kyungmoo Lee, Meindert Niemeijer, Robert F Mullins, Milan Sonka, and Michael D Abramoff. Automated segmentation of the choroid from clinical SD-OCT. *Investigative ophthalmology & visual science*, 53(12):7510–7519, 2012.

[29] Jessica M Skeie, Jasmine Hernandez, Aleksander Hinek, and Robert F Mullins. Molecular responses of choroidal endothelial cells to elastin derived peptides through the elastin-binding protein (glb1). *Matrix Biology*, 31(2):113–119, 2012.

[30] Robert F Mullins, Aaron D Dewald, Luan M Streb, Kai Wang, Markus H Kuehn, and Edwin M Stone. Elevated membrane attack complex in human choroid with high risk complement factor h genotypes. *Experimental eye research*, 93(4):565–567, 2011.

[31] Frank G Holz, Caren Bellman, Stephanie Staudt, Florian Schütt, and Hans E Völcker. Fundus autofluorescence and development of geographic atrophy in age-related macular degeneration. *Investigative ophthalmology & visual science*, 42(5):1051–1056, 2001.

[32] Jay Chhablani, Giulio Barteselli, Haiyan Wang, Sharif El-Emam, Igor Kozak, Aubrey L Doede, Dirk-Uwe Bartsch, Lingyun Cheng, and William R Freeman. Repeatability and reproducibility of manual choroidal volume measurements using enhanced depth imaging optical coherence tomography. *Investigative ophthalmology & visual science*, 53(4):2274–2280, 2012.

[33] Joong Won Shin, Yong Un Shin, and Byung Ro Lee. Choroidal thickness and volume mapping by a six radial scan protocol on spectral-domain optical coherence tomography. *Ophthalmology*, 119(5):1017–1023, 2012.

[34] Zhihong Hu, Xiaodong Wu, Yanwei Ouyang, Yanling Ouyang, and Srinivas R Sadda. Semiautomated segmentation of the choroid in spectral-domain optical coherence tomography volume scans. *Investigative ophthalmology & visual science*, 54(3):1722–1729, 2013.

[35] Jing Tian, Pina Marziliano, Mani Baskaran, Tin Aung Tun, and Tin Aung. Automatic segmentation of the choroid in enhanced depth imaging optical coherence tomography images. *Biomedical optics express*, 4(3):397–411, 2013.

[36] Lian Duan, Masahiro Yamanari, and Yoshiaki Yasuno. Automated phase retardation oriented segmentation of chorio-scleral interface by polarization sensitive optical coherence tomography. *Optics express*, 20(3):3353–3366, 2012.

[37] Delia Cabrera Fernandez. Delineating fluid-filled region boundaries in optical coherence tomography images of the retina. *Medical Imaging, IEEE Transactions on*, 24(8):929–945, 2005.

[38] Weiguang Ding, Mei Young, Serge Bourgault, Sieun Lee, David A Albiani, Andrew W Kirker, Farzin Forooghian, Marinko V Sarunic, Andrew B Merkur, and Mirza Faisal Beg. Automatic detection of subretinal fluid and sub-retinal pigment epithelium fluid in optical coherence tomography images. In *Engineering in Medicine and Biology Society (EMBC), 2013 35th Annual International Conference of the IEEE*, pages 7388–7391. IEEE, 2013.

[39] Gwénolé Quellec, Kyungmoo Lee, Martin Dolejsi, Mona Kathryn Garvin, Michael D Abràmoff, and Milan Sonka. Three-dimensional analysis of retinal layer texture: identification of fluid-filled regions in SD-OCT of the macula. *Medical Imaging, IEEE Transactions on*, 29(6):1321–1330, 2010.

[40] Christian Ahlers, Christian Simader, Wolfgang Geitzenauer, Geraldine Stock, Paul Stetson, Shawn Dastmalchi, and Ursula Schmidt-Erfurth. Automatic segmentation in three-dimensional analysis of fibrovascular pigmentepithelial detachment using high-definition optical coherence tomography. *British Journal of Ophthalmology*, 92(2):197–203, 2008.

[41] Martin Dolejší, Michael D Abràmoff, Milan Sonka, and Jan Kybic. Semi-automated segmentation of symptomatic exudate-associated derangements (SEADs) in 3D OCT using layer segmentation. Biosignal, 2010.

[42] Xinjian Chen, Meindert Niemeijer, Li Zhang, Kyungmoo Lee, Michael D Abràmoff, and Milan Sonka. Three-dimensional segmentation of fluid-associated abnormalities in retinal OCT: probability constrained graph-search-graph-cut. *Medical Imaging, IEEE Transactions on*, 31(8):1521–1531, 2012.

[43] JNP Kirkpatrick, T Spencer, A Manivannan, PF Sharp, and JV Forrester. Quantitative image analysis of macular drusen from fundus photographs and scanning laser ophthalmoscope images. *Eye*, 9(1):48–55, 1995.

[44] Zakaria Ben Sbeh, Laurent D Cohen, Gérard Mimoun, and Gabriel Coscas. A new approach of geodesic reconstruction for drusen segmentation in eye fundus images. *Medical Imaging, IEEE Transactions on*, 20(12):1321–1333, 2001.

[45] Gwenole Quellec, Stephen R Russell, Todd E Scheetz, Edwin M Stone, and Michael D Abràmoff. Computational quantification of complex fundus phenotypes in age-related macular degeneration and stargardt disease. *Investigative ophthalmology & visual science*, 52(6):2976–2981, 2011.

[46] Gwenole Quellec, Stephen R Russell, Johanna M Seddon, Robyn Reynolds, Todd Scheetz, Vinit B Mahajan, Edwin M Stone, and Michael D Abràmoff. Automated discovery and quantification of image-based complex phenotypes: a twin study of drusen phenotypes in age-related macular degeneration. *Investigative ophthalmology & visual science*, 52(12):9195–9206, 2011.

[47] Stephanie J Chiu, Joseph A Izatt, Rachelle V O'Connell, Katrina P Winter, Cynthia A Toth, and Sina Farsiu. Validated automatic segmentation of amd pathology including drusen and geographic atrophy in SD-OCT images. *Investigative ophthalmology & visual science*, 53(1):53–61, 2012.

[48] Pascal A Dufour, Lala Ceklic, Hannan Abdillahi, Simon Schroder, Sandro De Dzanet, Ute Wolf-Schnurrbusch, and Jens Kowal. Graph-based multi-surface segmentation of OCT data using trained hard and soft constraints. *Medical Imaging, IEEE Transactions on*, 32(3):531–543, 2013.

[49] Sandrine A Zweifel, Yutaka Imamura, Theodore C Spaide, Takamitsu Fujiwara, and Richard F Spaide. Prevalence and significance of subretinal drusenoid deposits (reticular pseudodrusen) in age-related macular degeneration. *Ophthalmology*, 117(9):1775–1781, 2010.

[50] Christine A Curcio, Jeffrey D Messinger, Kenneth R Sloan, Gerald McGwin, Nancy E Medeiros, and Richard F Spaide. Subretinal drusenoid deposits in non-neovascular age-related macular degeneration: morphology, prevalence, topography, and biogenesis model. *Retina (Philadelphia, Pa.)*, 33(2), 2013.

[51] Michael D Abràmoff, Mona K Garvin, and Milan Sonka. Retinal imaging and image analysis. *Biomedical Engineering, IEEE Reviews in*, 3:169–208, 2010.

[52] Yoshiaki Yasuno, Youngjoo Hong, Shuichi Makita, Masahiro Yamanari, Masahiro Akiba, Masahiro Miura, and Toyohiko Yatagai. In vivo high-contrast imaging of deep posterior eye by 1-um swept source optical coherence tomography and scattering optical coherence angiography. *Optics express*, 15(10):6121–6139, 2007.

[53] Yuri Boykov and Vladimir Kolmogorov. An experimental comparison of min-cut/max-flow algorithms for energy minimization in vision. *Pattern Analysis and Machine Intelligence, IEEE Transactions on*, 26(9):1124–1137, 2004.

[54] Yuri Boykov and Gareth Funka-Lea. Graph cuts and efficient nd image segmentation. *International Journal of Computer Vision*, 70(2):109–131, 2006.

[55] Kang Li, Xiaodong Wu, Danny Z Chen, and Milan Sonka. Optimal surface segmentation in volumetric images-a graph-theoretic approach. *Pattern Analysis and Machine Intelligence, IEEE Transactions on*, 28(1):119–134, 2006.

[56] Yin Yin, Xiangmin Zhang, Rachel Williams, Xiaodong Wu, Donald D Anderson, and Milan Sonka. LOGISMOS-layered optimal graph image segmentation of multiple objects and surfaces: cartilage segmentation in the knee joint. *Medical Imaging, IEEE Transactions on*, 29(12):2023–2037, 2010.

[57] Qi Song, Xiaodong Wu, Yunlong Liu, Mark Smith, John Buatti, and Milan Sonka. Optimal graph search segmentation using arc-weighted graph for simultaneous surface detection of bladder and prostate. In *Medical Image Computing and Computer-Assisted Intervention–MICCAI 2009*, pages 827–835. Springer, 2009.

[58] Li Zhang, Gabriëlle HS Buitendijk, Kyungmoo Lee, Milan Sonka, Henriët Springelkamp, Albert Hofman, Johannes R Vingerling, Robert F Mullins, Caroline CW Klaver, and Michael D Abràmoff. Validity of automated choroidal

segmentation in SS-OCT and SD-OCT. *Investigative Ophthalmology & Visual Science*, 56(5):3202–3211, 2015.

[59] MJ Hogan and JE JA Weddell. Histology of the human eye: an atlas and textbook. 1971.

[60] Marco A Zarbin. Current concepts in the pathogenesis of age-related macular degeneration. *Archives of ophthalmology*, 122(4):598–614, 2004.

[61] D Scott McLeod, Rhonda Grebe, Imran Bhutto, Carol Merges, Takayuki Baba, and Gerard A Lutty. Relationship between rpe and choriocapillaris in age-related macular degeneration. *Investigative ophthalmology & visual science*, 50(10):4982–4991, 2009.

[62] Robert F Mullins, Micaela N Johnson, Elizabeth A Faidley, Jessica M Skeie, and Jian Huang. Choriocapillaris vascular dropout related to density of drusen in human eyes with early age-related macular degeneration. *Investigative ophthalmology & visual science*, 52(3):1606–1612, 2011.

[63] Raan S Ramrattan, Theo L van der Schaft, Cornelia M Mooy, WC De Bruijn, PG Mulder, and PT De Jong. Morphometric analysis of bruch's membrane, the choriocapillaris, and the choroid in aging. *Investigative ophthalmology & visual science*, 35(6):2857–2864, 1994.

[64] Pichai Jirarattanasopa, Sotaro Ooto, Isao Nakata, Akitaka Tsujikawa, Kenji Yamashiro, Akio Oishi, and Nagahisa Yoshimura. Choroidal thickness, vascular hyperpermeability, and complement factor h in age-related macular degeneration and polypoidal choroidal vasculopathy. *Investigative ophthalmology & visual science*, 53(7):3663–3672, 2012.

[65] Lawrence A Yannuzzi. Indocyanine green angiography: a perspective on use in the clinical setting. *American journal of ophthalmology*, 151(5):745–751, 2011.

[66] Paulo E Stanga, Jennifer I Lim, and Peter Hamilton. Indocyanine green angiography in chorioretinal diseases: indications and interpretation: an evidence-based update. *Ophthalmology*, 110(1):15–21, 2003.

[67] SM Reza Motaghiannezam, David Koos, and Scott E Fraser. Differential phase-contrast, swept-source optical coherence tomography at 1060 nm for in vivo human retinal and choroidal vasculature visualization. *Journal of biomedical optics*, 17(2):0260111–0260115, 2012.

[68] Varsha Manjunath, Mohammad Taha, James G Fujimoto, and Jay S Duker.

Choroidal thickness in normal eyes measured using cirrus hd optical coherence tomography. *American journal of ophthalmology*, 150(3):325–329, 2010.

[69] Mona Kathryn Garvin, Michael D Abràmoff, Randy Kardon, Stephen R Russell, Xiaodong Wu, and Milan Sonka. Intraretinal layer segmentation of macular optical coherence tomography images using optimal 3-d graph search. *Medical Imaging, IEEE Transactions on*, 27(10):1495–1505, 2008.

[70] Meindert Niemeijer, Mona K Garvin, Bram van Ginneken, Milan Sonka, and Michael D Abramoff. Vessel segmentation in 3D spectral OCT scans of the retina. In *Medical Imaging*, pages 69141R–69141R. International Society for Optics and Photonics, 2008.

[71] Yoshinobu Sato, C-F Westin, Abhir Bhalerao, Shin Nakajima, Nobuyuki Shiraga, Shinichi Tamura, and Ron Kikinis. Tissue classification based on 3D local intensity structures for volume rendering. *Visualization and Computer Graphics, IEEE Transactions on*, 6(2):160–180, 2000.

[72] Yoshinobu Sato, Shin Nakajima, Nobuyuki Shiraga, Hideki Atsumi, Shigeyuki Yoshida, Thomas Koller, Guido Gerig, and Ron Kikinis. Three-dimensional multi-scale line filter for segmentation and visualization of curvilinear structures in medical images. *Medical image analysis*, 2(2):143–168, 1998.

[73] Alejandro F Frangi, Wiro J Niessen, Koen L Vincken, and Max A Viergever. Multiscale vessel enhancement filtering. In *Medical Image Computing and Computer-Assisted Interventation-MICCAI-98*, pages 130–137. Springer, 1998.

[74] Fred L. Bookstein. Principal warps: Thin-plate splines and the decomposition of deformations. *IEEE Transactions on pattern analysis and machine intelligence*, 11(6):567–585, 1989.

[75] Lee R Dice. Measures of the amount of ecologic association between species. *Ecology*, 26(3):297–302, 1945.

[76] U Schneider, H Kuck, W Inhoffen, and I Kreissig. Indocyanine green angiographically well-defined choroidal neovascularization: angiographic patterns obtained using the scanning laser ophthalmoscope. *German journal of ophthalmology*, 4(2):67–74, 1995.

[77] Shin Yoneya, Mark OM Tso, and K Shimizu. Patterns of the choriocapillaris. *International ophthalmology*, 6(2):95–99, 1983.

[78] Yoko Nishiyama Ito, Keisuke Mori, Josephine Young-Duvall, and Shin Yoneya.

Aging changes of the choroidal dye filling pattern in indocyanine green angiography of normal subjects. *Retina*, 21(3):237–242, 2001.

[79] Michael D Abràmoff, Kyungmoo Lee, Meindert Niemeijer, Wallace LM Alward, Emily C Greenlee, Mona K Garvin, Milan Sonka, and Young H Kwon. Automated segmentation of the cup and rim from spectral domain OCT of the optic nerve head. *Investigative ophthalmology & visual science*, 50(12):5778–5784, 2009.

[80] Marieh Esmaeelpour, Boris Považay, Boris Hermann, Bernd Hofer, Vedran Kajic, Ketan Kapoor, Nik JL Sheen, Rachel V North, and Wolfgang Drexler. Three-dimensional 1060-nm OCT: choroidal thickness maps in normal subjects and improved posterior segment visualization in cataract patients. *Investigative ophthalmology & visual science*, 51(10):5260–5266, 2010.

[81] Tetsuya Agawa, Masahiro Miura, Yasuhi Ikuno, Shuichi Makita, Tapio Fabritius, Takuya Iwasaki, Hiroshi Goto, Kohji Nishida, and Yoshiaki Yasuno. Choroidal thickness measurement in healthy japanese subjects by three-dimensional high-penetration optical coherence tomography. *Graefe's Archive for Clinical and Experimental Ophthalmology*, 249(10):1485–1492, 2011.

[82] Yasushi Ikuno, Kana Kawaguchi, Takeyoshi Nouchi, and Yoshiaki Yasuno. Choroidal thickness in healthy japanese subjects. *Investigative ophthalmology & visual science*, 51(4):2173–2176, 2010.

[83] Richard F Spaide, Hideki Koizumi, and Maria C Pozonni. Enhanced depth imaging spectral-domain optical coherence tomography. *American journal of ophthalmology*, 146(4):496–500, 2008.

[84] Scott A Read, Michael J Collins, Stephen J Vincent, and David Alonso-Caneiro. Choroidal thickness in childhood. *Investigative ophthalmology & visual science*, 54(5):3586–3593, 2013.

[85] Vedran Kajić, Marieh Esmaeelpour, Boris Považay, David Marshall, Paul L Rosin, and Wolfgang Drexler. Automated choroidal segmentation of 1060 nm OCT in healthy and pathologic eyes using a statistical model. *Biomedical optics express*, 3(1):86–103, 2012.

[86] Yukiko Matsuo, Taiji Sakamoto, Takehiro Yamashita, Masatoshi Tomita, Makoto Shirasawa, and Hiroto Terasaki. Comparisons of choroidal thickness of normal eyes obtained by two different spectral-domain OCT instruments and one swept-source OCT instrument. *Investigative ophthalmology & visual science*, 54(12):7630–7636, 2013.

[87] David Alonso-Caneiro, Scott A Read, and Michael J Collins. Automatic segmentation of choroidal thickness in optical coherence tomography. *Biomedical optics express*, 4(12):2795–2812, 2013.

[88] Albert Hofman, Sarwa Darwish Murad, Cornelia M van Duijn, Oscar H Franco, André Goedegebure, M Arfan Ikram, Caroline CW Klaver, Tamar EC Nijsten, Robin P Peeters, Bruno H Ch Stricker, et al. The Rotterdam study: 2014 objectives and design update. *European journal of epidemiology*, 28(11):889–926, 2013.

[89] Andreas Wahle, Kyungmoo Lee, Adam T Harding, Mona K Garvin, Meindert Niemeijer, Milan Sonka, and Michael D Abràmoff. Extending the XNAT archive tool for image and analysis management in ophthalmology research. In *SPIE Medical Imaging*, pages 86740M–86740M. International Society for Optics and Photonics, 2013.

[90] Kyungmoo Lee, Milan Sonka, Young H Kwon, Mona K Garvin, and Michael D Abràmoff. Adjustment of the retinal angle in SD-OCT of glaucomatous eyes provides better intervisit reproducibility of peripapillary RNFL thickness. *Investigative ophthalmology & visual science*, 54(7):4808–4812, 2013.

[91] Paul Riordan-Eva and John Whitcher. *Vaughan & Asbury's general ophthalmology*. Wiley Online Library, 2008.

[92] Dietmar Stöckl, Diego Rodríguez Cabaleiro, Katleen Van Uytfanghe, and Linda M Thienpont. Interpreting method comparison studies by use of the bland–altman plot: reflecting the importance of sample size by incorporating confidence limits and predefined error limits in the graphic. *Clinical chemistry*, 50(11):2216–2218, 2004.

[93] Christopher M Bishop et al. *Pattern recognition and machine learning*, volume 4. springer New York, 2006.

[94] Emily A McCourt, Brian C Cadena, Cullen J Barnett, Antonio P Ciardella, Naresh Mandava, and Malik Y Kahook. Measurement of subfoveal choroidal thickness using spectral domain optical coherence tomography. *Ophthalmic Surg Lasers Imaging*, 41(Suppl):S28–S33, 2010.

[95] K Lee, MK Garvin, S Russell, M Sonka, and MD Abràmoff. Automated intraretinal layer segmentation of 3-d macular OCT scans using a multiscale graph search. *Invest Ophthalmol Vis Sci*, 2010.

[96] Frederick L Ferris, Stuart L Fine, and Leslie Hyman. Age-related macular

degeneration and blindness due to neovascular maculopathy. *Archives of ophthalmology*, 102(11):1640–1642, 1984.

[97] Neil M Bressler, Susan B Bressler, and Stuart L Fine. Age-related macular degeneration. *Survey of ophthalmology*, 32(6):375–413, 1988.

[98] Daniel F Martin, Maureen G Maguire, Stuart L Fine, Gui-shuang Ying, Glenn J Jaffe, Juan E Grunwald, Cynthia Toth, Maryann Redford, Frederick L Ferris, Comparison of Age-related Macular Degeneration Treatments Trials (CATT) Research Group, et al. Ranibizumab and bevacizumab for treatment of neovascular age-related macular degeneration: two-year results. *Ophthalmology*, 119(7):1388–1398, 2012.

[99] Christian Ahlers, Isabelle Golbaz, Elisa Einwallner, Roman Dunavölgyi, Panagiotis Malamos, Geraldine Stock, Christian Pruente, and Ursula Schmidt-Erfurth. Identification of optical density ratios in subretinal fluid as a clinically relevant biomarker in exudative macular disease. *Investigative ophthalmology & visual science*, 50(7):3417–3424, 2009.

[100] Eva Smretschnig, Ilse Krebs, Sarah Moussa, Siamak Ansari-Shahrezarei, and Susanne Binder. Cirrus OCT versus spectralis OCT: differences in segmentation in fibrovascular pigment epithelial detachment. *Graefe's archive for clinical and experimental ophthalmology*, 248(12):1693–1698, 2010.

[101] Kyungmoo Lee, Meindert Niemeijer, Mona K Garvin, Young H Kwon, Milan Sonka, and Michael D Abramoff. Segmentation of the optic disc in 3D OCT scans of the optic nerve head. *Medical Imaging, IEEE Transactions on*, 29(1):159–168, 2010.

[102] Richard F Spaide and Christine A Curcio. Anatomical correlates to the bands seen in the outer retina by optical coherence tomography: literature review and model. *Retina (Philadelphia, Pa.)*, 31(8):1609, 2011.

[103] Michael D Abràmoff, Robert F Mullins, Kyungmoo Lee, Jeremy M Hoffmann, Milan Sonka, Douglas B Critser, Steven F Stasheff, and Edwin M Stone. Human photoreceptor outer segments shorten during light adaptation. *Investigative ophthalmology & visual science*, 54(5):3721–3728, 2013.

[104] David Huang, Eric A Swanson, Charles P Lin, Joel S Schuman, William G Stinson, Warren Chang, Michael R Hee, Thomas Flotte, Kenton Gregory, Carmen A Puliafito, et al. Optical coherence tomography. *Science*, 254(5035):1178–1181, 1991.

[105] Daniel F Kiernan, William F Mieler, and Seenu M Hariprasad. Spectral-domain

optical coherence tomography: a comparison of modern high-resolution retinal imaging systems. *American journal of ophthalmology*, 149(1):18–31, 2010.

[106] Jennifer H Acton, R Theodore Smith, Donald C Hood, and Vivienne C Greenstein. Relationship between retinal layer thickness and the visual field in early age-related macular degeneration. *Investigative ophthalmology & visual science*, 53(12):7618–7624, 2012.

[107] Ahmed Abdelsalam, Lucian Del Priore, and Marco A Zarbin. Drusen in age-related macular degeneration: pathogenesis, natural course, and laser photocoagulation–induced regression. *Survey of ophthalmology*, 44(1):1–29, 1999.

[108] Ronald Klein, Barbara EK Klein, Susan C Jensen, and Stacy M Meuer. The five-year incidence and progression of age-related maculopathy: the beaver dam eye study. *Ophthalmology*, 104(1):7–21, 1997.

[109] Age-Related Eye Disease Study Research Group et al. A simplified severity scale for age-related macular degeneration: Areds report no. 18. *Archives of ophthalmology*, 123(11):1570, 2005.

[110] Konstantinos Rapantzikos and Michalis Zervakis. Nonlinear enhancement and segmentation algorithm for the detection of age-related macular degeneration (amd) in human eye's retina. In *Image Processing, 2001. Proceedings. 2001 International Conference on*, volume 3, pages 1055–1058. IEEE, 2001.

[111] Konstantinos Rapantzikos, M Zervakis, and K Balas. Detection and segmentation of drusen deposits on human retina: Potential in the diagnosis of age-related macular degeneration. *Medical image analysis*, 7(1):95–108, 2003.

[112] Paolo Checco and Fernando Corinto. Cnn-based algorithm for drusen identification. In *Circuits and Systems, 2006. ISCAS 2006. Proceedings. 2006 IEEE International Symposium on*, pages 4–pp. IEEE, 2006.

[113] David E Freund, Neil Bressler, and Philippe Burlina. Automated detection of drusen in the macula. In *Biomedical Imaging: From Nano to Macro, 2009. ISBI'09. IEEE International Symposium on*, pages 61–64. IEEE, 2009.

[114] Ziyang Liang, Damon WK Wong, Jiang Liu, Kap Luk Chan, and Tien Yin Wong. Towards automatic detection of age-related macular degeneration in retinal fundus images. In *Conf Proc IEEE Eng Med Biol Soc*, pages 4100–4103, 2010.

[115] Wolfgang Drexler, Harald Sattmann, Boris Hermann, Tony H Ko, Michael Stur,

Angelika Unterhuber, Christoph Scholda, Oliver Findl, Matthias Wirtitsch, James G Fujimoto, et al. Enhanced visualization of macular pathology with the use of ultrahigh-resolution optical coherence tomography. *Archives of ophthalmology*, 121(5):695–706, 2003.

[116] Maciej Wojtkowski, Vivek Srinivasan, James G Fujimoto, Tony Ko, Joel S Schuman, Andrzej Kowalczyk, and Jay S Duker. Three-dimensional retinal imaging with high-speed ultrahigh-resolution optical coherence tomography. *Ophthalmology*, 112(10):1734–1746, 2005.

[117] Vivek J Srinivasan, Maciej Wojtkowski, Andre J Witkin, Jay S Duker, Tony H Ko, Mariana Carvalho, Joel S Schuman, Andrzej Kowalczyk, and James G Fujimoto. High-definition and 3-dimensional imaging of macular pathologies with high-speed ultrahigh-resolution optical coherence tomography. *Ophthalmology*, 113(11):2054–2065, 2006.

[118] Samuel R Freeman, Igor Kozak, Lingyun Cheng, Dirk-Uwe Bartsch, Francesca Mojana, Nitin Nigam, Manpreet Brar, Ritchie Yuson, and William R Freeman. Optical coherence tomography-raster scanning and manual segmentation in determining drusen volume in age-related macular degeneration. *Retina*, 30(3):431–435, 2010.

[119] Sina Farsiu, Stephanie J Chiu, Joseph A Izatt, and Cynthia A Toth. Fast detection and segmentation of drusen in retinal optical coherence tomography images. In *Biomedical Optics (BiOS) 2008*, pages 68440D–68440D. International Society for Optics and Photonics, 2008.

[120] Kayoung Yi, Mircea Mujat, Boris H Park, Wei Sun, Joan W Miller, Johanna M Seddon, Lucy H Young, Johannes F de Boer, and Teresa C Chen. Spectral domain optical coherence tomography for quantitative evaluation of drusen and associated structural changes in non-neovascular age-related macular degeneration. *British Journal of Ophthalmology*, 93(2):176–181, 2009.

[121] Giovanni Gregori, Fenghua Wang, Philip J Rosenfeld, Zohar Yehoshua, Ninel Z Gregori, Brandon J Lujan, Carmen A Puliafito, and William J Feuer. Spectral domain optical coherence tomography imaging of drusen in nonexudative age-related macular degeneration. *Ophthalmology*, 118(7):1373–1379, 2011.

[122] Daisuke Iwama, Masanori Hangai, Sotaro Ooto, Atsushi Sakamoto, Hideo Nakanishi, Takashi Fujimura, Amitha Domalpally, Ronald P Danis, and Nagahisa Yoshimura. Automated assessment of drusen using three-dimensional spectral-domain optical coherence tomography. *Investigative ophthalmology & visual science*, 53(3):1576–1583, 2012.

[123] Qiang Chen, Theodore Leng, Luoluo Zheng, Lauren Kutzscher, Jeffrey Ma, Luis de Sisternes, and Daniel L Rubin. Automated drusen segmentation and quantification in SD-OCT images. *Medical image analysis*, 17(8):1058–1072, 2013.

[124] Robert F Mullins, Elizabeth A Faidley, Heather T Daggett, Catherine Jomary, Andrew J Lotery, and Edwin M Stone. Localization of complement 1 inhibitor (c1inh/serping1) in human eyes with age-related macular degeneration. *Experimental eye research*, 89(5):767–773, 2009.